Optically detected magnetic resonance studies of magnesium doped gallium nitride

Zeng, Shanshan

Award date:
2005

Awarding institution:
University of Bath

OPTICALLY DETECTED MAGNETIC RESONANCE STUDIES OF MAGNESIUM DOPED GALLIUM NITRIDE

ProQuest LLC
789 East Eisenhower Parkway
P.O. Box 1346
Ann Arbor, MI 48106-1346

Acknowledgment

First of all, I would like to thank my supervisors, Dr. Daniel Wolverson and Prof. J. John Davies for accepting me as a Ph. D. student. I have benefited a lot from their thorough and patient guidance. I also appreciated very much that I was given the opportunity to participate in various conferences. On the non-scientific side I would like to thank them for organizing various activities, which gave me a unique experience of British culture and life.

In addition to the discussions with my supervisors, I had the pleasure to get enormous instructions from Dr. Gazi Aliev and Dr. Stephen Bingham, who have never been far away in trouble times.

I would also like to acknowledge the close collaboration and very useful discussions with groups of Prof. Paul G Coleman and Prof. Wang N Wang in Bath. I am very grateful to Mr. Harry Bone for excellent technical assistance.

I would like to thank Lowwana Smith for the pleasant atmosphere we have always had in our office and for many entertaining discussions on scientific and non-scientific topics.

I am deeply indebted to my parents, who have given me persistent support morally and financially through these years.

I cordially thank Xiaodong, who shares my dreams and boosts me in hardness. It is very lucky to have your accompany in my journey of life.

Finally, I would like to thank Universities UK and University of Bath for providing me a studentship.

Abstract

In this thesis, Optically Detected Magnetic Resonance (ODMR) technique, together with Photoluminescence (PL) and Positron Annihilation Spectroscopy (PAS) methods, have been applied to the study of magnesium doped epitaxial gallium nitride layers. The origins of two defect related PL bands in Metal-Organic Vapor-Phase Epitaxy (MOVPE) grown specimens, namely the "red" band and the "green" band, have been extensively discussed. It is suggested that the red emission is due to recombination between electrons from both effective-mass and deeper donors with holes from deep acceptors and point to the deeper donors being $V_N - Mg_{Ga}$ and the deep acceptors V_{Ga} (or related complexes). The ODMR spectra on the green spectral region are dominated by several broad anisotropic lines. The spectra are described by an exchange-coupled pair of $S = 1/2$ centres, which is tentatively assigned to a shallow donor-Mg complex. Systematically studies of the evolvements of defect centres with increasing magnesium concentration and with thermal annealing enables a better understanding of the defect formations and compensation mechanism in the materials. To study the spin dynamics in the specimens, two simple rate equation models are employed. Both models are able to represent the experimental waveforms of the change of PL intensity with the microwave power switched on and off. Finally, the defects involved in the recombination processes in Molecular Beam Epitaxy (MBE) grown layers are also discussed and compared to those in MOVPE grown ones.

Contents

Chapter 1

General properties of GaN

1.1 Introduction

During the last 15 years the developments in the field of III-nitride semiconductors (GaN, AlN, InN and their ternary and quaternary alloys) have been spectacular. The main application of the material system is its contribution to ultra violet (UV) and blue light emitters as well as solid state lighting. At room temperature the band gap values are $\sim$ 0.64 to 0.67 eV for InN, 3.4 eV for GaN, and 6.2 eV for AlN. They form a complete series of alloys whose direct band gaps, in principle, can cover the whole visible region and extend to the ultraviolet range. Indium-based III-nitride single quantum well (SQW) and multiple quantum well (MQW) structures have been employed as active layers of high-brightness blue and green light-emitting diodes (LEDs) and laser diodes (LDs). More than 10,000 h of working life of blue/green lasers has been demonstrated [1]. AlGaN-based UV emitters have found applications in biotechnology, environmental and medical use as well as free-space communication. The material system has also applications as short wavelength detectors and high-power/temperature radio frequency electronic devices. However, further improvements in device performance hinge on understanding and reduction of extended and point defects. To achieve this a wide range of experimental methods has been employed and among them, Photoluminescence (PL) and Optically Detected Magnetic Resonance (ODMR)

are powerful methods to investigate point defect-related radiative recombination processes in semiconductors.

In this chapter we start with the description of crystal structure and electronic band structure of III-nitrides, which relates directly to ODMR studies of this material system. An accurate knowledge of the band structure of the semiconductor in question is crucial in determining its potential utility. It is the direct-band-gap nature and the size of the band gap that stimulated the great interest in this material system. In Sec. 1.4 two major growth methods, Metal-Organic Vapor-Phase Epitaxy (MOVPE) and Molecular Beam Epitaxy (MBE), are briefly discussed. The large lattice mismatch and the large difference in thermal expansion coefficients between GaN films and substrate materials lead to great difficulty in the growth of high quality materials. The review of substrates is also presented in Sec. 1.4. The properties of semiconductors are often controlled by defects and impurities. In this chapter the intrinsic defects in GaN and *n*-type and *p*-type doping are also reviewed.

1.2 Crystal structure

The III-nitrides can normally exist in Wurtzite (WZ) and Zincblende (ZB) crystal polytypes, with the WZ phase being the stable and widely used form. Crystallographically, the WZ structure and the ZB structure are very closely related. For both structures, the bonding to the next neighbors is tetrahedral. The WZ structure has a hexagonal primitive cell and thus two lattice constants, a and c. It consists of two interpenetrating hexagonal close packed (hcp) sublattices, one with group III atoms and the other with group V atoms, offset along the c axis by 5/8 of the cell height. Its space group is C_{6v}^4. The ZB structure, on the other hand, has a cubic primitive cell and a single lattice constant a. It can be viewed as two face-centred cubic (fcc) structures, each with one type of atoms, displaced from each other by one-quarter of a body diagonal. The layer stacking in the $\langle 0001 \rangle$ direction in WZ structure is equivalent to that along the $\langle 111 \rangle$ direction in ZB structure. For WZ structure, the stacking sequence of the (0001) plane in

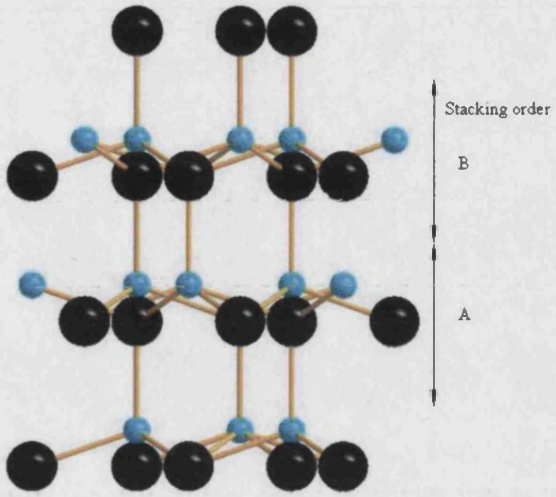

Figure 1.1: A stick and ball diagram of a hexagonal structure.

the $\langle 0001 \rangle$ direction is:

$$...Ga_AN_AGa_BN_BGa_AN_AGa_BN_BGa_AN_AGa_BN_B \tag{1.1}$$

whereas for the ZB lattice the stacking sequence of the (111) plane in the $\langle 111 \rangle$ direction is:

$$...Ga_AN_AGa_BN_BGa_CN_CGa_AN_AGa_BN_BGa_CN_C. \tag{1.2}$$

In this thesis all the GaN samples under study are of WZ symmetry. A stick and ball representation of a WZ structure is depicted in Fig. 1.1. Table 1.1 shows the calculated [2] and experimental [3] values of the lattice parameters for WZ GaN.

Table 1.1: Lattice constants for GaN

	Experimental values	Calculated values
a	3.189 Å	3.174 Å
c	5.178 Å	5.169 Å

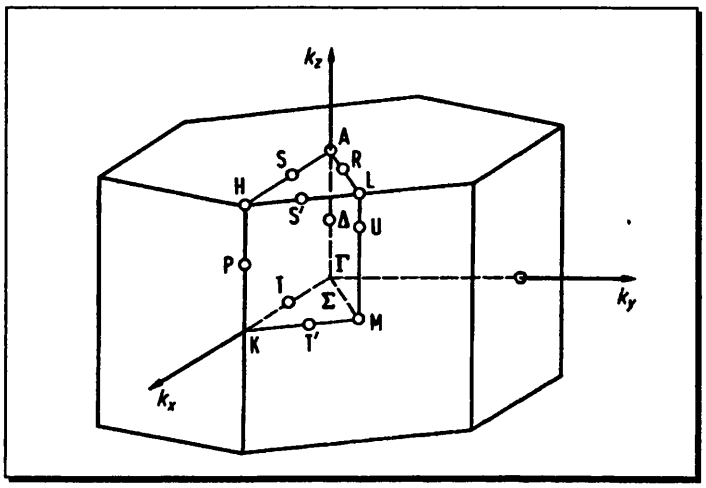

Figure 1.2: Structure and the first Brillouin zone of a Wurtzite crystal.

1.3 Electronic band structure

The main difference between the band structures of WZ and ZB crystals is the influence of the crystal field on the valence band. The crystal field splitting is present only in the WZ structure and transforms the semiconductor from ZB to WZ. In this sense, the WZ structure acts like a "pre-strained" cubic crystal. With the presence of crystal field in the WZ structure, the effects of quantum well confinement and strain on the GaN valence band structure are much less dramatic than in, for example, GaAs.

The first Brillouin zone of a WZ crystal is displayed in Fig. 1.2. The conduction band wave functions are formed from the s orbital of Ga atoms combined with spin functions and transform the Γ point as the Γ_7 representation of the space group C_{6v}^4. The valence band states are constructed of combinations of p_3-like

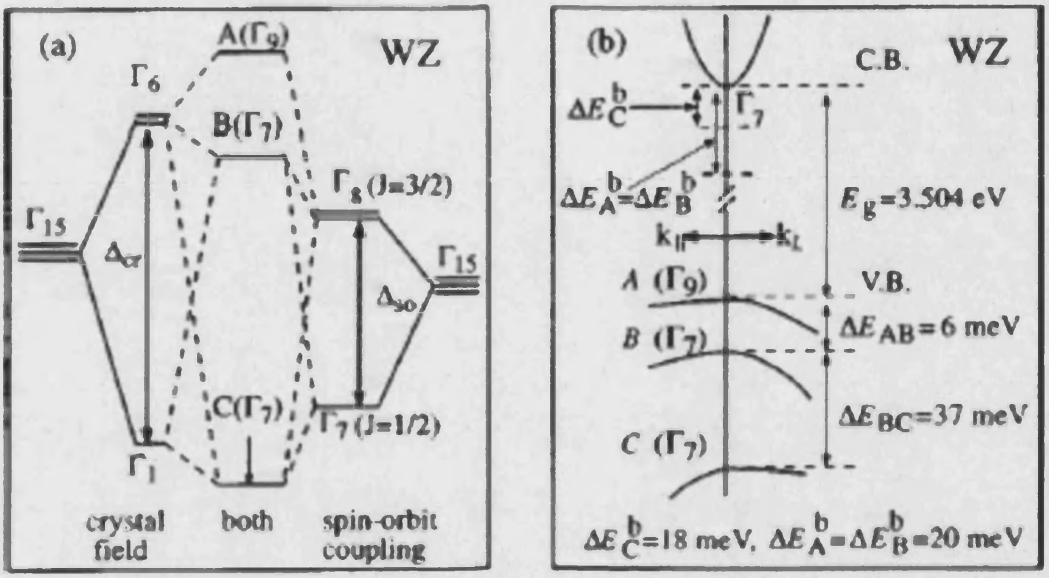

Figure 1.3: (a) Effect of crystal field splitting and spin-orbit coupling on the valence band (near the Γ point) of WZ GaN [4]. At k = 0, the valence band is split by the combined action of crystal field and spin-orbit coupling into A(Γ_9), B(Γ_7) and C(Γ_7) states. (b) Calculated values of the band energy levels [5] near the Γ point. ΔE_A^b, ΔE_B^b, ΔE_C^b are the binding energies of the A, B, C excitons, respectively.

(p_x, p_y, p_z- like) orbitals on N atoms with spin functions. A schematic diagram of the valence band splitting is shown in Fig. 1.3a [4] and the calculated values of the band energy levels are shown in Fig. 1.3b [5]. Under the influence of the crystal field and spin-orbit interaction, the six-fold degenerate Γ_{15} level splits into Γ_9 (A), upper Γ_7 (B), and lower Γ_7 (C) levels. The levels are named as HH (heavy hole), LH (light hole) and CH (crystal-field split hole), respectively. In Fig. 1.3a, from left to right, the crystal-field splitting is considered first. From right to left, the spin-orbit splitting is considered first. Regardless of which is considered first, the final result is the same in that there are three valence bands which are sufficiently close to one another so that the band mixing is non-negligible. Free excitons may involve a hole from each of the subbands and are conventionally called A-, B-, C-type holes or excitons.

The band structure diagram shown in Fig. 1.3b is obtained by the first princi-

ple band structure calculations, using the Local Density Approximation (LDA) as implemented by the all-electron relativistic, Full-potential Linearized Augmented Plane Wave (FLAPW) method [5]. The FLAPW method is presently one of the most accurate electronic structure calculation schemes. The exchange-correlation (xc) functional can be treated using the LDA, which is the most simple approximation for the xc-energy functional, the crucial quantity of density functional theory. For given local density $n(r)$, the LDA replaces the true xc-energy density at each point r in space by the xc-energy density of a homogeneous electron gas of the same (global) density $n_0 = n(r)$. The calculated conduction band and valence band structures near the Γ point are strongly non-parabolic (Fig. 1.3b), and therefore the effective mass approximation and the $\mathbf{k}\cdot\mathbf{p}$ approximation are usually inadequate.

1.4 Growth of GaN

1.4.1 Substrate

Because of the low solubility of nitrogen in gallium and the high vapor pressure of nitrogen on GaN, bulk growth of GaN must resort to very high temperatures and pressures. GaN crystals are therefore normally grown epitaxially. Due to lacking a commercial lattice matched substrate, good GaN epilayers could not be obtained until the late 1980s. Sapphire is currently the most extensively used substrate. The lattice mismatch of GaN with sapphire is $\sim 13\%$. The technology of growth of the nitrides on sapphire is quite mature. Most commonly, GaN is grown on the (0001) plane (c plane). With the increasing interest in nonpolar III-nitrides heterostructures, more recently, growth of $(11\bar{2}0)$ quantum wells (QWs) on r-plane sapphire substrates was attempted by MBE [6] as well as by MOVPE [7]. In these QWs the spontaneous and piezoelectric polarization is avoided and therefore the internal electrical field that spatially separates the electron and hole wave functions in conventionally grown QWs is absent, thus the internal quantum efficiency is increased. Due to the large mismatch in the lattice constants and coefficients of thermal expansion of GaN and sapphire, the quality of the film

grown directly on sapphire is poor. Good quality films can be grown by first growing a low temperature buffer layer.

GaN growth onto a variety of other substrate materials has also been investigated by researchers. GaN has been grown on 6H SiC, ZnO, $MgAl_2O_4$, Si, etc. The properties of several substrate materials have been discussed in Refs. [8] and [9]. The lattice mismatches between GaN and SiC (3.5%), ZnO(1.9%) and $MgAl_2O_4$(9.5%) are smaller than for growth onto sapphire. WZ GaN has also been successfully obtained on (111) Si. However, sapphire is generally still the preferred substrate because of its low cost, hexagonal symmetry, ease of handling and high stability at high temperature. All of the samples studied in this thesis were grown on sapphire.

To further improve film quality, homoepitaxial growth of GaN films has become increasingly popular. The approach consists of growing a thick (normally 300 - 1000 μm) GaN layer to be separated from the original hetero-substrate and used as a free-standing substrate for subsequent growth of epilayers and quantum structures. The thick GaN layer is normally grown by Hydride Vapor-Phase Epitaxy (HVPE) since it provide a reasonably high growth-rate. The dislocation density and impurity concentrations in homoepitaxial films are normally much reduced compared to those in conventional heteroepitaxial layers.

1.4.2 Metal-Organic Vapor-Phase Epitaxy (MOVPE)

All the high performance nitride light emitters, which require high quality InGaN, have been produced by MOVPE. In MOVPE, trimethylgallium (TMGa) for Ga, trimethylaluminum (TMAl) for Al, and trimethylindium (TMIn) for In react with NH_3 (for nitrogen) at a substrate which is heated to roughly 1000°C. Mg is widely used as a *p*-type dopant and Si as an *n*-type dopant. Biscyclopentadienyl (Cp_2Mg) is use as a source of Mg and methyl silane ($MeSiH_3$) as a source of Si. A two-flow method, introduced by Nakamura (Fig. 1.4) [10], improves significantly the quality of GaN epilayers. In this method, in addition to the main gas flow parallel to the substrate, another flow, designed as the "subflow" is used. The subflow transports a mixture of the inactive gases H_2 and N_2 perpendicular to

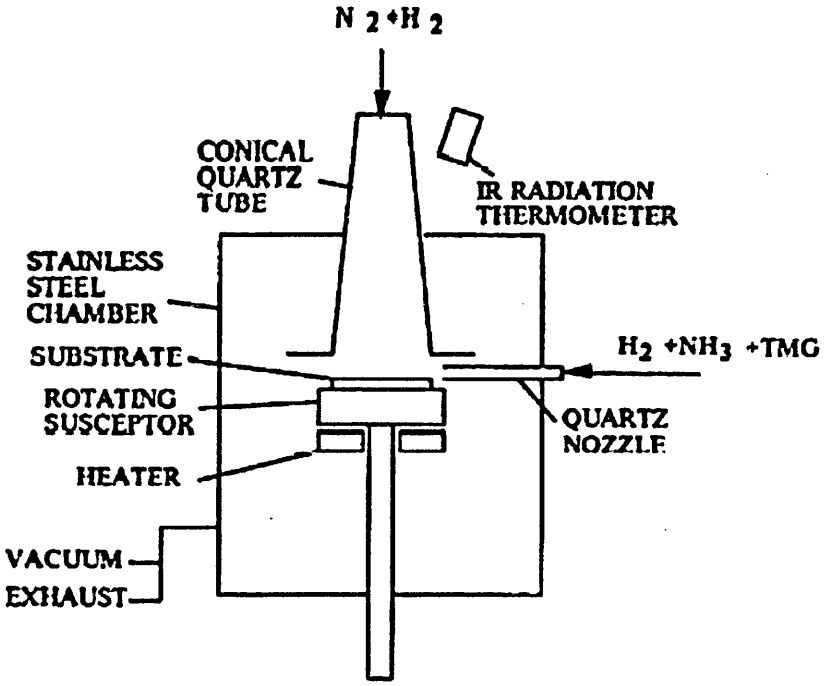

Figure 1.4: Schematic two-flow MOVPE reactor for GaN growth [10].

the substrate. The subflow changes the direction of the main flow to bring the reactant gas in contact with the substrate. Without the subflow, a continuous film could not be obtained and only the growth of a few islands on the substrate was obtained [10].

1.4.3 Molecular Beam Epitaxy (MBE)

MBE technique provides precise control over the growth parameters and powerful *in-situ* monitoring capabilities. This allows the preparation of many different structures that are otherwise not possible to attain.

Initially an MBE system is essentially a metal evaporator working in an ultrahigh vacuum (UHV) environment. Gas sources were utilized in some cases, which is termed Gas-source MBE (GSMBE). In nitride growth by MBE, the metal species are provided by Ga, In and Al metal sources and the dopant are provided by pure Si for n-type and Mg for p-type. N is provided by N_2, usually in a

plasma environment to enhance the dissociation of the nitrogen molecules, or NH_3. MBE growth has been reported by electron cyclotron resonance microwave-plasma-assisted MBE (ECR-MBE) [11] and radio frequency-plasma assisted MBE (RF-MBE).

MBE grown structures based on conventional compound semiconductors have been produced successfully for applications such as IR lasers for CD players, surface emitting vertical cavity lasers and high-performance pseudomorphic MODFETs. Nitride growth, however, requires much higher temperatures than those used in producing conventional group III-V semiconductors for which MBE systems were initially designed. The materials grown on foreign substrates such as sapphire and SiC are normally associated with high dislocation densities, typically in the range of 5×10^9 - 5×10^{10}cm^{-2} [12]. As a result the room temperature electron mobility values (in the range of 100-300 cm^2/Vs [12]) are much lower than those of materials grown by MOVPE (normally in excess of 900 cm^2/Vs [13]). The dislocation reduction, which is the key to achieving high mobility GaN, can be realized by using HVPE or MOVPE buffer layer. This approach has led to record or near record bulk (1150 cm^2/Vs RT) [14] and 2DEG (53,550 cm^2/Vs 4.2K) [15] mobilities.

1.5 Defects and doping

1.5.1 Formation of native point defects in GaN

Native defects are point defects intrinsic to the semiconductor, such as vacancies (missing atoms), self-interstitials (additional atoms incorporated on sites other than substitutional sites), and antisites (in a compound semiconductor, a cation sitting on a nominal anion site, or vice versa). First-principles calculations for native point defects in GaN have been reported by several groups [17, 18, 19]. Formation energies for all of them in GaN, in all relevant charge states, are shown in Fig. 1.5. It shows that self-interstitial (Ga_i and N_i) and antisite (Ga_N and N_{Ga}) defects are high-energy defects in GaN, and are thus unlikely to occur

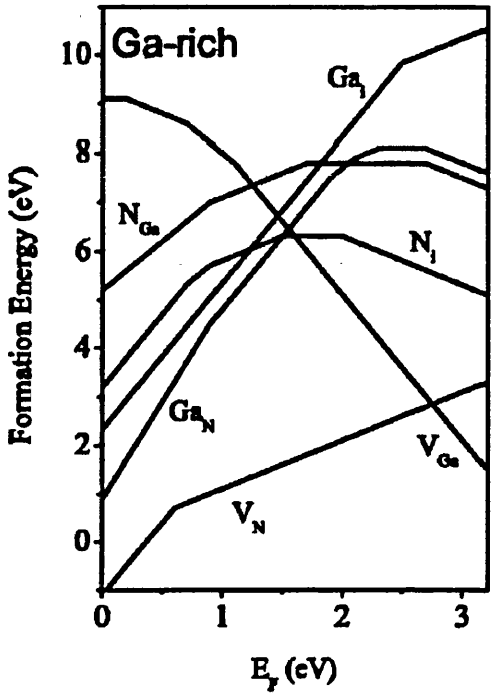

Figure 1.5: Formation energies as a function of Fermi level for native point defects in GaN. Ga-rich conditions are assumed. The zero of Fermi level corresponds to the top of the valence band. Only segments corresponding to the lowest-energy charge states are shown. The slope of these segments indicates the charge state. Kinks in the curves indicate transitions between different charge states [16].

in thermal equilibrium. Only vacancies have low enough energies to be present in significant concentrations. Nitrogen vacancies (V_N) behave as shallow donors in GaN, for almost 25 years, this has been thought to be the source of the *n*-type "autodoping" of GaN [20, 21]. However, based on first-principles calculations, their high formation energy under *n*-type conditions makes it very unlikely that V_N would form spontaneously during growth of not-intentionally doped GaN, and hence they cannot be responsible for *n*-type conductivity (see next section). The formation energy of V_N decreases with the Fermi level moving towards the valence band maximum and it has a low formation energy in *p*-type GaN, making them a likely compensating center in the case of acceptor doping. On the other hand, the gallium vacancy (V_{Ga}) is the lowest energy defect in *n*-type GaN, where it acts as a triple acceptor. This defect plays a role in donor compensation as well as in the frequently observed yellow luminescence. The electronic band structure

of V_{Ga} shows levels within about 1 eV of the valence-band maximum.

1.5.2 Donors in GaN

n-type doping of nitrides has never been a problem; in fact, as-grown material has often exhibited unintentional n-type conductivity. Silicon is the major dopant for n-type GaN since the electron concentration can be controllably changed from $\sim 10^{17}$ to 2×10^{19} cm^{-3} by varying the flow rate of SiH_4 in MOVPE growth [22]. A similar case is applicable to MBE as well. The activation energy of Si_{Ga} donor is 30 meV [23] and it behaves like a standard hydrogenic donor at high pressure. Si_{Ga} is an energetically very stable configuration; the nitrogen substitutional site and the interstitial configurations are energetically unfavorable [24]. Oxygen is present in high concentrations in undoped GaN and it is widely thought to be account for the n-type conductivity in unintentionally doped GaN. The activation energy of the oxygen donor is 33 meV [23]. With increasing concentration of O, the associated donor level moves closer to the conduction band, merging with it at $n_0 > 3 \times 10^{18}$cm^{-3}. Other dopants that have been investigated in order to achiev n-type conductivity include Se and Ge, both shallow donors. Free-electron concentrations in Se or Ge doped samples of up to 10^{19}cm^{-3} can easily be achieved.

1.5.3 Acceptors in GaN

There has been much effort aimed at doping GaN and its ternaries p-type by introducing group-II and group-IV elements. However, Mg is the only dopant that enables one to obtain reproducible p-type conductivity. Many other potential dopants, including Li, Na, K, Be, Zn, Ca, Cd, and C, have also been incorporated into GaN (a recent review of dopant related luminescence, see Ref. [25]). Some dopants have been observed to compensate electrons in GaN effectively, leading to highly resistive material. Although Mg is a shallow acceptor with an ionization energy of $\sim$ 200 meV [26, 27], the early attempts with Mg doping were not successful, mainly for three reasons: (i) Hydrogen which is always present in

MOVPE and HVPE growth forms an electrically inactive complex with Mg; (ii) heavily doped GaN is notorious for self-compensation; (iii) the large lattice mismatch and the large difference in thermal expansion coefficients between GaN films and the sapphire substrate also contributes to the difficulty of obtaining high quality and *p*-type GaN films. Through several decades' effort, the surface morphology was markedly improved, firstly by introducing an AlN buffer layer initially deposited on the sapphire substrate [28, 29]. Amano *et al* [30, 31] then discovered that *p*-type GaN film can be obtained by growing Mg-doped GaN films with AlN buffer layer and performing low-energy electron-beam irradiation (LEEBI) treatment after growth . By using a GaN buffer layer instead of an AlN buffer layer, Nakamura *et al* [32, 33] further improved the crystal quality. The same authors also discovered that N_2-ambient or vacuum-ambient thermal annealing at temperatures above 700°C is effective in obtaining low-resistivity *p*-type GaN films identical to those produced by the LEEBI treatment [34]. It was confirmed later that *p*-type GaN is produced principally through thermal annealing, and that LEEBI creates similar conditions as thermal annealing due to electron beam heating [35, 36]. The discovery of the effect of annealing for the activation of Mg acceptors contributes substantially to the commercialization of this material system for applications such as blue and green LEDs. In GaN : Mg grown by MOVPE, the concentration of free holes at room temperature reaches its maximum value at about $10^{18}cm^{-3}$, and it decreases with further increase of Mg concentration [37] due to the self-compensation mechanism.

Chapter 2

The ODMR technique

2.1 Introduction

Optically Detected Magnetic Resonance (ODMR) is a well-established technique to investigate recombination processes in semiconductors [38, 39, 40, 41]. The technique is essentially a combination of Photoluminescence (PL) and Electron Spin Resonance (ESR) methods. It provides the high sensitivity of PL and the high resolution of ESR. Unlike ESR, which probes the ground state of the system, ODMR provides a way to obtain information from the excited states of defects and impurities in semiconductors. The earliest studies of ODMR in solids were carried out by Geschwind *et al.* (1959) in the ^{2}E state of Cr^{3+} ions in ruby.

The ODMR method has already been applied to studies of GaN. The PL spectra of GaN and its alloys are always dominated by broad overlapping bands so that it can be difficult to assign a particular luminescence band to particular optical centres. ODMR provide information on the excited state of defects through obtaining the values and angular dependencies of the Zeeman splitting (g tensor). The spin Hamiltonian parameters of the defect can be decided and the symmetry of the defect can be revealed. It relates detailed microscopic structures of centres to their particular luminescence spectra. In some cases the hyperfine interaction can be resolved, which arises from the interaction of the electron-spin magnetic

dipole with nuclear-spin magnetic dipoles in its vicinity. Thus we can establish whether the defect is on the Ga, N, or interstitial site. It has proved to be a technique employed to discriminate precisely centres involved in recombination processes. For recent reviews of ODMR in wide band gap materials, see Refs. [41] and [42].

2.2 Introduction to ODMR

2.2.1 Magnetic resonance

If we assume that atoms (or ions) with an angular momentum have a magnetic moment, given by Eq. 2.1:

$$\mu = \gamma \mathbf{L}, \tag{2.1}$$

where μ is the magnetic dipole moment, $\mathbf{L}$ the angular momentum, and γ the magnetogyric ratio, which is of order (e/mc) for electrons, the torque ($\mathbf{G}$) on the moment subject to an external magnetic field ($\mathbf{B}$) is

$$\mathbf{G} = \mu \times \mathbf{B}. \tag{2.2}$$

The equation of motion is therefore

$$\frac{d\mu}{dt} = \gamma \mu \times \mathbf{B}. \tag{2.3}$$

The magnetic dipole μ then processes uniformly about the field with angular velocity $\omega_L = -\gamma \mathbf{B}$. The precession produces an oscillatory magnetic moment normal to the external magnetic field $\mathbf{B}$. It can interact with another oscillatory

magnetic field $B_1 \cos\omega t$ provided by the microwave radiation and the field is normal to **B**. When the microwave frequency ω is equal to the natural precession frequency ω_L, the interaction has a marked effect, that it changes the energy of the dipole, which is $E = -\mu \cdot \mathbf{B}$, by an amount of $\hbar\omega$. This effect is known as "magnetic resonance".

2.2.2 General principles of ODMR

The general principles of ODMR can be understood by reference to Fig. 2.1. In quantum mechanics, electrons (or holes) have discretely quantized angular momentum known as spin. Spin is intrinsic property of electrons and for a free electron, the spin is 1/2 (in units of $\hbar$). The ODMR technique is based on spin selection rules existing in electron-hole recombination processes. The spin selection rules govern transitions between electron energy levels, in that allowed transitions must involve the promotion of electrons without a change in their spin, i.e., $\Delta S = 0$. In an external magnetic field **B** the energy level degeneracy of different electronic spin states is lifted. The spin-dependence of recombination process may cause recombination to occur faster from some spin levels than from others. As a result, there are always differences between the populations of various spin levels of excited states.

The intensity or polarization of the accompanying photoluminescence is dependent on the population distributions among the spin states, and can be changed with the effect of microwave resonance. Microwave resonance occurs when the microwave quantum energy $h\nu$ matches the separation of different spin levels. It induces carrier transitions between the levels. For a single free electron, the resonance between the adjacent spin-up (M_S = 1/2) and spin-down (M_S = -1/2) levels can be expressed as

$$\Delta U = h\nu = g_e \mu_B \mathbf{B} \tag{2.4}$$

where ΔU is the energy difference between adjacent spin states, g_e is the Zeeman splitting constant for the free electron, μ_B is the Bohr magneton, and **B** desig-

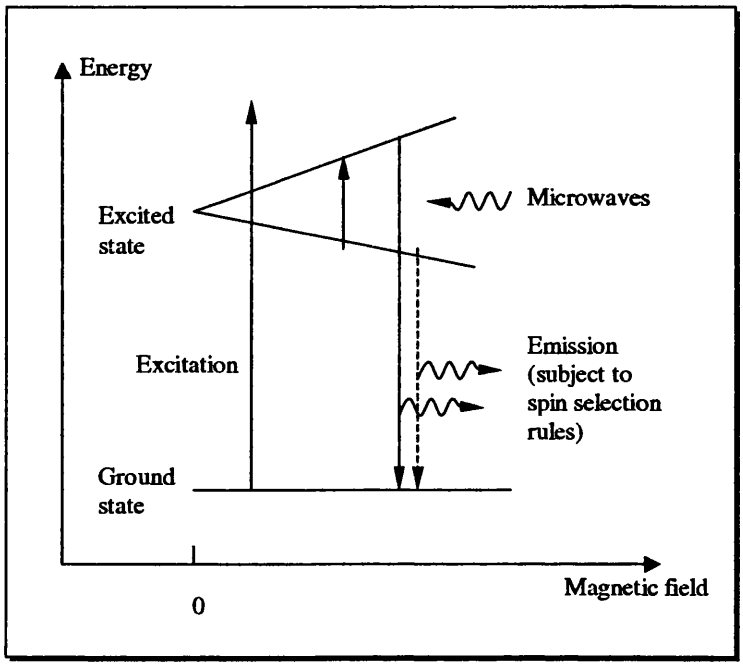

Figure 2.1: Schematic diagram to illustrate the principles of ODMR experiments. The recombination probability of the radiative decay transitions shown by solid line is assumed to be much bigger than that shown by the dashed line.

nates the external magnetic field that satisfies the resonance condition. When magnetic resonance occurs between two spin levels, the tendency is always to equalize the populations of them. It follows that magnetic resonance transitions affect the emission, which can be detected optically. The changes in PL are monitored as the magnetic field is swept and constitute the ODMR spectrum. In most cases, increases in the intensity of the PL (PL-enhancing) are obtained and positive ODMR signals are observed. However, the behaviour can be more complicated, with magnetic resonance causing the transfer of carriers into a process in competition with the PL that is monitored. It then causes decreases in the emission intensity and therefore, negative (PL-quenching) signals can also be observed. Even more complicated, in the presence of the background signals, the resonance ODMR signal may appear as either a positive or negative signal, merely as a consequence of the relative magnitude of the rate constants involved in the problem [43]. The modulation of the PL under magnetic resonance conditions is in the range of $0.1 - 0.01\%$.

2.2.3 The g-factor

2.2.3.1 Effective g-factor

The Zeeman splitting constant for the free electron

$$g_e = 2.002319304386(20) \tag{2.5}$$

is one of the most accurately known of the physical constants. When put in an atom, the electrons (or holes) can no longer be considered free. They are in a magnetic field produced by the orbital motion. This local field interact with spins and the total Hamiltonian of the electrons is modified. This effect is called spin-orbit coupling, which gives the deviation of the g-values for a particular centre from the free electron g-value. In an ODMR measurement, the spin species are in an effective magnetic field expressed as

$$\mathbf{B}_{eff} = \mathbf{B} + \mathbf{B}_{local} \tag{2.6}$$

where $\mathbf{B}$ is the magnetic field applied externally to the sample and $\mathbf{B}_{local}$ is the local magnetic field which can be induced by the orbital motion or magnetic nuclei. In principle the field $\mathbf{B}$ in Eq. 2.4 should be replaced by $\mathbf{B}_{eff}$; in usual practice it is more convenient to retain the external magnetic field $\mathbf{B}$ and replace g_e by the effective g-factor. Thus we can write Eq. 4.5 as

$$\mathbf{B}_{eff} = (g/g_e)\mathbf{B} \tag{2.7}$$

and Eq. 2.4 becomes

$$\Delta U = h\nu = g\mu_B\mathbf{B} \tag{2.8}$$

In this way the local magnetic field is taken into account by the effective g-factor.

The g-factor was first introduced by A. Landé in 1921, who showed that when both orbital and spin momentum are present, the value of g depends on the nature of the coupling between them. The value of g is given by the formula:

$$g_J = \frac{3}{2} + \frac{S(S+1) - L(L+1)}{2J(J+1)}, \tag{2.9}$$

where J, S, and L are quantum numbers representing respectively the total angular momentum, the electron spin and orbital momentum. For a free electron whose orbital momentum $L = 0$, the pure spin g-factor is then very close to 2.

Theoretically the conduction band g-factor can be estimated by the **k·p** perturbation theory. The method requires only a small number of experimentally determined band gap values and optical matrix elements and therefore is particularly useful for interpreting optical spectra. Similar to calculation of effective mass, the following three-band approximation of the effective g-factor is obtained [44]:

$$g_c = 2[1 - \frac{E_P \Delta_0}{3E_0(E_0 + \Delta_0)}] \tag{2.10}$$

where E_0 is the band gap energy, Δ_0 is the spin-orbit splitting and E_P is the momentum matrix element.

Usually in semiconductors donors show g-values smaller than free electrons, and acceptors have a positive g shift. However, there are exceptions to this simple rule [45]. Like effective mass, the effective g-factor provides information about the conduction or valence band structure and is sensitive to applied perturbations like strain, quantum confinement or electric fields.

2.2.3.2 g anisotropy

The simplest resonance expression $\Delta U = h\nu = g\mu_B \mathbf{B}$ (Eq. 2.8) with a numerical value of g is applicable only to an isotropic system, such as a cubic crystal in which there is octahedral symmetry about any normal lattice site. With different orientations of the external magnetic field $\mathbf{B}$, the effective magnetic field $\mathbf{B}_{eff}$ may have different effects on the spins. Therefore the line positions of the ODMR spectra may change with the crystal orientation relative to the magnetic field $\mathbf{B}$. In this case the effective g-factor should be expressed as a tensor. A truly isotropic system is one for which

$$g_X = g_Y = g_Z \tag{2.11}$$

where X, Y and Z are the principal axes of the paramagnetic species. For an unpaired electron at such a site, the spin Hamiltonian has the form

$$H = g\mu_B(B_X S_X + B_Y S_Y + B_Z S_Z) \tag{2.12}$$

The lattice structure of GaN is known as Wurtzite and defects in GaN may be of tetragonal symmetry. For such a system, the g-factor is given by the positive square root of

$$g^2 = g_\perp^2 \sin^2\theta + g_{||}^2 \cos^2\theta \tag{2.13}$$

where

$$g_\perp = g_X = g_Y \neq g_Z = g_{||} \tag{2.14}$$

and θ is the angle between $\mathbf{B}$ and the symmetry axis of the defect. The spin Hamiltonian is

$$H = \mu_B[g_\perp(B_X S_X + B_Y S_Y) + g_{||} B_Z S_Z] \tag{2.15}$$

For systems with rhombic or lower symmetry, where the X and the Y axes are no longer equivalent, the spin Hamiltonian is the following,

$$H = \mu_B(g_X B_X S_X + g_Y B_Y S_Y + g_Z B_Z S_Z) \tag{2.16}$$

and the effective value of g for an arbitrary orientation is then given by

$$g^2 = g_X^2 \cos^2\theta_{BX} + g_Y^2 \cos^2\theta_{BY} + g_Z^2 \cos^2\theta_{BZ} \tag{2.17}$$

where θ_{BX}, θ_{BY} and θ_{BZ} are, respectively, the angles between the field **B** and the X, Y, and Z axes.

Since the lattice structure of the material studied is normally known, the orientation dependence of ODMR spectra can help to locate the position of particular defects in the lattice.

2.2.4 Donor-acceptor recombination

Donor Acceptor Pair (DAP) transitions appear when electrons on the neutral donor sites recombine with holes on the neutral acceptor sites. The DAP transition energy is given by

$$E(r) = E_g - (E_A + E_D) + \frac{e^2}{4\pi\varepsilon_0\varepsilon_r r} \tag{2.18}$$

where E_D and E_A are the donor and acceptor binding energies and the last term is the Coulomb interaction contribution resulting from the interaction of ionized donors and acceptors in the initial state.

The ODMR technique is widely applied to investigate donor-acceptor recombination processes in semiconductors because of the long lifetime of the processes

(e.g., the yellow luminescence band of undoped GaN has a lifetime distribution extending to the millisecond range; the effect of recombination lifetime on ODMR sensitivity will be discussed in Sec. 2.3). Both electrons from donors and holes from acceptors have effective spins of 1/2 before recombination. Under an external magnetic field, the energy level degeneracy of different spin states of both the donors and the acceptors is lifted. Electrons and holes may prefer energetically to occupy different spin states. As a result the recombination probability of them will be small. Under magnetic resonance conditions, either the electron spin or the hole spin is flipped. The recombination probability can be therefore increased dramatically and PL enhancing signals can be detected.

If the concentration of neutral donors and acceptors is sufficiently low (which is normally true in the case of GaN), the relative probability of recombination with a centre other than the nearest one is vanishingly small. Under this circumstance it is appropriate to describe energy levels of the excited states in terms of donor-acceptor pairs [46]. Two kinds of cases can be encountered: (a) the exchange interactions of the donors and acceptors are weak and four energy levels are formed by combining the spin states of two centres; (b) the two particles are coupled by a strong exchange interaction and can be described by a triplet state and a singlet. When a donor and an acceptor are well separated (i.e. the exchange interaction between them is weak), four spin levels are formed (Fig. 2.2), which can be written as $|++\rangle$, $|+-\rangle$, $|-+\rangle$ and $|--\rangle$. The symbols present the spin components of the donor and the acceptor and the signs represent the spin magnetic quantum numbers $+1/2$ etc. for the acceptor and donor spins respectively. The spectrum is analysed in terms of the general spin Hamiltonian:

$$H = \sum_{i=x,y,z} (g_{1i}\mu_B B_i S_{1i} + g_{2i}\mu_B B_i S_{2i} + A_i S_{1i} \cdot S_{2i}) \tag{2.19}$$

The first and second terms are the electronic Zeeman interactions of the donor and acceptor spins, respectively. The third term represents the coupling between the two spins, where A is the interaction tensor and is small in this case.

In the cases that the exchange interaction between the two particles are strong, the four levels mentioned above split into a singlet and a triplet (Fig. 2.3). The

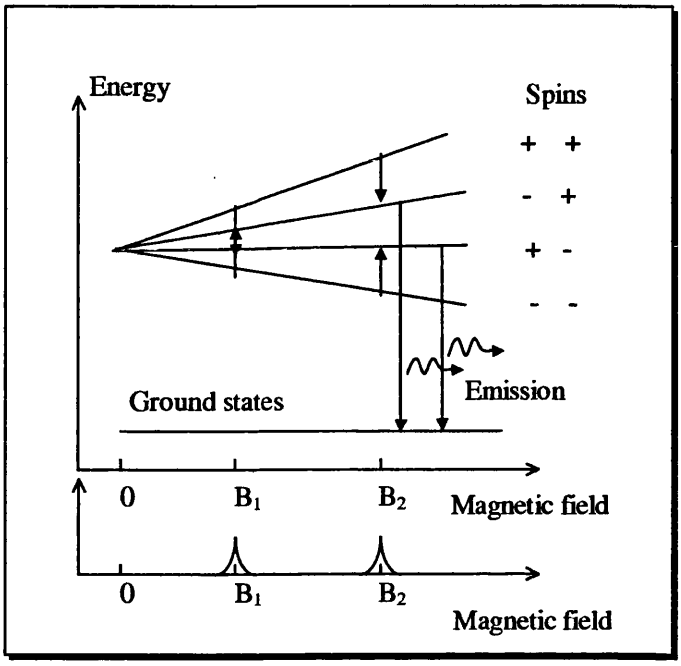

Figure 2.2: Energy levels of a donor-acceptor pair with vanishingly small exchange interaction. Magnetic field is applied along the symmetry axis. The microwave transitions (small arrows) cause increases in emission intensity at the magnetic field value B_1 and B_2.

triplet state itself is characterized by an effective spin of 1 and the spin Hamiltonian becomes

$$H = g_x\mu_B B_x S_x + g_y\mu_B B_y S_y + g_z\mu_B B_z S_z + D[S_z^2 - \frac{1}{3}S(S+1)] + E(S_x^2 + S_y^2) \quad (2.20)$$

where

$$g = \frac{1}{2}(g_D + g_A) \quad (2.21)$$

and g, g_D, g_A are the pair g-value, donor g-value and acceptor g-value, respectively. D is the axial term and describes the magnitude of the zero-field splitting (Fig. 2.3). The last term is necessary if a further reduction in symmetry from axial to rhombic is observed.

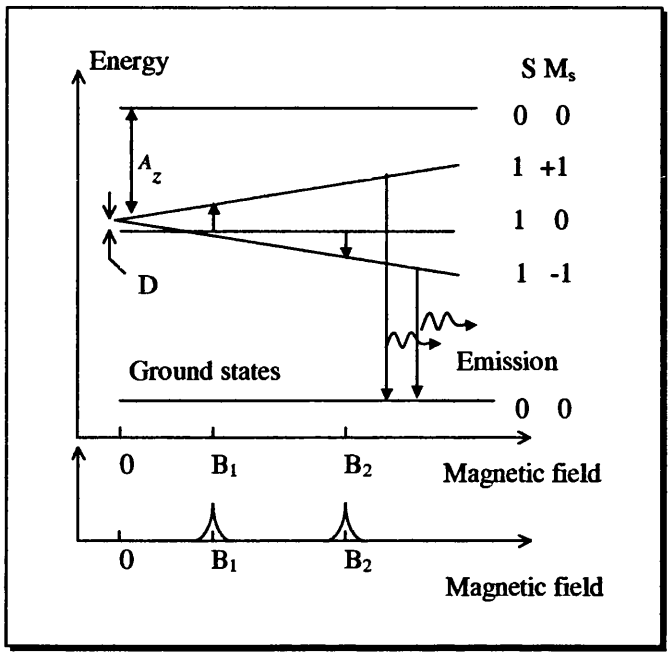

Figure 2.3: Energy levels for a system, which has triplet and singlet excited states, the triplet being the lower. Magnetic field is applied along the symmetry axis. The microwave transitions (small arrows) cause increases in emission intensity at the magnetic field value B_1 and B_2.

2.3 Experimental arrangement

Fig. 2.4 shows the schematic apparatus for our ODMR system. The system uses a split-coil superconducting magnet. The maximum field is 3 Tesla. The most outstanding feature of a superconducting magnet is its ability to support a very high current density with a vanishingly small resistance. This characteristic permits magnets to be constructed that generate intense magnetic fields with little or no electrical power input. This feature also permits steep magnetic field gradients to be generated at intense field and high stability of the field that is superior to the use of ferromagnetic materials.

The detection of ODMR signals requires a system including three necessary channels: a microwave radiation channel and channels for optical excitation and detection. The microwave source, which is a multiple transistor oscillator, emits monochromatic radiation. Our present microwave systems in Bath operate at

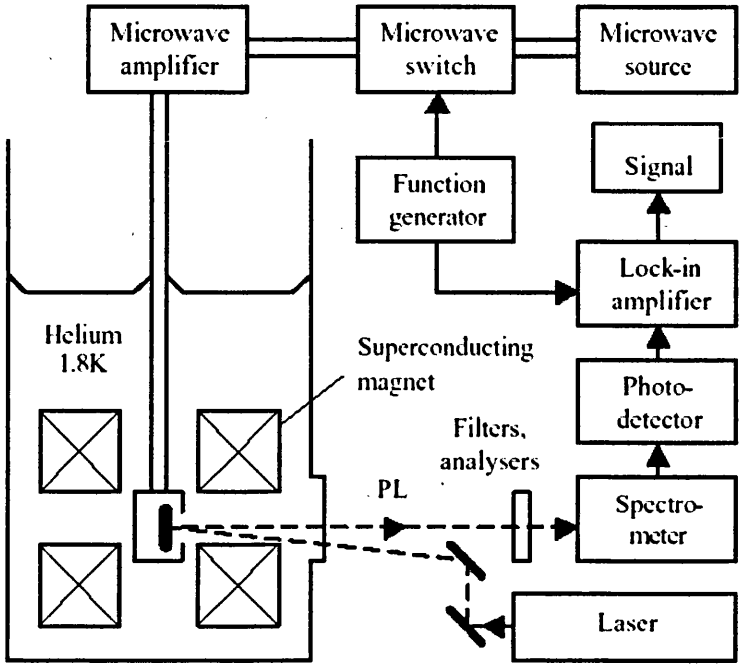

Figure 2.4: Schematic apparatus for ODMR.

14, 34 and 100 GHz with powers of $\sim$ 50, $\sim$ 60 and $\sim$ 35 mW (but without a resonant cavity for the case of 100 GHz), respectively. The incident microwaves are amplified and chopped at frequencies in the range 200 Hz to 10 kHz by a switch. The microwaves are guided into resonators (in the absence of a sample, Q $\sim$ 3000), which are of rectangular TE_{011} form to maximise the microwave magnetic field B_1 at the position of the sample. An automatic-frequency-control (AFC) system is used to stabilize the microwave frequency, since the energy density in the resonator is very sensitive to the microwave frequency. The resonator has appropriate optical access and could be rotated about an axis perpendicular to the magnetic field. The sample is contained in the microwave cavity and in direct contact with superfluid helium at the nominal temperature of 1.8 K to achieve as large a population difference as possible between the Zeeman levels. In ODMR measurements, the system operates at a fixed microwave frequency and scans the ODMR spectrum by a linear variation of the static magnetic field. It is very difficult to achieve high sensitivity if the microwave frequency is varied. The difficulty arises largely from the fixed-frequency characteristics of the resonant

cavity.

The major requirement of a source for the optical excitation of ODMR experiments is that it should be stable. Lasers are usually employed for excitation since they are reasonably stable and since they provide high power densities at the sample. In our ODMR system, semiconductor samples are excited with the multi-line UV output of an argon-ion laser (363.8 and 351.1 nm) or from a He-Cd laser (325 nm). Typical excitation powers are in the region of 10 mW. The entire sample surface (of area about 10 mm^2) is illuminated with a typical illumination intensity of 0.2 Wcm^{-2}. Light emission from the sample is focused onto a detector by two focusing lenses. Combinations of high- and low-pass interference filters are placed between the lenses and spectral regions of the emission which are of interests are selected. A photomultiplier tube with a S20 response is used for detection in the UV and visible spectral regions and for better sensitivities in the red and near infrared regions, a Si avalanche photodiode (APD) is used. In some cases a monochromator may be used instead of the filters and the ODMR spectral dependence under a resonance condition can be examined. The signals from the detector are processed by a phase sensitive detector (PSD) in coherence with the chopping of microwaves. The signals from the PSD then correspond to the change in the intensity of the emission with and without microwave excitation.

There are several experimental parameters that affect the sensitivity of the experiment. The most important parameter is the lifetime of the optical excited state (t_r). It is essential to maintain a sufficient population at the excited state of interest. Generally if $t_r \leqslant 1\mu s$ the steady state population achieved by optical excitation may be too little for the necessary sensitivity to be achieved [41]. The lifetime of excitons, as an example, is normally too short to allow for ODMR experiments with standard ODMR set-up. Therefore the technique is not suitable for the studies of near-bandgap luminescence of the free or bound excitons. On the other hand, Spin-lattice relaxation tends to re-establish thermal equilibrium, with which the lowest-lying level has the greatest population as a result of the Boltzmann distribution. The population of the two-spin states might be changed so that ODMR signals can be affected. To prevent this it is advantageous if the spin-lattice relaxation time is long compared to the recombination time. This is the reason that usually an ODMR measurement is carried out at

helium temperature, with samples directly contacting with liquid helium.

2.4 Background signals in ODMR

In many ODMR studies, the magnetic resonance signals are superimposed on non-resonant background signals. The origin of the background signal is a component of PL modulated by the chopped microwaves at any magnetic field **B** even without the spin resonance condition being met. The background signal shows normally only a weak dependence on external magnetic field. They are usually assigned to the absorption of microwave power in the sample via a cyclotron resonance, leading to a heating of the electronic system; the effects of heating can be complicated since a raised temperature will generally reduce the PL quantum efficiency but may also shift the carrier population balance in favour of the radiative recombination channel that is being monitored. The absorption of the microwaves power can also give rise to impact ionisation of centres [47, 48], including those monitored via the PL, so that an ODMR background signal can result from this non-thermal mechanism. The presence of background signals can have a profound effect on the magnitudes and signs of the ODMR signals themselves [43].

Chapter 3

Origin of red luminescence in Mg doped GaN

3.1 Introduction

The *p*-type doping of GaN with Mg has achieved substantial progress. Room temperature free hole concentrations of the order 10^{18} cm^{-3} have been realized, which is sufficient for many applications. However, a self-compensation mechanism, in which deep defects are formed to compensate the doping effects, begins to appear even at low doping concentrations and further improvement of carrier concentrations is restricted, which constitutes an impediment for progress in device applications. Deep defects also play a key role in the performance limits and aging effects of devices. The red (1.8 eV) luminescence band is often observed in Mg-doped GaN and is suggested to be related to deep defects on the basis of photoluminescence and magnetic resonance studies [49, 50, 51, 52]. It has been proposed that vacancy-dopant complexes are involved, with $V_N - Mg_{Ga}$ as a deep donor and V_{Ga} related complexes as deep acceptors [49, 50]. This suggestion is mainly based on previous experiences of II - VI (rather than III - V) compounds and direct experimental confirmation is therefore needed. The $V_N - Mg_{Ga}$ defect, formed by self-compensation, has also been suggested to be the deep donor involved in the 2.8 eV band in Mg-doped GaN [53, 54]. The

proposed donor-like behavior of this defect is, however, in contradiction to the fact that it can be observed by positron annihilation spectroscopy (PAS) [55], since in PAS only neutral and negatively charged defects can be detected. Furthermore, theoretical calculations based on self-consistent local-density-function theory are consistent with the PAS results in that a neutral charge state of the defect is energetically favored [56]. The neutral state of the defect is formed presumably by associating two electrons with the nitrogen vacancy and therefore should be acceptor-like. The apparent discrepancy of the charge states of the $V_N - Mg_{Ga}$ center can be reconciled by introducing the model that, under most conditions, the defect will exist in the neutral "ground" state (which is the case when PAS experiments are performed) while, under laser excitation, it is transferred to a singly charged excited state which can participate in optical processes as a donor. To test this proposal and give further experimental substantiation of the origins of the red emission, PAS, together with photoluminescence (PL) and optically-detected magnetic resonance (ODMR) experiments have been performed to investigate one undoped and several Mg-doped GaN epitaxial layers with different Mg concentrations before and after thermal activation.

3.2 Experimental Details

The GaN samples were grown on *c*-plane sapphire substrates in a Thomas-Swan close-coupled showerhead reactor operating at low pressure. The typical V/III ratio is ~ 2000 and the growth rate is $\sim 2.3\ \mu mh^{-1}$. The Mg-doped layers were of thickness 1.5 μm and were grown at a temperature of 1047°C directly onto a thin nucleation layer of GaN grown at 525°C. The Mg precursor flow rates were 75, 100, 200 and 300 sccm (samples #626, #625, #624 and #623 respectively) producing a range of Mg concentrations; these were not determined directly but are expected to increase monotonically with the precursor flow rate. All the as-grown samples are highly resistive. Annealing was carried out in a horizontal tube furnace at 850°C for 20 minutes. The O_2 concentration in N_2 was 0.5%. Afterwards all the samples exhibited *p*-type conductivity. A nominally undoped highly resistive sample (#621) grown under the same conditions, was also studied for comparison.

The low temperature PL spectra were obtained at 10.5 K with 325-nm He-Cd laser excitation and conventional single-grating spectrometer. The PL intensity were monitored with an S20 response photomultiplier (in the UV and visible) or a Si avalanche photodiode (in the red and near infrared). All the spectra are uncorrected for the system response. The ODMR measurements were carried out with microwave frequencies in the 14 GHz bands. Optical excitation of the ODMR was provided by a multi-line UV argon ion laser (dominant lines at 351.1 and 363.8 nm). The microwave excitation was chopped at low frequencies (typically ~600 Hz). The description of the ODMR systems can be found in Chapter 2.

PAS with a slow positron beam is an effective tool for the investigation of open volume defects such as neutral or negatively charged vacancies in semiconductors. When positrons annihilate electrons in semiconductors, the resulting gamma ray spectrum is Doppler broadened (since the electrons have a range of momenta). If the positrons become trapped in vacancy-type defects, the energy spectrum of the gamma rays becomes narrowed. The narrowing is characterized by a quantity S, defined as the ratio of the central area of the energy spectrum to the total area under the spectrum. The value of S is characteristic of the material under study, but is higher when vacancies are present [57]. Measurements of S can thus be used to monitor vacancy concentrations. In the present work, single-detector Doppler-broadening PAS was performed using a magnetic transport positron beam system [58]. GaN samples were studied by positrons implanted into the samples at energies in the range 0.1 - 30 keV, corresponding to mean depths up to 1.5 μm.

3.3 Experimental results and discussion

3.3.1 PL

Typical PL spectra of the samples under study are shown in Fig. 3.1. From the undoped sample several excitonic luminescence features were observed with the dominant peak at 3.483 eV (Fig. 3.1(d)). There are two additional

broad bands, known in the literature as the "blue" band and the "yellow" band which have been observed in undoped or Si doped samples, peaking at approximately 3.0 eV and 2.25 eV, respectively. The blue band is attributed to donor-acceptor recombination emission [59] and several studies suggest that Ga vacancy (V_{Ga})-related complexes play a role [60, 61, 62]. The yellow band is very often present in undoped GaN and its origin has been under intensive debate. It is now widely accepted that V_{Ga} or related complexes contribute to the yellow luminescence as deep acceptors [18, 63, 64]. The existence of the blue and yellow bands therefore verifies the presence of V_{Ga} in the undoped sample.

For the Mg-doped samples, we observed (Figs. 3.1(a) and (b)) a broad band with estimated zero phonon (ZP) energy at around 3.3 eV (clearest in our spectra for the as-grown samples #625 and #626). This has been attributed to the recombination of electrons from shallow donors with holes from neutral Mg acceptors [49, 66, 53, 67]. It has been suggested that the shallow donors are residual donors such as Si_{Ga} [68], O_N [69] or $V_N - H$ complex [53]. The explanation in terms of $V_N - H$ complex is favored in this work since the 3.3 eV band disappears after annealing, indicating that the centres dissociate with thermal activation in a hydrogen-free atmosphere. There is a second broad band peaked at 2.8 eV, which is referred to often as the "blue band" in Mg-doped samples and has been observed previously to dominate the spectra of the samples having the highest Mg content [49, 54]. This observation is confirmed for the present series of samples. This 2.8 eV band has been the subject of considerable discussion and is generally believed to be due to recombination involving deeper donors and Mg acceptors [49, 53, 67, 70, 71, 72]. The band becomes dominant after annealing (Fig. 3.1(b)). In addition to the 3.3 eV and 2.8 eV bands, the as-grown samples exhibit a broad red luminescence band peaked at $\sim$ 1.8 eV. The red PL band, which is strongest in the lightly doped material, becomes weaker as the Mg concentration is increased and vanishes after annealing.

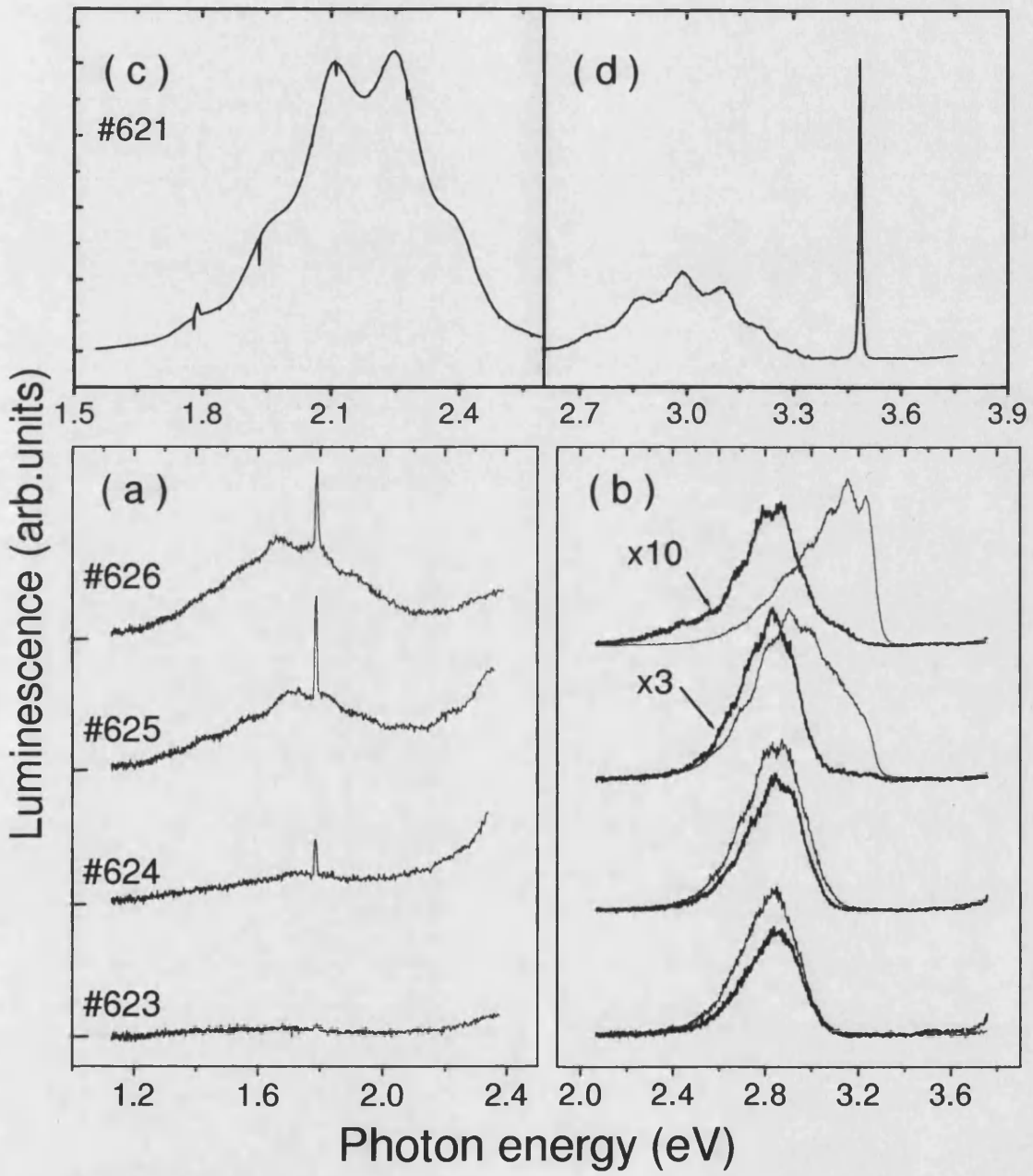

Figure 3.1: (a) and (b) PL spectra at 10.5K from the GaN : Mg samples grown with different Mg precursor flow rates increasing from #626 to #623. In (b) the effects of annealing on the PL in the blue/violet region are shown (spectra after annealing are shown by the thick lines). Panels (c) and (d) show the PL from an undoped as-grown specimen (#621). The sharp peak at 1.79 eV is the well known $^2E(\bar{E})$–$^4A_2$ (or R_1) line (see for example Ref. [65]) of Cr^{3+} in Al_2O_3 emitted from a sapphire substrate. The structure in the wide PL bands is due to interference effects.

3.3.2 ODMR spectra

The ODMR signals detected in the 1.77 - 1.91 eV spectral region of the four as-grown Mg-doped samples are shown in Fig. 3.2. Both PL-enhancing and PL-quenching signals are observed. The sharp enhancing signal in the middle of the spectra is isotropic with $g_{||}, g_{\perp} = 2.003 \pm 0.003$ and FWHM = 5 mT. The g-value and width correspond closely to those of the so-called MM1 center [51, 52]: it is PL-enhancing only when detecting via the red band and has been attributed[51, 52] to deep defects with an energy level in the lower midgap region. At the high field side of the sharp signal the other two overlapping luminescence-enhancing resonances are observed, which are better resolved in measurements performed at 34 GHz (reported in Chapter 5). From comparison with previous magnetic resonance work [51, 67, 73, 74], the narrower resonance, with $g_{||} = 1.952 \pm 0.003$ and FWHM = 8-10 mT, is attributed to effective-mass (EM) donors. The g-value of the broader signal ($g_{||} = 1.967 \pm 0.005$) is very close to that of a deeper donor signal detected on the 2.75 - 3.1 eV spectral region of both the as-grown and annealed samples that we have studied (signal (vi) in Chapter 5), suggesting that the same deeper donor is probably associated with both the 2.8 eV "blue" band and the 1.8 eV "red" band. In addition to the luminescence-enhancing lines an asymmetric quenching signal with a g-value about 2.105 is detected, and is attributed to shallow Mg acceptors [67]. The luminescence-quenching character indicates that it is a center involved in a recombination process competing with the red emission. The ODMR results presented above suggest that donor (EM and/or deeper)-to-deep-acceptor recombination is responsible for the red emission. As in the PL spectra, the ODMR signals in the red become weaker as the Mg concentration is increased. The signals do not exist in undoped samples and, in doped samples, are suppressed after annealing.

According to theoretical studies the deep compensating defects in GaN are dopant-vacancy associates [17, 18]. In p-type GaN the N vacancy (V_N) has the lowest formation energy while in n-type the Ga vacancy (V_{Ga}) dominates. Previous studies suggest that V_{Ga} is a deep acceptor and leads to an energy level in the lower part of the band gap, about 1.0 eV above the valence band [75, 76]. On the other hand $V_N - Mg_{Ga}$ is predicted to be a donor with an energy level

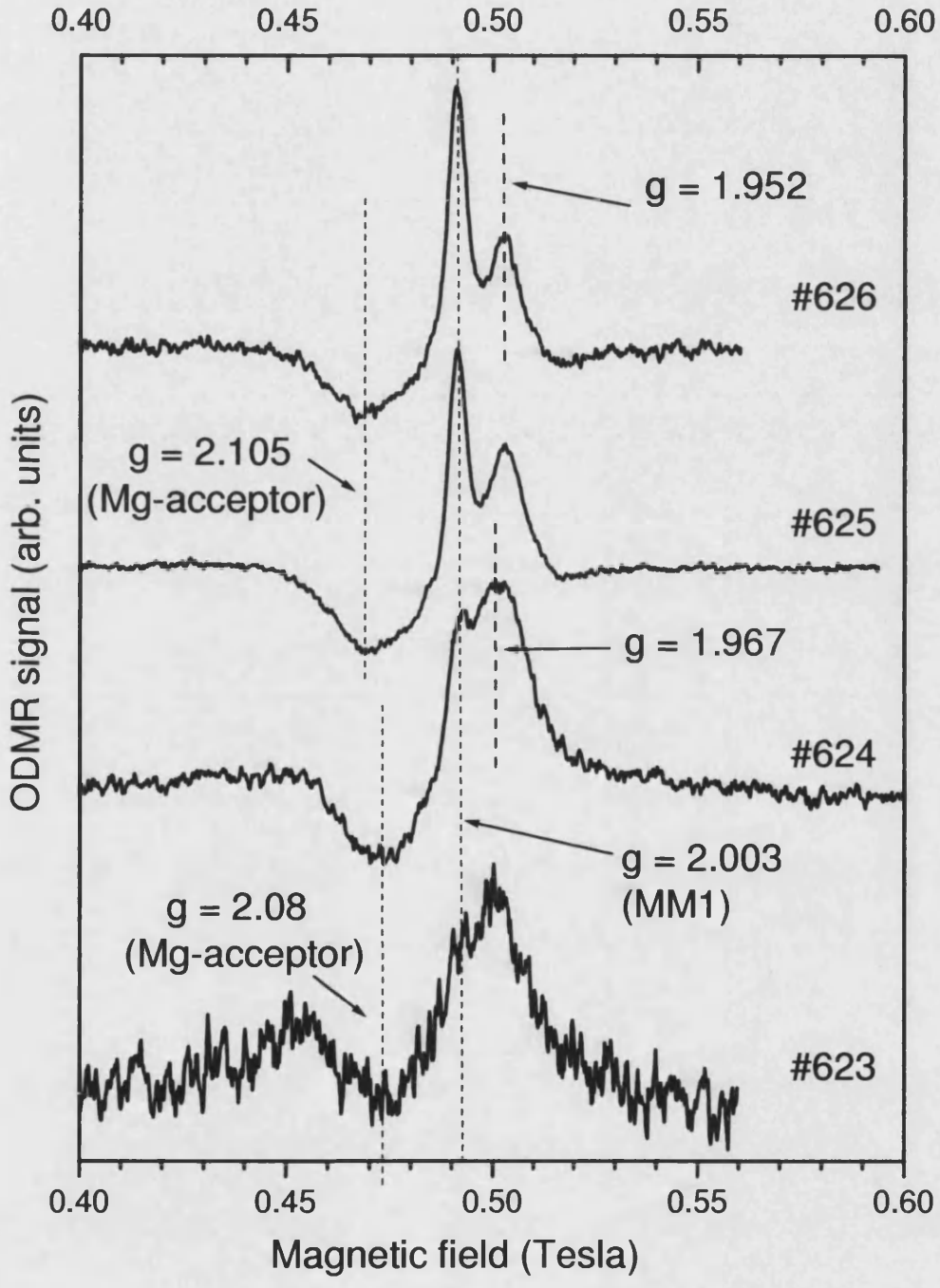

Figure 3.2: ODMR spectra detected on the 1.77 - 1.91 eV red region for samples #626, #625, #624, and #623 with Mg concentration increasing from #626 to #623. The arrows indicate the g-values at $\mathbf{B}||c$ obtained using a Lorentzian multipeak fitting procedure and correspond to the resonances indicated by vertical lines.

at $\sim$ 280 meV below the conduction band [54]. The energy levels of V_{Ga} and $V_N - Mg_{Ga}$ make them appropriate candidates for the defect centers involved in the 1.8 eV red emission. Furthermore, $V_N - Mg_{Ga}$ is suggested to be the donor involved in the 2.8 eV band in Mg-doped GaN [53, 54], which has a very similar g-value to that of the deeper donor in the red band in the present work.

3.3.3 PAS

In GaN, both V_{Ga} [63] and $V_N - Mg_{Ga}$ [55] have been observed in previous PAS studies. The results of the present slow positron measurements are presented in Fig. 3.3(a). The S parameters of the four Mg-doped as-grown samples, along with those of the lightly Mg-doped annealed sample and of the undoped reference sample, are shown as a function of positron implantation energy. The corresponding mean depths probed are also shown. For the undoped and the annealed samples, as the positron implantation energy increased, the S parameters firstly decrease from the surface specific value (i.e., at low energy) and become approximately constant at around 0.420 above 2.5 keV. This indicates that at this energy most positrons are annihilated in the GaN film. The S parameters rise slightly as the positron energy increases from 2.5 keV to 18 keV, suggesting that the vacancy concentration increases as the depth is increased from about $\sim$ 30 nm to $\sim$ 700 nm. The observation here agrees with a previous report [77] suggesting that vacancies prefer to reside alongside dislocations, since dislocation densities increase towards the interface of the film and the nucleation layer. Beyond 18 keV measurable annihilation starts to take place in the sapphire substrate and S parameters fall towards the value characteristic of the sapphire substrate (measured separately to be 0.392). Fig. 3.3(b) shows S_b as a function of Mg concentration, where S_b is taken as the average of the S parameter measured in the energy range from 12 keV to 18 keV and represents the bulk film value. The S_b value of the undoped sample is slightly bigger than that of the annealed one. For the lightly Mg-doped as-grown samples #626 and #625 the highest S_b values are observed. With the increase of Mg concentration S_b decreases and the shape of the S curves approaches those of the undoped and the annealed ones. The trends of S_b with doping and annealing (increasing with light Mg-doping, decreasing when Mg concentration is further increased and becoming suppressed

after annealing) are very similar to the trends in the strength of the red luminescence (shown also in Fig.(3.3(b)) and of the ODMR signals detected in the red spectral region. The first observation of this strong correlation between the PAS and the PL/ODMR data thus provides strong support to the red emission being associated with vacancy-type defects.

As noted in section III.A, the low-temperature PL results suggest the existence of V_{Ga} in undoped samples. It has previously been proposed that Mg doping reduces the concentration of V_{Ga} in GaN [77, 78, 79] and S_b in Mg-doped samples is normally lower than in undoped ones. However, in our case the values of S_b for all the Mg-doped as-grown samples are higher than for the undoped sample. This suggests that a second type of vacancy-related defect must be present. Room temperature Hall-effect measurements for the four *annealed* samples show that they are all of p-type conductivity. The resistivity rises progressively as the Mg concentration N_A is increased, indicating that the degree of compensation in the samples is increased. It is suggested that self-compensation limits the hole conductivity in MOVPE GaN : Mg layers and results in a decrease of the hole density after reaching a maximum value $p_{max} \approx 6 \times 10^{17}cm^{-3}$ at $N_A \approx 2 \times 10^{19}cm^{-3}$ [80]. Although N_A was not measured directly in our samples, it is estimated to be of the order of $10^{20}cm^{-3}$ for the heavily doped sample (#623). Hence, self-compensating donors probably exist in reasonable amounts in our samples.

Several studies have suggested that $V_N - Mg_{Ga}$ complexes contribute to the electrical compensation of Mg [49, 53, 55, 80]. The defects exist in a neutral charge state under most conditions and the concentration is predicted to be independent of the Fermi level [56]. For the as-grown Mg-doped samples, although Hall-effect measurements are not possible due to the high resistivity of the samples, the dominant PL bands switch from 3.3 eV to 2.8 eV as the Mg concentration is increased, also indicating the increase of compensating donors. We then conclude that $V_N - Mg_{Ga}$ centers exist in both as-grown and annealed Mg-doped samples and their concentration increases with N_A.

If $V_N - Mg_{Ga}$ were the only vacancy-related defect detectable by PAS measurements in the as-grown samples S_b should have increased rather than decreased

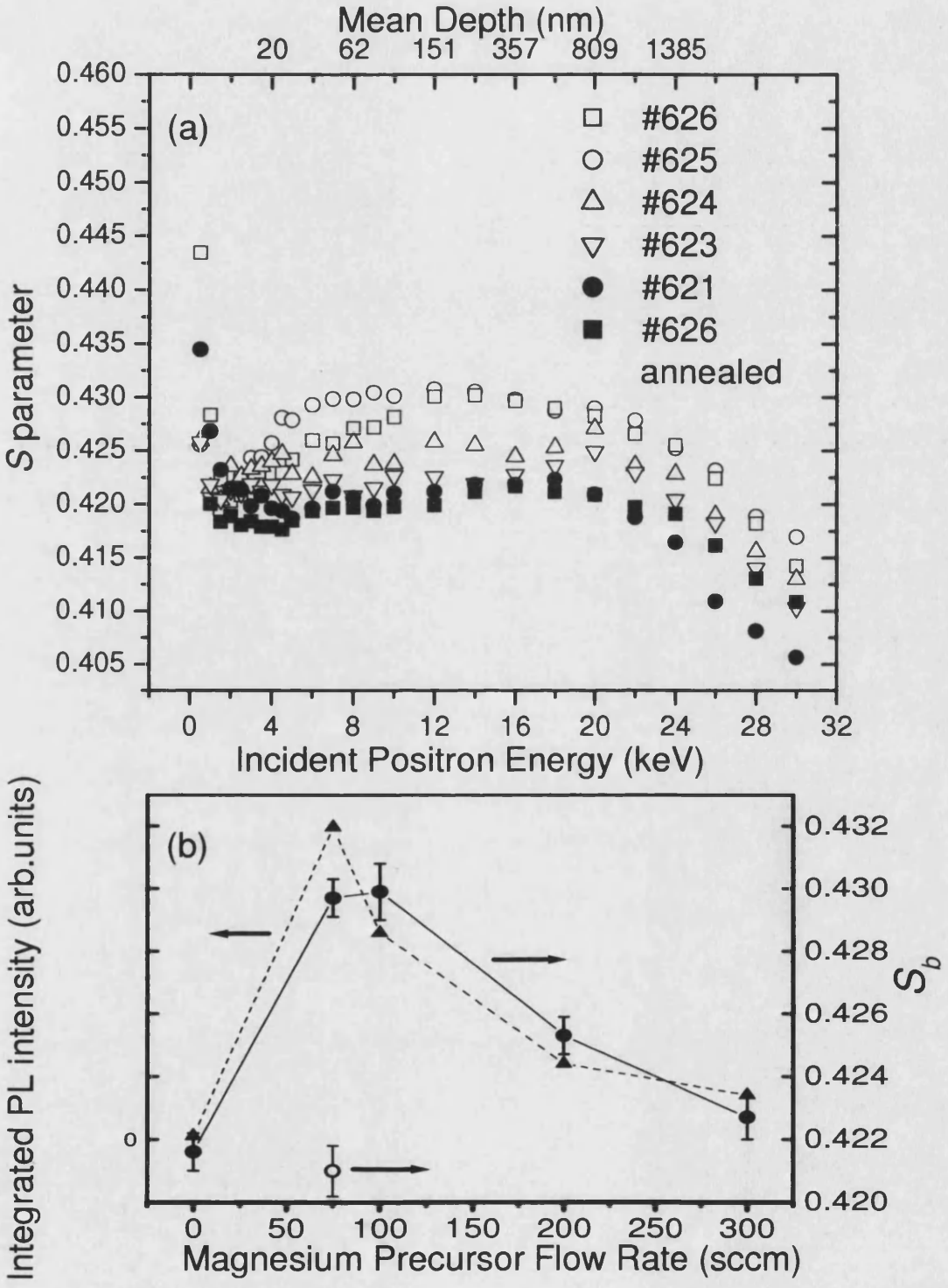

Figure 3.3: (a) The low momentum S parameter versus incident positron energy for the range of as-grown GaN : Mg samples; (b) The change of the mid-range S_b parameter with Mg concentration (filled circles) and the behavior of the integrated intensity of the red emission (filled triangles). The unfilled circle shows the mid-range S_b parameter for the most lightly doped specimen after annealing. The lines are guides to the eye.

at larger Mg concentration. Therefore, V_{Ga} and/or related complexes must also be present in n-type GaN since in such specimens S_b decreases with increasing Mg-doping [81]. Theoretical calculations have shown that the formation energy of V_{Ga} is increased as the Fermi level moves further away from the conduction band towards the valence band [18, 17]. If both $V_N - Mg_{Ga}$ and V_{Ga} are the defect centers associated with the red luminescence the experimental results can be interpreted as follows. In the undoped sample the Fermi level is between the EM and the deeper donor levels. Both V_{Ga} and V_N can be present in reasonable amounts while the V_N centers escape detection by positrons because of their positive charge states. In the lightly doped samples # 626 and # 625 the dopants are either passivated by H atoms [75, 82, 83] or form $V_N - Mg_{Ga}$ centers. Hence the Fermi level is hardly affected and the concentration of V_{Ga} remains high. The neutral ($V_N - Mg_{Ga}$) and negative charged (V_{Ga}) vacancies detected by PAS measurements reach a maximum. The red luminescence channel is switched on, with recombination involving the deeper donors ($V_N - Mg_{Ga}$) and deep acceptors (V_{Ga}). With further increase of Mg dopant the concentration of $V_N - Mg_{Ga}$ continues to increase. The complex is neutral and does not contribute to the carrier concentration itself. The Fermi level moves towards the valence band as a result of the increased contribution of the Mg_{Ga}^- centers. The formation energy of V_{Ga} is increased and its concentration decreases, leading to the decrease of the intensity of the red luminescence. The change of S_b is dominated by that of the V_{Ga} concentration. The overall behaviour is such as to cause the S_b parameter and the intensities of the red PL and the associated ODMR spectrum to pass through the observed maxima. After thermal annealing the samples turn to p-type. The formation energy of V_{Ga} is above 5 eV in p-type GaN under nitrogen-rich conditions [17] and hence they cannot occur in appreciable concentrations. Therefore the red luminescence is suppressed and S_b decreases further. Studies show that $V_N - Mg_{Ga}$ complexes still exist after thermal annealing [53, 80] and they are probably associated with the 2.8 eV luminescence band from the annealed samples.

3.4 Discussion

The findings of our experiments can be summarized as follows: (i) the ODMR data from the red emission point to a recombination process involving electrons from both EM and deeper donors with holes from deep acceptors; (ii) the PAS experiments, together with those of previous studies, show that there are two types of vacancy-related centers in GaN : Mg and that these are likely to be gallium vacancies (V_{Ga}) (or complexes involving gallium vacancies) and complexes formed from nitrogen vacancies associated with substitutional magnesium ($V_N - Mg_{Ga}$), the charge states being either negative or neutral; (iii) that the concentrations of these defects are correlated with the strengths of the red emission and the associated ODMR signals.

The implication of these results is that both the deeper donor and the deep acceptor signals are vacancy related. In the case of the deep acceptor, the evidence points to it being formed by the gallium vacancy, which would be expected to be negatively charged and thus to act as a positron trap. In the optically-excited magnetic state observed in the ODMR spectrum, the vacancy would be expected to contain an odd number of holes and thus to be V_{Ga}^{0} or V_{Ga}^{2-} (in the Sonder-Sibley [84] notation, we write these as $[3h^+]_{Ga}$ and $[h^+]_{Ga}^{2-}$ respectively). Following recombination, it would become V_{Ga}^{-} or V_{Ga}^{3-} ($[2h^+]_{Ga}^{-}$ and $[\ ]_{Ga}^{3-}$ respectively). It is also possible that the deep acceptor is formed from an association between a gallium vacancy and an oxygen ion [72].

The identification of the deeper donor state is more problematic. The suggestion that it is a nitrogen vacancy - magnesium associate was discussed in Ref. [49] and evidence for the existence of such a center was provided by more recent positron studies [55]. The ODMR signals are described by a spin of 1/2, and the g-values are consistent with electrons which are in donor-like orbits. The ODMR thus leads to a model in which the electron responsible for the ODMR signals is trapped in a donor-like orbit by a defect that should have a net positive charge.

In contrast, in order to trap the positrons, the complex needs to be in the neutral (or the unlikely negative) state. The neutral state, in the Sonder-Sibley notation, can be written

$([[\ ]_N^{3+} + [Mg^{2+}]_{Ga}^{-}]^{2+} + 2e^{-})^0,$

in which the two electrons are presumed to be in donor-like orbits. Since these electrons are spin-paired, the neutral deeper donor state (which we write as DD^0) will be non-magnetic and will not lead to ODMR signals. To reconcile these results requires the involvement of a third center. The ODMR spectra show that the usual *EM* donors are also present and we assume that in their neutral state (which we denote by D^0) they contain only one electron (and therefore in this state are magnetic). We can now envisage the following sequence of events. The starting point is:

(i) $D^+ + DD^0(\uparrow\downarrow)_e + A^-$.

Here we assume that the Fermi level lies between the EM and the deeper donor levels; this would be consistent with the high resistivity of the (as-grown) specimens. The symbol A represents the deep acceptor that is involved in the red emission, assumed to be ionized. The arrows indicate the spin states of relevant electrons. Photo-excitation results in transfer of an electron from the acceptor state to the EM donor. If thermalization occurs, this results in neutral EM donors and neutral acceptors in the following spin states :

(ii) $D^0(\downarrow)_e + DD^0(\uparrow\downarrow)_e + A^0(\uparrow)_h$.

If the red emission is due to recombination between electrons from EM or deeper donors with holes from deep acceptors there are now two possibilities. First, the electrons from a *EM* donor could recombine with the hole. If we assume a selection rule in which recombination only between electrons and holes of the same spin direction leads to strong emission, then recombination between the thermalized electrons from the EM donor and the thermalized holes from the deep acceptors is restricted. However, if either spin were to be flipped, the PL would be enhanced (thus leading to the EM donor and deep acceptor ODMR signals). Following this recombination process, the system returns to stage (i).

The second possibility, involving recombination between electrons from the *deeper* donor and holes from the deep acceptor, is not restricted by the spin selection

rules and would lead to

(iii) $D^0(\downarrow)_e + DD+(\downarrow)_e + A^-$,

It is the next stage that is sensitive to magnetic resonance of the deeper donor: it involves a transfer of an electron from the EM to the deeper donor (a process sometimes referred to as "feeding"). Since in stage (iii) the spins of both donors are parallel, the feeding is inhibited. However, magnetic resonance, which flips the spin, would result in either

(iv.a) $D^0(\downarrow)_e + DD^+(\uparrow)_e + A^-$ or

(iv.b) $D^0(\uparrow)_e + DD^+(\downarrow)_e + A^-$.

In either case, the feeding process from D^0 to DD^+ can now occur, leading back to the starting state (i) and thus speeding up the cycle, enhancing the PL intensity. It is also apparent that magnetic resonance in the neutral acceptor state could enhance recombination involving the EM donor at stage (ii). Since the red PL consists of a very broad band, it is not possible to distinguish between the recombination processes involving the EM and the deeper donors.

The sequence would lead to the following characteristics. In the ODMR spectra obtained by monitoring the red emision there would appear PL-enhancing signals from both the EM and the deeper donors; in particular, it would provide a mechanism by which the deeper donor could be detected by ODMR despite the fact that its (two-electron) neutral state is non-magnetic. It would explain the simultaneous appearance in the ODMR spectrum of the enhancing signal due to the deep acceptor. Further, since the red recombination process is in competition with the violet and blue PL processes (which involve shallow magnesium-related acceptors), the appearance of the shallow acceptor signals as luminescence-quenching features is also accounted for.

A one-electron energy level diagram which summarizes the conclusions is shown in Fig. 3.4. The diagram is similar to those in Refs. [49] and [51] , except that the difference in the energies of the EM and deeper donor states in our case needs

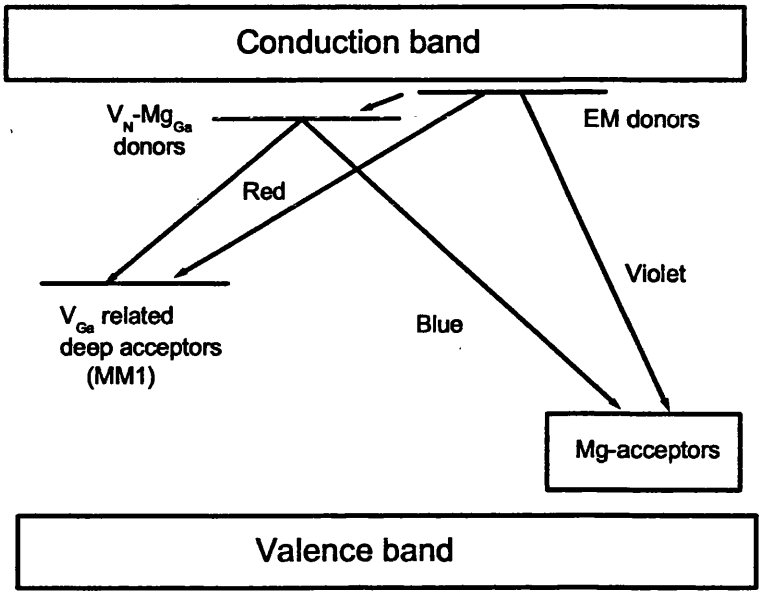

Figure 3.4: Schematic diagram for the recombination process giving rise to the red, blue and violet bands of GaN.

to be much smaller than the 250 meV proposed in the former reference (this is since, in our case, the emission involving both EM and the deeper donors leads to red emission). We note also that we take the MM1 center to be a deep acceptor, in agreement with the scheme shown in Fig. 5 of Ref. [51] (but in contrast to the assignment in Ref. [50]). The diagram is almost certainly oversimplified and should be viewed with caution, since donor and acceptor levels other than those shown are likely to be present. Further, there is strong evidence that the depth of the "shallow" acceptors (presumed to be formed by substitutional magnesium at gallium sites) is affected by Jahn-Teller effects and by the influence of strain and other nearby defects [85], so that it is represented in the diagram by a range of energy levels. As noted above, our results point to an electron "feeding" process from the EM to the deeper donors and it is interesting to note that such a process has previously been invoked to account for the temperature dependence of the red emission [50]. The dynamical behavior of this system of competing processes when magnetic resonance is stimulated in one of the levels is very complicated and requires a rate equation analysis which will be present in Chapter 6 .

Attempts have also been made to explain the PAS and PL/ODMR data by a single type of vacancy related defects, i.e., either V_{Ga} related or $V_N - Mg_{Ga}$. If V_{Ga} related centres are indeed the defects observed in the positron studies, to account for an increase in the number of V_{Ga} related centres at low levels of Mg doping, one would expect that the Fermi level moves towards conduction band at low Mg precursor flow rate. In other words, light Mg doping should increase *n*-type conductivity. This trend, however, was neither directly observed in our Hall measurements (sample #621 and #626 are both highly resistive in our measurements), nor reported by other workers. Furthermore, in our PAS measurements, the S parameter of the annealed sample #626A is just slightly smaller than that of the undoped sample #621. This minor decrease in S parameter is, however, not in scale with the difference of Fermi level positions between the two samples, since sample #626A shows clear *p*-type conductivity. Theoretical calculation suggests that the formation energy of V_{Ga} increases nearly linearly with Fermi level moving further towards valence band. We would therefore expect a much more dramatic drop of S parameter for #626A.

Another V_{Ga} related defect under consideration is a centre that V_{Ga} is associated with H in the undoped sample (and thus positrons cannot detect the complex). At low Mg precursor flow rate, as the induced Mg acceptor is more ready to associate with H, H is dissociated from V_{Ga} and the vacancy can then be detected by PAS. As the Mg flow rate is increased, the Mg ions will tend to occupy Ga sites and a reduction in vacancy concentration is expected, as observed. The main problem with this model is that, since H is the main contaminant in MOVPE grown samples, the amount of H ions should be enough for them to be associated with both V_{Ga} and Mg acceptors. Furthermore, in *n*-type GaN, V_{Ga} and associated complexes have been observed and studied extensively by PAS [63]. Therefore the V_{Ga}-H centre is unlikely to exist in the undoped sample. Additionally, there is very strong evidence from previous positron studies that $V_N - Mg_{Ga}$ is indeed formed in Mg-doped GaN. We therefore eliminate the possibility of the V_{Ga} centres as the only type of vacancy related defects.

The supposition that the positron data can be accounted for by $V_N - Mg_{Ga}$ alone is also problematic. Since the deep donor involved in the red band exists before and after annealing (reported in Chapter 5), the vanishing of the red PL

has to be associated with the elimination of the deep acceptor. The recombination process involving $V_N - Mg_{Ga}$ as an acceptor-like defect can be envisaged as $D^0 + [V_N^{3+} - Mg_{Ga}^- + e^-]^+ \longrightarrow D^+ + [V_N^{3+} - Mg_{Ga}^- + 2e^-]^0$. Here the complex can be regarded as a very deep double donor, which when it is in its singly ionised state contains one unpaired electron which leads to the ODMR signal with $g = 2.003$. The ODMR signal with $g = 1.962$ is associated with an unidentified relatively shallow donor. However, under most circumstances, except when the Fermi level is very close to the valence band, V_N will be in the 1+ state, and $V_N - Mg_{Ga}$ will be neutral. The transition level between 3+ and 1+-charge states of V_N occurs at 0.59 eV above the VBM [16] (0.16 eV [24] and 0.39 eV [86] in earlier calculations) and therefore, it is unlikely that the 3+ state of V_N exists in our as-grown samples. The formation energy of the $V_N - Mg_{Ga}$ centre is thus independent of the Fermi level and the increase in the concentration of the centre with Mg doping is expected. It is contrary to the gradual fall of the S parameter with Mg doping. We are thus forced to rule out a model in which all the data are accounted for by the presence of $V_N - Mg_{Ga}$ complexes.

3.5 Conclusions

Epitaxial GaN layers have been studied using PL, PAS and ODMR for the first time. We find that the change of the low momentum S parameter with Mg concentration and annealing is correlated with the behavior of the PL and ODMR signals in the red region, indicating that the red luminescence is vacancy-related. The experiments lead to the conclusion that the red emission is due to recombination between electrons from both EM and deeper donors with holes from deep acceptors and point to the deeper donors being $V_N - Mg_{Ga}$ and the deep acceptors V_{Ga} (or related complexes). To account for the rôle of the deeper donors (which in their neutral state are non-magnetic) in the ODMR process, a feeding process involving transfer of electrons from EM donors is found to be necessary, the ODMR signals from the $V_N - Mg_{Ga}$ being due to an ionized state in which an unpaired electron is present.

Chapter 4

ODMR of Mg-doped GaN in the green spectral region

4.1 Introduction

In this chapter we report the observation of an extraordinarily strong ODMR signal in unannealed GaN : Mg detected in the green region of the spectrum.

4.2 Experimental Details

The MOVPE grown Mg doped sample with the lowest Mg concentration (#626) is investigated. The sample is unannealed. The growth conditions and details of the sample can be found in Chapter 3. The ODMR measurements were carried out in 14 and 34 GHz systems which have been described in Chapter 2. Optical excitation of the ODMR was provided by a multi-line UV argon ion laser (dominant lines at 351.1 and 363.8 nm). The microwave excitation was chopped at low frequencies (typically ~600 Hz). For experiments with 100 GHz microwave excitation, a non-resonant cavity was used and the maximum power generated by the microwave source was ~ 35 mW. In order to record the wavelength de-

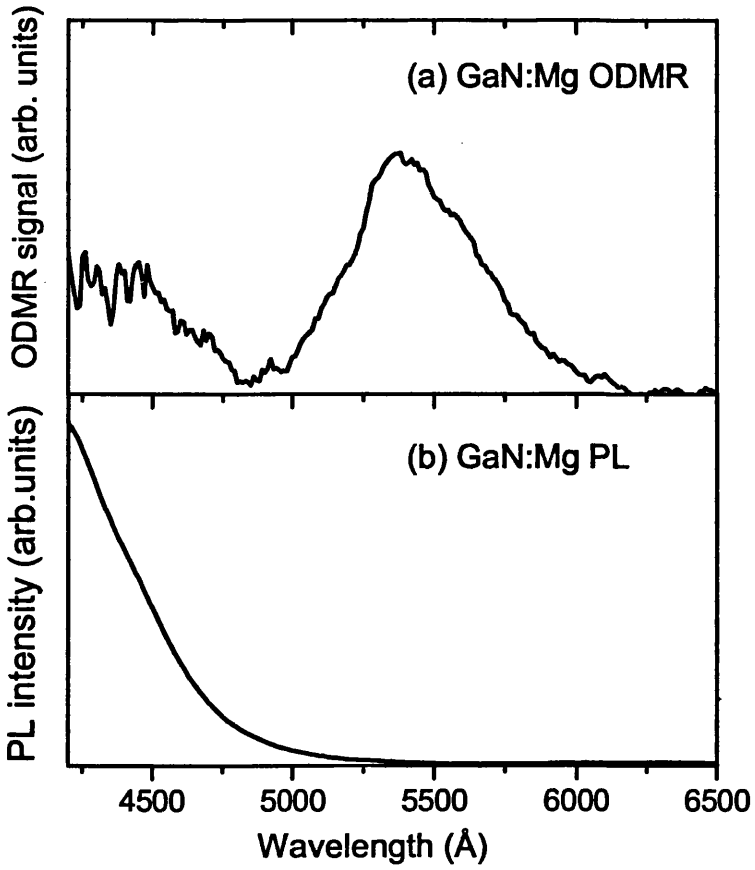

Figure 4.1: Wavelength-dependence of (a) the 13.75 GHz ODMR and (b) the PL signals of an as-grown GaN : Mg sample grown by MOVPE with a Mg precursor flow rate of 75 sccm (sample temperature 1.9 K; UV argon ion laser excitation).

pendence of the PL (in which case the UV excitation laser beam was chopped mechanically) or the ODMR signals, a single-grating spectrometer of 0.5 m focal length was used instead of the edge filters.

4.3 Experimental results

For the ODMR experiments, the PL was monitored in the wavelength range 500 to 550 nm (2.25 to 2.48 eV); the spectrum of the PL emission including the wavelength region relevant to ODMR is shown in Fig. 4.1(b). In Fig. 4.1(a),

we show the magnitude of the new ODMR signal as a function of wavelength (detected as the magnetic field set at the one of the ODMR signal positions with microwave excitation), indicating that it arises principally from a spectral region where the PL is relatively weak. However, it is shown in Fig. 4.1(a) that the same ODMR signal can also be detected within the wavelength range of the well-known donor-acceptor pair emission (400 to 450 nm) where the ODMR signal represents, however, a much smaller fractional modulation of the PL.

In Fig. 4.2 we show the 13.75 GHz ODMR spectra of the sample over a wide magnetic field range, from zero to 1 Tesla, as a function of the angle between the sample c-axis and the direction of magnetic field. The spectra are shifted vertically for clarity and the signals in each case are close to zero at the right hand side of the figure; for these spectra, the background signal detected away from microwave resonance conditions was relatively very small. A pronounced anisotropy of the signals was observed. Several extremely broad and intense bands are seen, at magnetic fields of 0.15, 0.46 and 0.86 Tesla at $B\|c$. Although quite clear shifts in position are observed, the width of the signals means that it is difficult unambiguously to extract details of the spin Hamiltonian from these measurements. We therefore recorded spectra with microwave excitation at 34 GHz and results are presented in Figs. 4.3 and 4.4; we shall also show that the data obtained with microwave excitation at 100 GHz provide additional confirmation of our model later.

The spectra are normalized to similar peak heights in order to emphasize their shifts in magnetic field, but we note that the strength of the signals increases dramatically as the sample is rotated with respect to the magnetic field. These bands are particularly strong for the sample with the lowest Mg concentration, but we do not observe such signals in samples grown in the same MOVPE system but without Mg doping. GaN : Mg samples supplied by other groups and grown either by MBE or MOVPE have also been investigated and are often found to show similar signals as well; the reasons for the dependence in strength of the signals on sample properties will be considered later in this chapter (4.6).

As can be seen in Fig. 4.3, the higher microwave frequency shows all the features already seen but allows a significantly better resolution. In particular, the peak

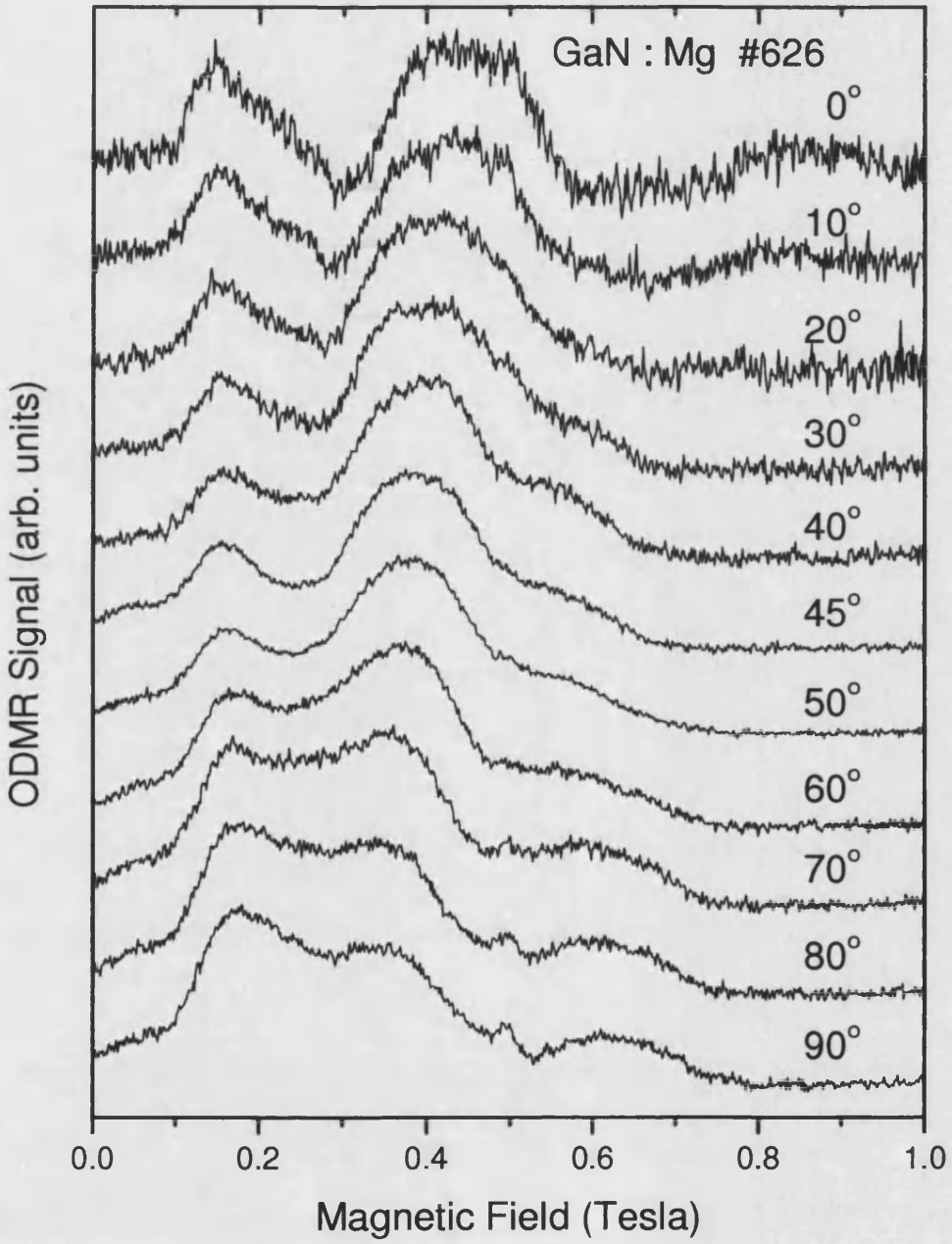

Figure 4.2: Angle-dependence of the ODMR spectra in the green spectral region of an as-grown GaN : Mg sample (Mg precursor flow rate 75 sccm). The microwave frequency was 13.75 GHz and the sample temperature was 1.9 K; the angles between the magnetic field and the normal to the sample are indicated on the figure. The spectra have been normalized to similar peak heights.

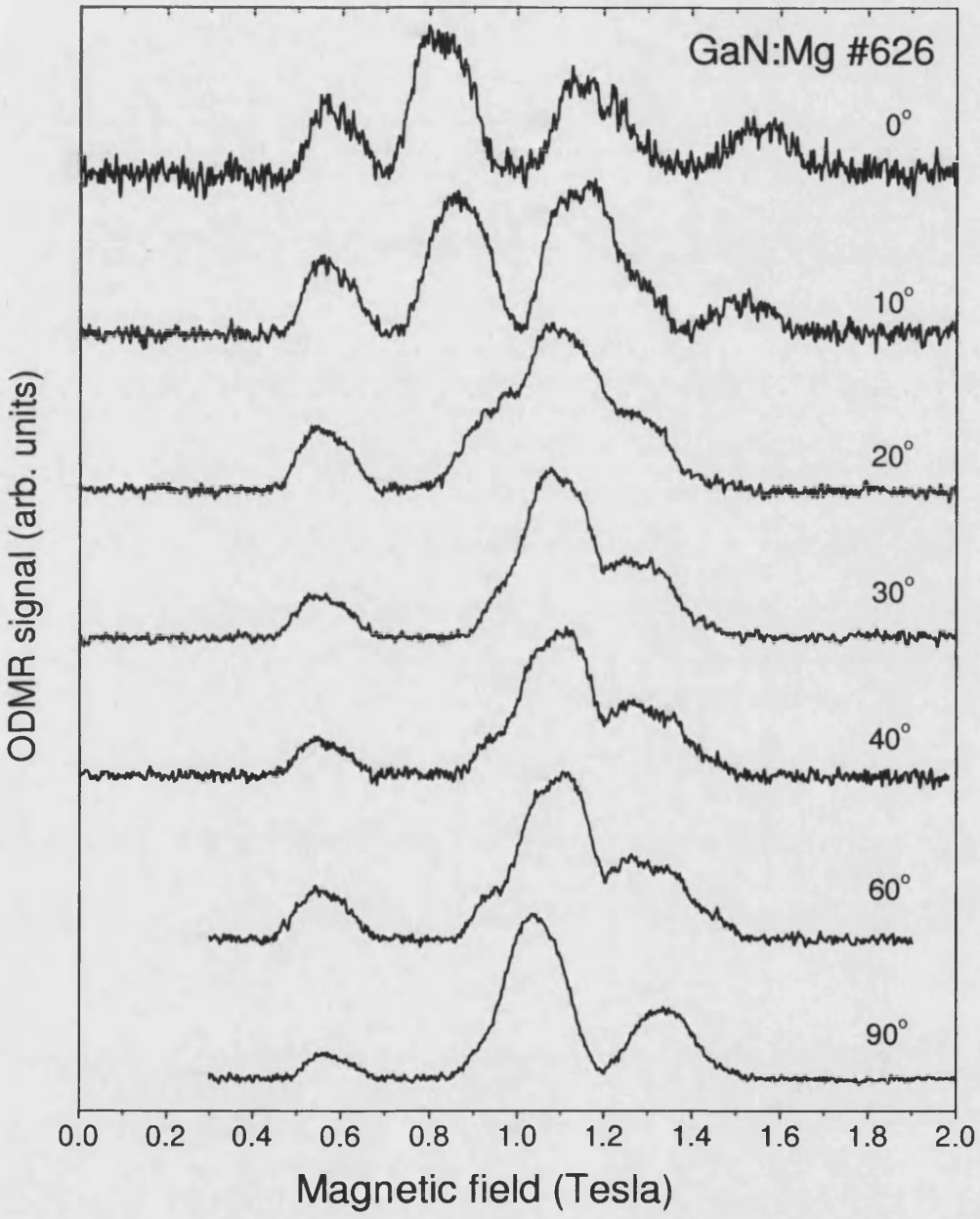

Figure 4.3: Angle-dependence of the ODMR spectra in the green spectral region of an as-grown GaN : Mg sample (Mg precursor flow rate 75 sccm). The microwave frequency was 33.57 GHz and the sample temperature was 1.9 K; the angles between the magnetic field and the normal to the sample are indicated on the figure. The spectra have been normalized to similar peak heights.

observed in the uppermost trace of Fig. 4.2 at about 0.15 Tesla is now clearly resolved into two components (at about 0.6 and 0.8 Tesla for the corresponding top trace of Fig. 4.3). A sharp signal is also observed at, for instance, 30° and 40° as a negative-going feature at 1.2 Tesla that coincides approximately with a dip between two broader, converging signals. It corresponds to a g-factor of 1.96 ± 0.001 and is assigned to the well-known shallow donor often observed in GaN : Mg [67]. The spectra are again normalized in order to display the variation of position with angle, but the improving signal-to-noise ratio from 0° to 90° indicates the rapid increase in intensity with angle.

4.4 Spin Hamiltonian model

The principal new features of the ODMR spectra presented above are four bands in the Faraday geometry, converging to three in the Voigt geometry (for example, the top and bottom traces of Figs. 4.2 and 4.3 respectively). Since the experimental conditions (detection wavelength range, Mg doping level and annealing state) under which these signals are observed are correlated, they arise from the same defect centre. The observation of four microwave-induced transitions between spin states requires at least four distinct spin states to be involved (though more states may in principle be involved if the selection rules for microwave absorption or any population effects prevent some transitions from being observed).

The simplest possibilities to be considered are therefore either a centre having $J = 3/2$ or an exchange-coupled pair of $S = 1/2$ centres $J = S \oplus S = 1/2 \oplus 1/2 = 0, 1$, with the requirement that the exchange coupling is close enough in magnitude to the microwave quantum energy that both $J = 0$ and $J = 1$ levels can contribute to the observed signals. We can rule out the former possibility, $J = 3/2$, because of the observation of the half-field line at around 0.58 Tesla in Fig. 4.4, which can only be associated with an overall integral spin.

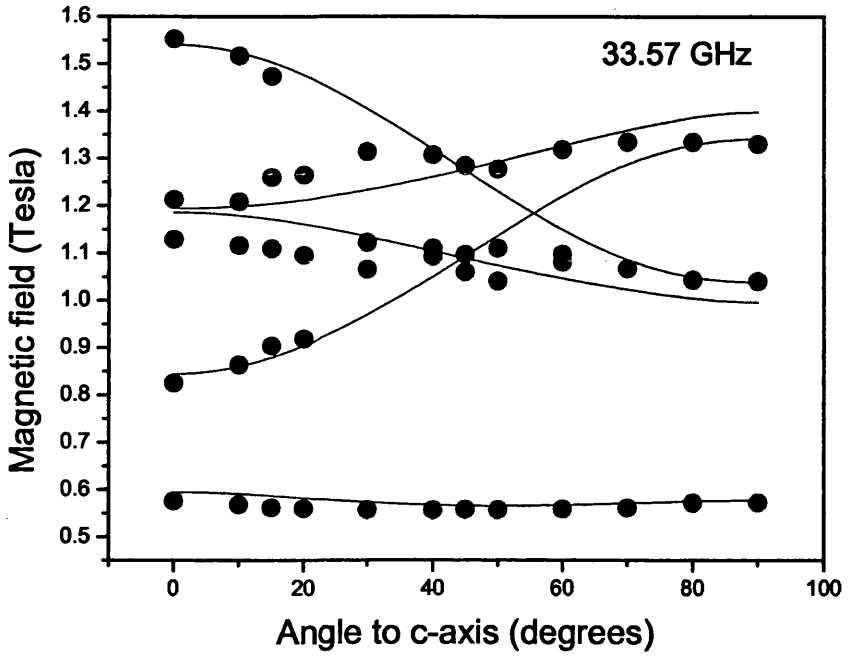

Figure 4.4: Summary of the peak positions of the 33.57 GHz ODMR spectra of Fig. 4.3 as a function of angle between the magnetic field and the sample normal (dots). Also shown are fits to the data on the basis of the model of two exchange-coupled $S = 1/2$ centres presented in the text (solid lines).

The general spin Hamiltonian appropriate to the second case is as follows [87],

$$H = \sum_{i=x,y,z} (g_{1i}\mu_B B_i \sigma_{1i} + g_{2i}\mu_B B_i \sigma_{2i} + A_i \sigma_{1i} \cdot \sigma_{2i}), \tag{4.1}$$

where $\sigma_{1,2}$ are the $S = 1/2$ spinors, the first two terms represent the Zeeman terms for the two $S = 1/2$ centres with anisotropic gyromagnetic ratios $g_{1,2}$ and a magnetic field $\mathbf{B}$ and, in the third term, A is the strength of the exchange interaction, allowed here to be anisotropic. Using this Hamiltonian, we are able to obtain a good description of the angle-dependence of the ODMR transitions, as shown by the solid lines in Fig. 4.4. However, there is some ambiguity in the determination of the parameters $g_{1,2i}$ and A_i and, in particular, in their relative signs. In order to understand this, it is useful to consider the solutions to the Hamiltonian of Equation 4.1. We define the angle θ to be the angle between the

magnetic field and the crystallographic c axis. The energy levels in the Faraday geometry ($\theta = 0$) are then given by Equation 4.2. In the Voigt geometry ($\theta = \pi/2$ and **B** defined to be along the x direction), a similar expression for the energy levels holds, with z and x interchanged (equation 4.3):

$$E(\theta = 0) = \begin{cases} -1/4\,A_z \pm 1/4\sqrt{(A_x + A_y)^2 + 4\mu_B^2(g_{1z} - g_{2z})^2B^2} \\ +1/4\,A_z \pm 1/4\sqrt{(A_x - A_y)^2 + 4\mu_B^2(g_{1z} + g_{2z})^2B^2}. \end{cases} \tag{4.2}$$

$$E(\theta = \pi/2) = \begin{cases} -1/4\,A_x \pm 1/4\sqrt{(A_z + A_y)^2 + 4\mu_B^2(g_{1x} - g_{2x})^2B^2} \\ +1/4\,A_x \pm 1/4\sqrt{(A_z - A_y)^2 + 4\mu_B^2(g_{1x} + g_{2x})^2B^2}. \end{cases} \tag{4.3}$$

We consider first the Faraday geometry. Equation 4.2 shows that, if $g_{1z} \simeq g_{2z}$ and $A_x \simeq A_y$, two of the four levels are dominated by the exchange effects and are only weakly dependent on field, whereas the other two levels will depend strongly on field, tending to energies of $\pm 1/2\mu_B|g_{1z} + g_{2z}|B$ at large fields. It will be seen in the following that the above conditions do indeed hold. The energy level structure of the exchange-coupled centre in the Faraday geometry is shown in Fig. 4.5. The ODMR transitions at microwave frequency ν =33.57 GHz are expected to occur at fields **B** given approximately by $h\nu = 2g_z\mu_B B$, $h\nu = g_z\mu_B B + A_z$ (A_z is assumed to be negtive here, as will be discussed below), $h\nu = g_z\mu_B B$ (two transitions), $h\nu = g_z\mu_B B - A_z$, as a sequence from low to high field; this corresponds to the distribution of signals shown in Fig. 4.4 for $\theta = 0$. From the magnetic field of the lowest ODMR transition (the "half-field line" at 0.58 Tesla), we can thus deduce that $|g_{1z} + g_{2z}| \sim 4.1$. The transitions at $h\nu = g_z\mu_B B \pm A_z$ allows us to estimate $|A_z| \sim 0.04$ meV. From the position of the $h\nu = g_z\mu_B B$ lines, we can obtain another estimate of the sum of the g-factors, $|g_{1z} + g_{2z}| \sim 4.08$. After careful fitting of the whole set of angle-dependent data, we find the g-factors and A terms are determined to accuracies of ± 0.02 and ± 0.002 respectively.

We now consider the Voigt geometry; a comparison of equations 4.2 and 4.3 reveals the most interesting feature of the present data. If we assume for the moment that all g-tensor components are close to +2 and that A_z and A_x have

Table 4.1: Spin Hamiltonian parameters used in the simulation of the data of Figs. 4.4 and 4.6 via Eq. 4.1.

Parameter	x	y	z
g_1	1.948	1.948	1.951
g_2	2.030	2.030	2.080
$g_1 + g_2$	3.978	3.978	4.031
A/meV	0.04	0.04	-0.04

the same magnitude and sign, then there is no strong dependence of the ODMR transitions on angle, since equations 4.2 and 4.3 become similar. However, this situation does not agree at all with the data of Fig. 4.4, where a strong angle-dependence is observed. We therefore consider next the case that A_z and (A_x, A_y) have opposite signs. A consequence of this would be that the first term of equation 4.3 has *neither* a strong Zeeman *nor* a strong exchange component and, thus, the two energy levels it represents become close to degenerate (the middle two levels at Voigt geometry in Fig. 4.5). The splitting between the other two energy levels depends on field (at large field) as $\mu_B|g_{1x} + g_{2x}|B = 2\mu_B g_x B$, leading to two ODMR transitions at **B** given approximately by $h\nu = g_x\mu_B B \pm A_x$ in addition to the half-field line at $h\nu = 2g_x\mu_B B$. This corresponds closely to the pattern of signals shown in Fig. 4.4.

It can be seen that, in the Faraday geometry, a crossing of the $(J, m_J) = (1, 1)$ and $(J, m_J) = (0, 0)$ levels is predicted at around 0.3 Tesla. This has however not yet been observed. The figure demonstrates that the magnitude of the exchange splitting for this centre is comparable to the size of the Zeeman splittings, in contrast to other coupled centres we have observed [88] where, due to a stronger coupling, the $(J, m_J) = (0, 0)$ level played no role in the ODMR spectra.

The above approximations in Faraday and Voigt geometries give a starting point for the simulation of the data; we find that the fit is not well constrained and that, because of the considerable width of the ODMR transitions, several sets of fitting parameters give equally good fits to the data. As an example, the set of parameters used in the simulation of the ODMR spectra in Fig. 4.4 is summarized in Table 4.1. We find that A_z and (A_x, A_y) not only have opposite signs, but that

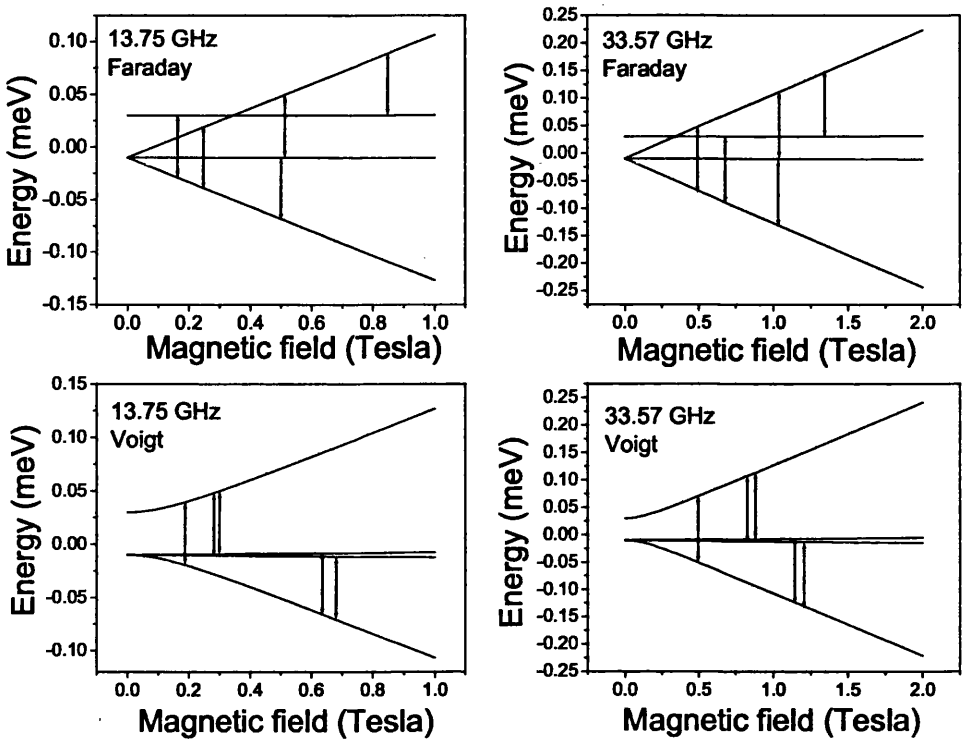

Figure 4.5: Energy levels on the basis of the model of two exchange-coupled $S = 1/2$ centres presented in the text. Magnetic field is applied along (Faraday) or perpendicular to (Voigt) the symmetry axis. The microwave transitions (small arrows) at 13.75 GHz (left) and 33.57 GHz (right) are also shown.

they have almost equal magnitudes (there is some interplay between the effects of the choice of g-values and A values). The relative signs of the parameters are also uncertain: good simulations of the data can be obtained if all A_i are, for instance, positive. The rules the signs must obey can be deduced from Eqs. 4.2 and 4.3 and are: if all A_i have the same sign, then either $g_{1x} < 0$; $g_{1z}, g_{2x}, g_{2z} > 0$ or $g_{2x} < 0$; $g_{1x}, g_{1z}, g_{2z} > 0$ whilst, if A_z is opposite in sign to $A_{x,y}$, then either $g_{1x}, g_{2x} < 0$; $g_{1z}, g_{2z} > 0$ or all g are positive. Since the data are described adequately in terms of two identical interacting spin 1/2 centres, it seems more logical to assume that A_z is opposite in sign to $A_{x,y}$, rather than invoking two different centres, one of which must have one negative g component.

A reasonably good fit can be obtained by directly applying the set of parameters in Table 4.1 to data obtained at microwave frequency ν =13.75 GHz (Fig. 4.4).

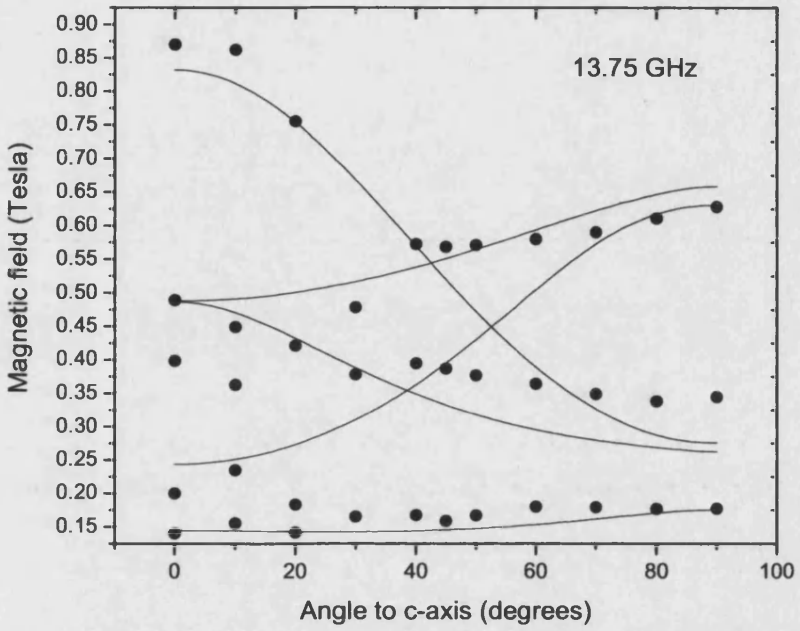

Figure 4.6: Summary of the peak positions of the 13.75 GHz ODMR spectra of Fig. 4.2 as a function of angle between the magnetic field and the sample normal (dots). Also shown are fits to the data on the basis of the model of two exchange-coupled $S = 1/2$ centres presented in the text (solid lines).

As shown in Fig. 4.5, in Faraday geometry, the transition of $h\nu = g_z \mu_B B + A_z$ happens at lower field than the "half-field transition" at 13.75 GHz; in Voigt geometry, similar situations hold for microwave frequencies of both 33.57 GHz and 13.75 GHz. The fitting at different microwave frequencies therefore gives further support to the exchange-coupled pair model we use.

At 100 GHz, since the sample was placed in a non-resonant cavity, it was possible to vary the microwave frequency continuously and thus ODMR signals could be obtained at a set of frequencies as shown in Fig. 4.7. The inset to this figure shows a typical spectrum; in this spectrum, a negative-going signal implies an overall enhancement of the PL intensity on application of the resonant microwave field. It is clear that the broad signals found at 35 GHz are again seen, though only three peaks are observed. The sharp, positive-going signal is due to the isolated shallow donor and the variation of its position in field with the microwave frequency is consistent with a g-factor of 1.951, indicated by the dashed line in

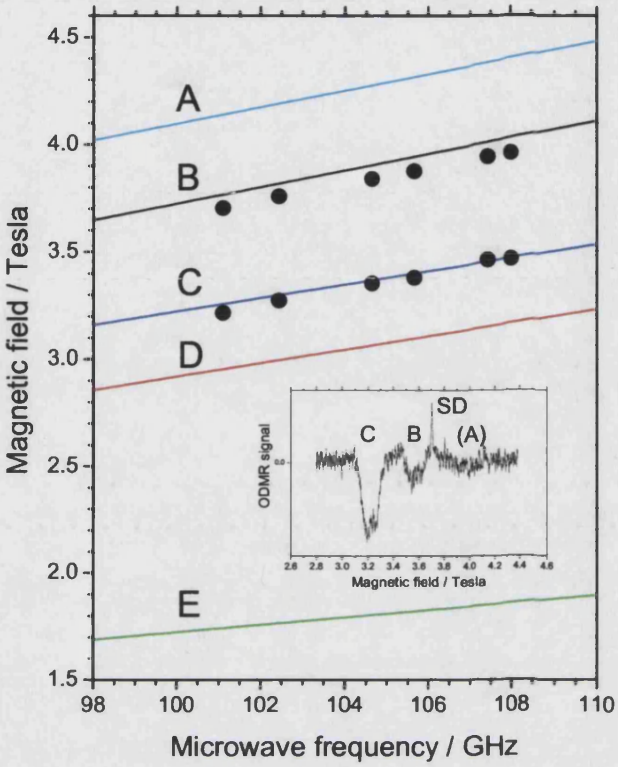

Figure 4.7: Summary of the peak positions of the 100 GHz ODMR spectra as a function of microwave frequency (dots). Also shown are calculated field positions of the transitions using the parameters in Table 4.1, on the basis of the model of two exchange-coupled $S = 1/2$ centres presented in the text (solid lines). The inset shows a typical spectrum.

Fig. 4.7. The remaining signals arise from the centre seen only in the green PL region and the solid lines show the calculated field positions of the transitions using the parameters obtained from the fitting of the 35 GHz data (Table 4.1).

4.5 Interpretation of the spectra

The g-values obtained from the fit correspond to those of shallow donors and shallow acceptors in GaN. The obvious choice for the shallow acceptor would be Mg, while several candidates exist for the shallow donor, such as Si_{Ga} [68], O_N [69] or $V_N - H$ complex [53]. It indicates that the microscopic origin of this luminescence is completely different from the yellow band observed in n-type

GaN. Similar ODMR signals from yellow emission were reported earlier for Mg doped GaN bulk crystals by Bayerl *et al* [89] and Godlewski *et al* [90]. The signals were explained by spin triplet resonance and tentatively attributed to the Mg-O complex. In Ref. [89], the g-values used for the fit ($g_{e||} = g_{e\perp} = 1.83, g_{h||} = 2.18, g_{h\perp} = 2.22$) are close to those obtained here, but the sign of the exchange interaction term (described by an axial fine-structure tensor) in [89] remains unchanged ($D_{||} = 0.18\text{cm}^{-1}, \text{D}_{\perp} = 0.09\text{cm}^{-1}$). It was shown in [89] that the exchange coefficient is strongly related to the overlap of the coordinate (orbit) wave function rather that arising from direct overlap of the electronic wave-function. The spin "feels" the local field by means of the spin-orbit coupling. The exchange term here is therefore decided by the interparticle distance, strain and crystal field, etc. The origin of the remarkable form of the exchange term in this investigation is still under study.

4.6 Isotropic signals in the green spectral region

A different kind of broad ODMR signal was detected in the green spectral region from samples of various growth techniques and doping profiles and are summarised in Fig. 4.8. Unlike the anisotropic signals discussed above, the signal positions here show no shift when the direction of the magnetic field is changed from being parallel to the sample c-axis to 45° to the c-axis, while part of the signals transfer from PL-quenching to PL-enhancing (Fig. 4.8 left). The intensity of the line is also highly anisotropic. The maximum amplitude is found with **B** oriented 40° away from the c axis. The signals exist in Mg doped samples grown by MBE as well as by MOVPE. Weak signals have also been detected in Si doped samples, but Mg may well be a common contaminant in the growth system. The signals become weaker after thermal annealing.

The first instinct would be to describe the signals by an exchange-coupled pair of $S = 1/2$ centres with isotropic g-factors and exchange interaction strength. The same spin Hamiltonian (Eq. 4.2) will apply, whereas in this case both g and A are numbers instead of tensors. However, a good fit of the fields of the

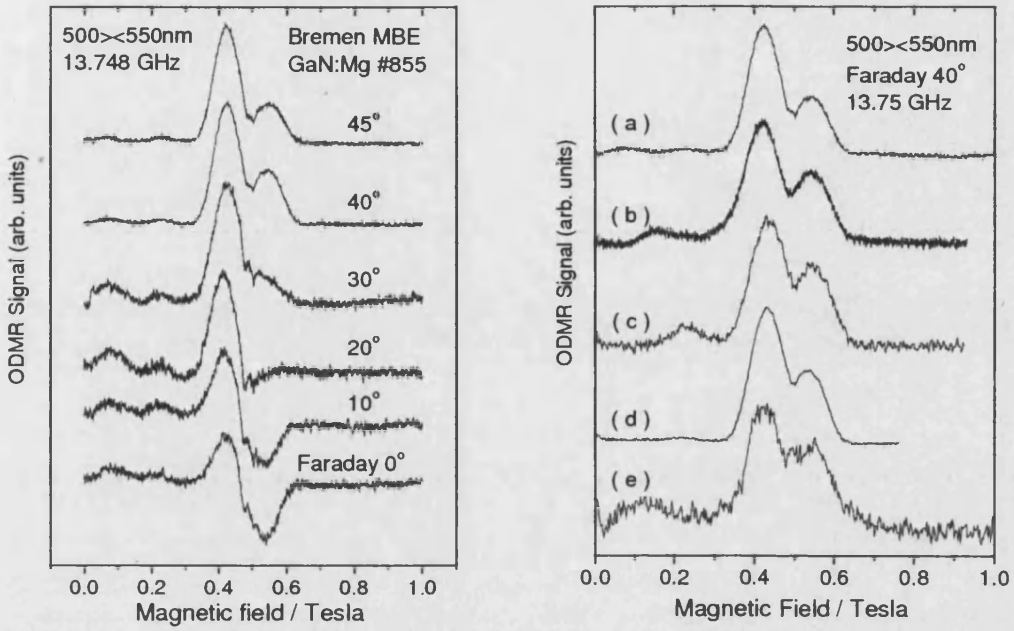

Figure 4.8: Left: Angle-dependence of the ODMR spectra in the green spectral region of an MBE grown GaN : Mg sample (# 0855). The microwave frequency was 13.748 GHz and the sample temperature was 1.9 K; the angles between the magnetic field and the normal to the sample are indicated on the figure. The spectra have been normalized to similar peak heights. Right: ODMR spectra in the green spectral region of samples of different origins: (a) MBE grown GaN : Mg sample (# 0855) from Bremen University; (b) MBE grown GaN : Mg sample (#738) from Sharp Laboratories of Europe Ltd.; (c) lightly Mg doped GaN grown by MOVPE after thermal annealing; (d) sample (c) before thermal annealing; (e) Si doped GaN grown by MOVPE. The microwave frequency was 13.75 GHz and the sample temperature was 1.9 K; all the spectra were obtained in Faraday 40° geometry and have been normalized to similar peak heights.

transitions could not been obtained. The difficulty here arises principally from the differences between the g-value attained from the "half-field line" and that from the $h\nu = g_z \mu_B B$ transition and, taking sample #0855 as an example, the $|g_1 + g_2|$ deduced are ~ 4.25 and ~ 4.64, respectively. It suggests that a different model may be required to accounted for the signals. Such broad g-isotropic signal with strong anisotropy of intensity was also reported by Glaser *et al* [91] on 24 GHz ODMR for MOVPE GaN : Mg and was attributed to an $S > 1/2$ defect. The origin of the signals requires further investigation.

4.7 Conclusions

ODMR on the green spectral region of lightly Mg-doped GaN film grown by MOVPE exhibits new resonance features. The spectra are dominated by several broad (FWHM = 110 - 140) lines. Angular rotation studies of this sample reveal that the g-value and intensity are pronouncedly anisotropic. The spectra are described by an exchange-coupled pair of $S = 1/2$ centres. Donor and acceptor g-values of $g_{ez} = 1.951$, $g_{ex} = g_{ey} = 1.948$, $g_{hz} = 2.08$ and $g_{hx} = g_{hy} = 2.03$ are found. The exchange interaction can be described by a tensor with $A_z = -0.04$ meV and $A_x = A_y = 0.04$ meV. This pair is tentatively assigned to a shallow donor-Mg complex. A different kind of broad ODMR signal with fairly isotropic g-values but highly anisotropic intensity has been detected from GaN samples of various origins. However, no direct correlation has been found between sample origins and the two types of ODMR signals.

Chapter 5

ODMR studies of concentration and annealing dependence on Mg-doped GaN

5.1 Introduction

Although the ODMR technique has been applied by several groups to study the recombination process of Mg doped GaN films as a function of Mg concentration, almost all the data reported are obtained after Mg acceptor activation [50, 67, 88, 91, 92]. In this chapter, we provide PL and ODMR studies of Mg doped GaN samples grown by MOVPE with four different Mg concentrations before and after annealing, expecting to achieve better understanding of the annealing and self-compensating mechanisms. Systematic and dramatic changes of ODMR spectra have been detected with increasing Mg concentration and with annealing, indicating that the method is an effective tool to probe this problem. It is observed that the annealing process has a similar effect to increasing Mg concentration in terms of eliminating several competing recombination pathways.

5.2 Experimental details

The details of the Mg doped GaN samples were provided in Chapter 3. The low-temperature PL system and spectra were also presented in Chapter 3. For the room-temperature PL measurements, a Renishaw UV microscope system with frequency doubled argon ion laser excitation (244 nm) was used and a high excitation density was therefore achieved. Large laser power density on the GaN samples raises the local temperature and increases the concentration of the free carriers. The ODMR measurements were carried out with microwave frequencies in the 14 and 34 GHz bands. Optical excitation of the ODMR was provided by a multi-line UV argon ion laser (dominant lines at 351.1 and 363.8 nm). Typical microwave chopping frequency was 605 Hz. A description of the ODMR systems can be found in Chapter 2.

5.3 Experimental results

5.3.1 PL

The room temperature PL spectra of the samples with different Mg concentrations before and after annealing are shown in Fig. 5.1, the periodic structure being due to interference effects. The spectra of Fig. 5.1 are not corrected for the spectral response of the measurement system, but the main effect of this correction is a displacement of position of the peak of less than 50 meV to lower energy for broad PL bands and, obviously, is negligible for sharp peaks. Compared with the PL spectra taken at 10.5 K (Fig. 3.1), at room temperature a new narrow band at approximately 3.42 eV was observed, which is clearest for the samples expected to have the lowest Mg concentrations (as-grown #626 and #625). This band is ascribed to free exciton recombination associated with the A valence band on the basis of temperature-dependent reflectivity measurements [93, 94]. The 3.15 eV and 2.8 eV PL bands at low-temperature shift to 3.25 eV and 2.96 eV at room-temperature, respectively. The blue shift of the two bands with increased temperature cannot be explained by the energy shift in accor-

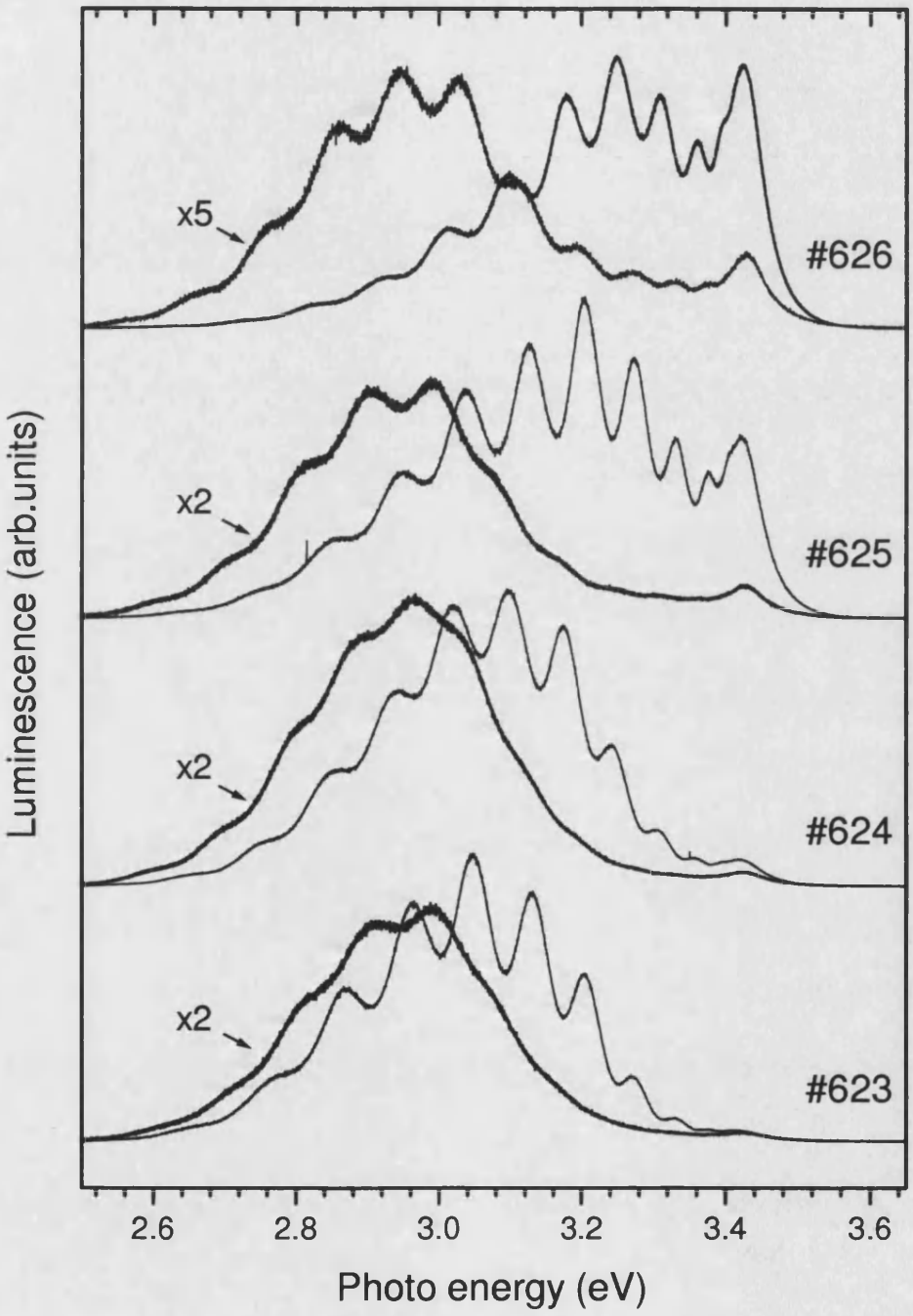

Figure 5.1: Room temperature PL spectra of the GaN : Mg samples grown with different Mg precursor flow rates increased from top to bottom before (thin line) and after (thick line) annealing.

dance with the band gap [95], since the band gap decreases when temperature is increased, nor by the effect of measurement system response. It is probably due to the increase of the excitation laser power from $\sim$ 0.3 $W\,cm^{-2}$ at low temperature to $\sim$ 10 $kW\,cm^{-2}$ at room temperature. This behaviour also supports the DAP recombination models suggested for the two bands in Chapter 3, that they are attributed to shallow donor-to-acceptor recombination and self-compensating donor-to-acceptor recombination, respectively. Similar to the low temperature spectra, when the Mg concentration is increased the 3.25 eV band at room-temperature disappears and the 2.96 eV band becomes dominant; annealing has a similar effect to increasing the Mg concentration. After annealing the 2.96 eV band dominates the spectra of the samples for all the four concentrations.

It is also observed from Fig. 5.1 that at room-temperature the PL intensity is reduced approximately by a factor of 5 for the lowest concentration sample (#626) and 2 for the other specimens after annealing. Such behaviour is however not a common rule. Annealing for some cases leads to increase of PL intensity but for the other cases to decrease or no change in intensity [88, 96, 97, 98].

5.3.2 Concentration and wavelength dependence: as-grown samples

Fig. 5.2, 5.5, 5.6, 5.7 demonstrate ODMR spectra obtained for as-grown samples with different Mg doping levels at different spectral windows here named as violet (2.75 - 3.1 eV), blue (2.48 - 2.75 eV), green (2.25 - 2.48 eV) and near-infrared (NIR, 1.13 - 1.46 eV). The windows were selected through the use of combinations of long- and short-pass filters in front of the detectors. The violet edge is specified as mentioned previously (Sec. 2.3) by the necessity of blocking the laser scattering light. The infrared edge is specified by the falling edge of the sensitivity of the Si APD. For as-grown samples, dramatically different ODMR spectra were obtained for a sample of a certain Mg concentration from different detection windows as well as from a certain window with increase of the Mg concentration. It indicates that different recombination models should be used to interpret various PL bands in the GaN samples and the mechanisms change with Mg concentration.

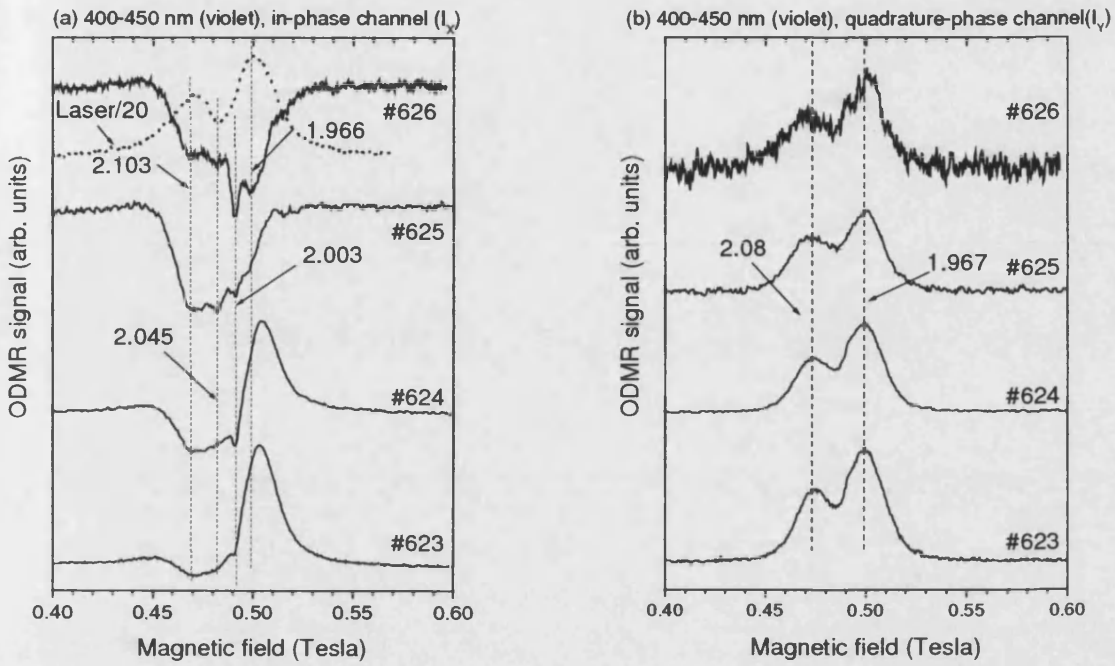

Figure 5.2: ODMR spectra at 13.76 GHz obtained from the PSD in-phase (I_X, a) and quadrature-phase (I_Y, b) channels on the violet (2.75 - 3.1 eV) spectral region for samples #626, #625, #624 and #623, with different Mg concentrations increasing from #626 to #623. The arrows indicate the g-values at $\mathbf{B}||c$ obtained using a Lorentzian multipeak fitting procedure and corresponded to the resonances indicated by the vertical lines.

5.3.2.1 Violet(2.75 - 3.1 eV)

The phase sensitive detector (PSD) that we used in our ODMR measurements extracts the Fourier coefficient of the sinusoidal wave in-phase (I_X) and quadrature-phase (I_Y) with the microwave excitation. The overall ODMR signals can be expressed as $I(\omega) = I_X \sin\omega t + I_Y \cos\omega t$, where ω is the microwave chopping frequency and I_X and I_Y are experimental measurables. For samples #626 and #625, the spectra obtained from I_X are dominated by four PL-quenching ODMR signals near the $g = 2$ region (Fig. 5.2. In these and all the following spectra, a positive-going signal implies an overall enhancement of the PL intensity on application of the resonant microwave field). The peak positions can be obtained by fitting the spectra with Lorentzian shape lines and the g-value of each signal can thus be worked out through the equation $h\nu = \mu_B g B$. The dependence of the spectra of sample #626 on the angle between the sample c-axis and the magnetic

field is shown in Fig. 5.3. All the four signals can be fitted by an effective spin of 1/2 using the simple equation $g(\theta) = \sqrt{g_{\|}^2 \cos^2\theta + g_{\perp}^2 \sin^2\theta}$:

(i) anisotropic signal with $g_{\|} = 2.103 \pm 0.003$ and $g_{\perp} = 1.98 \pm 0.01$ (FWHM = 12 mT), attributed to shallow Mg acceptor [67]. The linewidth at $\mathbf{B}\|c$ is the same as that obtained from the 9.5 GHz EPR measurement ($\sim$ 12 mT) in Ref. [67], but it is approximately two times smaller than that obtained from 24 GHz ODMR measurement in the same work ($\sim$ 27 mT).

(ii) anisotropic signal with $g_{\|} = 2.045 \pm 0.005$ and $g_{\perp} = 2.040 \pm 0.005$ (FWHM = 14 mT). It is similar to the signals tentatively attributed to Mg-related or induced deep centers or severely perturbed shallow Mg-acceptors [52, 67, 90, 99]. It is possible that the anisotropy of the signal is averaged out due to random lattice distortions and therefore, the properties of the acceptors will not reflect the symmetry of the uppermost valence band.

(iii) isotropic signal with $g_{\|}, g_{\perp} = 2.003 \pm 0.003$ (FWHM = 5 mT). The g-value and linewidth are very close to the deep level centre MM1 (g = 2.001, FWHM = 4 - 5 mT [51, 52]). According to Ref. [51] the MM1 signal is exclusively detected from the red luminescence band, but in this study the MM1 signal is observed from the violet and the blue regions as a PL-quenching signal, as well as from the red region as a PL-enhancing one (Fig. 5.2, 5.5, 3.2), indicating that the role of the defect centre involved in the recombination process changes. In Chapter 3 the chemical origin of this signal has been comprehensively discussed and it is attributed to Ga vacancies or related complexes.

(iv) anisotropic signal with $g_{\|} = 1.966 \pm 0.005$ and $g_{\perp} = 1.956 \pm 0.005$ (FWHM = 15 mT), assigned to a deep donor in this work.

The quenching nature of the four magnetic resonance signals indicates that they are from levels that are involved in recombination processes that are in competition with the PL being monitored and, therefore, appear as decreases in the emitted intensity. These competitive recombination processes should probably have longer recombination lifetimes than the direct monitored processes, i.e., the 2.8 eV PL band and the tail of the 3.15 eV PL band, since the two bands dominate

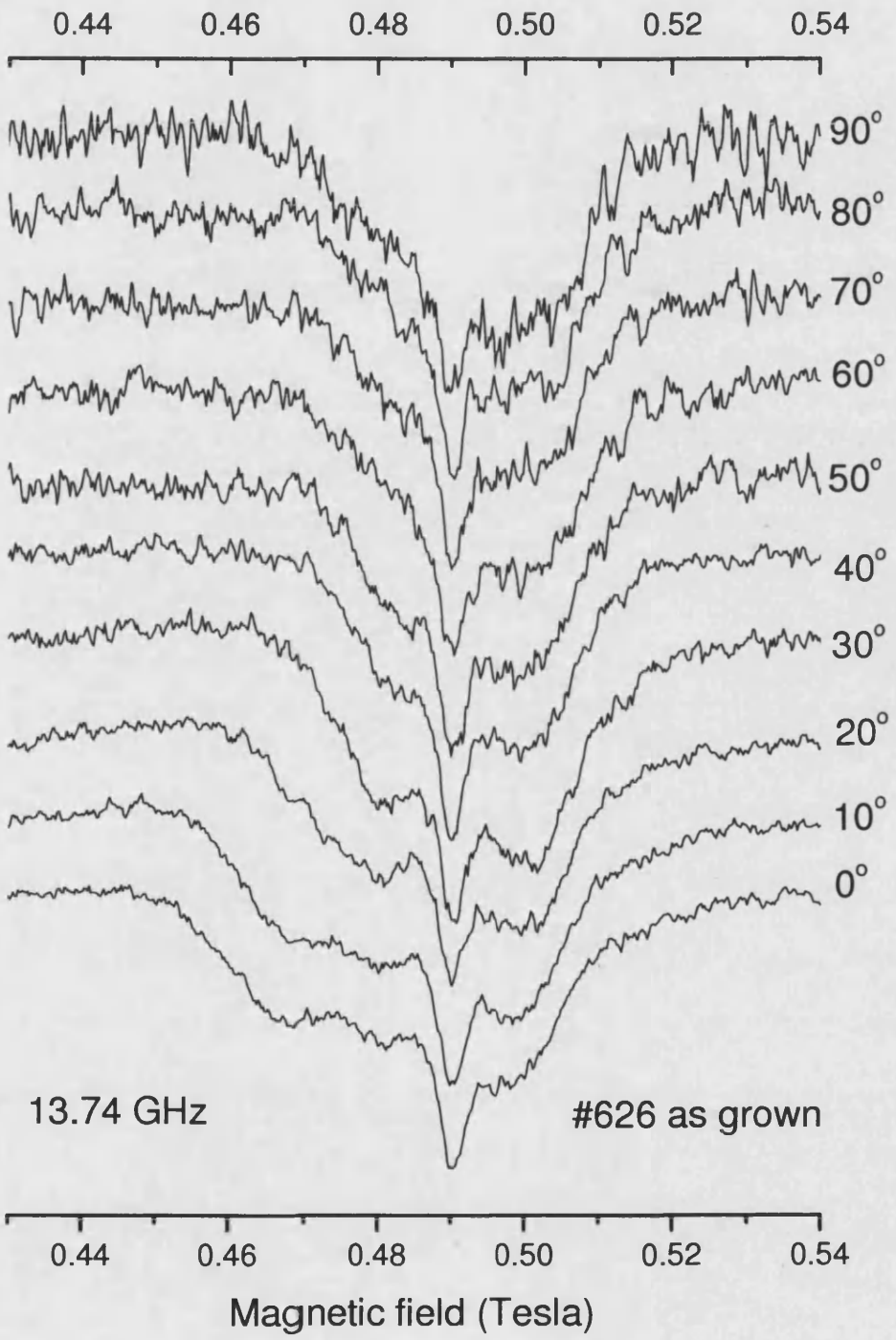

Figure 5.3: ODMR spectra at 13.74 GHz obtained from the violet spectral region for as-grown sample #626 as a function of the angle between the c-axis and the direction of the magnetic field.

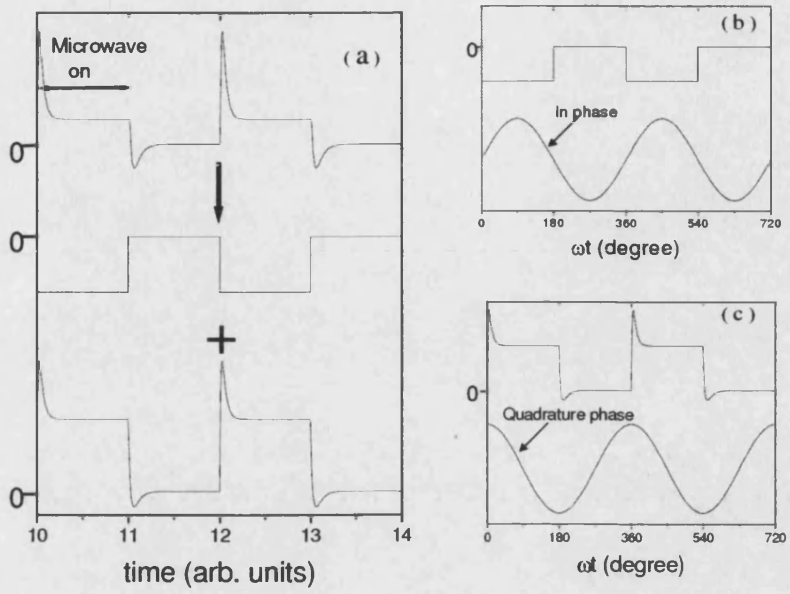

Figure 5.4: Schematic diagrams illustrating that the recorded waveform contains information on both PL-quenching and PL-enhancing signals, which can be separated into I_X and I_Y by choosing a suitable microwave chopping frequency or phase of the PSD.

the PL spectra and to give strong radiative emission the transition possibilities between the defect levels should be high. The waveform of the PL intensity as a function of time under resonance condition with microwave excitation switched on and off can be recorded by an averaging oscilloscope. If we imagine that in the situation that two magnetic resonance signals are partly overlapped, when the magnetic field is set at the peak of one signal, the recorded waveform probably contains information on both signals. As illustrated schematically in Fig. 5.4a, the recorded waveform in the present study contains information on both PL-quenching and PL-enhancing signals, and it can be further regarded as the sum of the quenching waveform and the enhancing waveform. At a relatively low microwave chopping frequency, the enhancing waveform, related to a shorter recombination lifetime, contributes mainly to the transient part of the recorded waveform and the quenching one to the plateau. The recorded waveform is, at the same time, the input of the PSD. At low chopping frequencies, I_X is not particularly sensitive to the transients part of the waveform, which occur close to the zero-crossings of the reference sine wave. I_Y, on the other hand, should be sensitive to the transient of the waveform (illustrated in Fig. 5.4b, c). We

can therefore separate the PL-quenching and PL-enhancing signals by choosing a suitable microwave chopping frequency or phase of the PSD. In the present study with a microwave chopping frequency of 605 Hz and phase of 0°, the two types of signals can be relatively well separated into I_X and I_Y. Two PL-enhancing signals are obtained from I_Y:

(v) anisotropic signal with $g_{||} = 2.08 \pm 0.01$ and $g_{\perp} \approx 2.0$ (FWHM = 13 - 18 mT). It is similar to the Mg-related signal reported by several groups [59, 67, 88, 91, 92, 100, 101, 102]. It is also suggested that the g-values of the Mg acceptors vary with different Mg concentrations in the range of $g_{||}$ from 2.102 to 2.065 and $g_{\perp}$ from 1.94 to 2.00 [92]. Such deviation of the Mg-acceptor g-values are also observed in this work with different Mg concentrations and with different detection windows (see Sec. 5.3.3) and it is comprehensively discussed in Ref. [85].

(vi) $g_{||}, g_{\perp} = 1.967 \pm 0.005$ (FWHM = 21 mT) is similar to a signal attributed to deep donors in this work,

In Chapter 6, calculations based on a rate-equation model suggest that the intensity of the quenching signal is proportional to the laser excitation power. This correlation is observed here, as it is shown on Fig. 5.2 (dotted line), when the laser power is reduced from approximately 10 Wcm^{-2} to 0.5 Wcm^{-2} the PL-quenching signals are replaced by the two PL-enhancing signals very similar to signals (v) and (vi) with $g_{||} = 2.086$ (FWHM = 30mT) and $g_{||} = 1.961$ (FWHM = 24 mT), respectively.

The I_X signal for sample #625 exhibits similar PL-quenching features in the violet region to sample #626, with some redistribution of the relative intensities of the signals that make up the spectrum. The acceptor-like signals become relatively stronger. The spectra from the violet region of samples #624 and #623 become complicated. This is because the quenching signals become weaker. The situation is further complicated when detecting in this region because the detection window cover different PL bands, some of which are enhanced and others quenched by the magnetic resonance. These spectra are similar to those obtained in Ref. [88] for an as-grown sample with similar Mg concentration at the microwave chopping

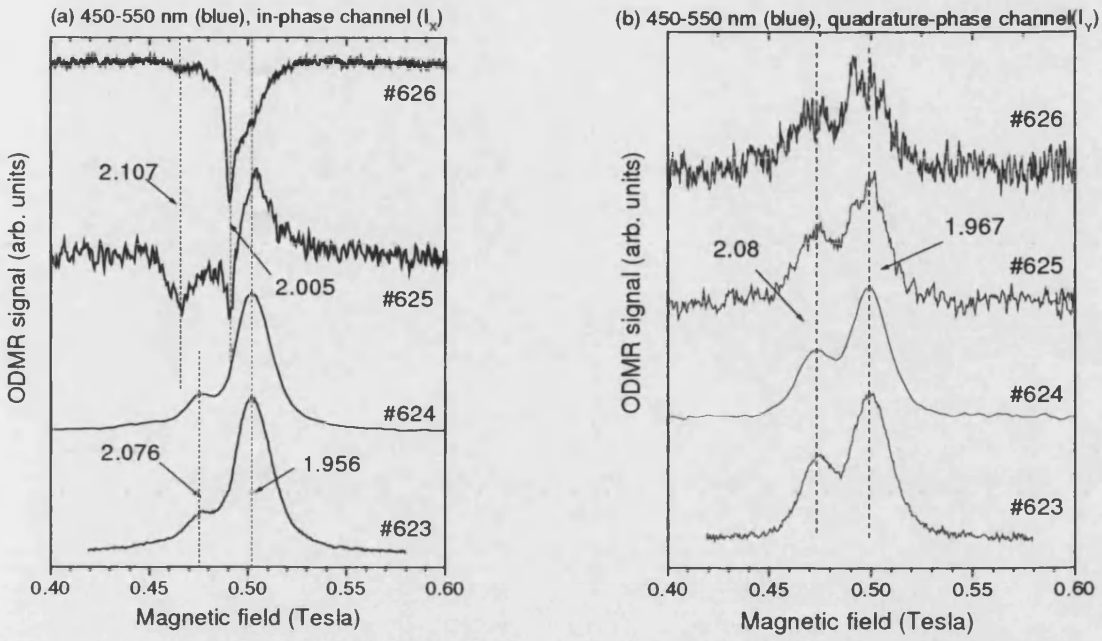

Figure 5.5: ODMR spectra at 13.76 GHz obtained from the PSD in-phase (I_X, a) and quadrature-phase (I_Y, b) channels on the blue (2.48 - 2.75 eV) spectral region for samples #626, #625, #624 and #623 with different Mg concentrations increasing from #626 to #623. The arrows indicate the g-values at $\mathbf{B}||c$ obtained using a Lorentzian multipeak fitting procedure and corresponded to the resonances indicated by the vertical lines.

frequency of 605 Hz. One possible explanation of the decrease of the quenching signals is that there is a decrease in the concentration of one or more of the defect centers giving the quenching signals (especially one of the donors (vi) and the MM1 center). This could be a result of the incorporation of the Mg dopant or a change of the Fermi level with Mg doping. The intensities of the Mg acceptor signal (v) and of the deep donor signal (vi) detected from the I_Y channel both increases, while exhibiting no change in their g-values when the Mg concentration is increased.

5.3.2.2 Blue (2.48 - 2.75 eV)

For sample #626 in the blue region (Fig. 5.5) signals (i) and (iv) become much weaker and signal (ii) disappears. The spectrum of sample #625 becomes com-

plicated, involving a PL-enhancing signal ($g_{||} = 1.956 \pm 0.001$, FWHM = 20 mT) (vii) assigned to the well-known shallow donor often observed in GaN : Mg [67]. Due to the unresolved signal (vi), the linewidth of signal (vii) is larger than it should be for the shallow donor signal (also reported in Sec. 5.3.2.6). Samples #624 and #623 demonstrate only two PL-enhancing signals (v) and (vii) discussed above. The ratio of the integrated intensities of these signals is $I_D/I_A \sim 10 - 11$, where I_A and I_D correspond to the intensities of signals (v) and (vii), respectively. The spectra from I_Y are very similar to those obtained in the violet spectral window: PL-enhancing signals (v) and (vi) are detected and the intensity of the signals increases with Mg-doping. The shallow donor signal in the present study is detected exclusively from I_X, indicating that the signal has a different dynamic behaviour from signal (vi).

It can be concluded at this point that signals directly involved in the emission detected from the violet and blue windows are deep donors (vi) and Mg acceptors (v).

5.3.2.3 Green (2.25 - 2.48 eV)

Broad ODMR spectra were observed from the green spectral region with three asymmetric signals (viii), each with FWHM = 110 - 140 mT peaked at 0.15 T, 0.46 T and 0.86 T at $B||c$, respectively (Fig. 5.6). Weak traces of the PL-quenching signals around g of 2 region are still observable for sample #626 and #625. For samples #624 and #623, the sharp shallow-donor signal (vii) at 0.50 Tesla, appearing as a positive-going signal still remains. Wavelength, angular, and microwave frequency dependencies of the spectra have been comprehensively investigated in Chapter 4 and the spin Hamiltonian has been determined. Possible microscopic models have also been discussed. Increasing Mg-concentration leads to the decrease of the intensity of the broad signals, shown as a decrease of the signal-to-noise ration for sample #624 and #623.

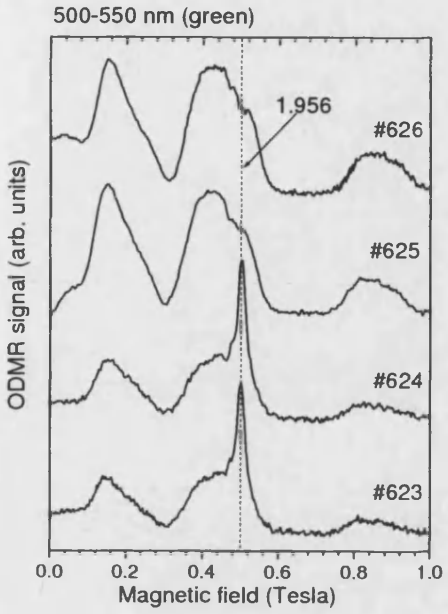

Figure 5.6: ODMR spectra at 13.76 GHz obtained from the green (2.25 - 2.48 eV) spectral region for samples #626, #625, #624 and #623 with different Mg concentrations increasing from #626 to #623. The arrows indicate the g-values at $\mathbf{B}||c$ obtained using a Lorentzian multipeak fitting procedure and corresponded to the resonances indicated by the vertical lines.

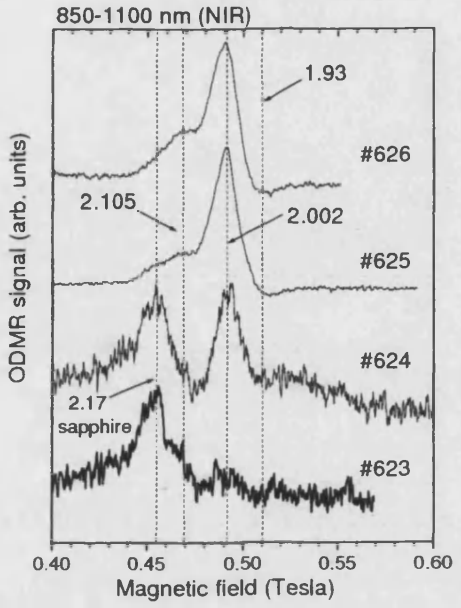

Figure 5.7: ODMR spectra at 13.76 GHz obtained from the NIR (1.77 - 1.91 eV) spectral region for samples #626, #625, #624 and #623 with different Mg concentrations increasing from #626 to #623. The arrows indicate the g-values at $\mathbf{B}||c$ obtained using a Lorentzian multipeak fitting procedure and corresponded to the resonances indicated by the vertical lines.

5.3.2.4 Red (1.77 - 1.91 eV)

The origin of the red emission has been extensively discussed in Chapter 3. The ODMR spectra of the as-grown samples have been reported in Fig. 3.1. Signal (iii) that is PL-quenching in the violet and blue regions becomes PL-enhancing in the red region, while signals (i) and (ii) remain PL-quenching. Furthermore, the asymmetric PL-quenching feature for sample #626 and #625, which comes from the overlap of signals (i) and (ii), becomes more symmetric for sample #624 and #623 with $g_{||} = 2.073$. At the high field side of signal (iii) the other two overlapping luminescence-enhancing resonances are observed, which are both attributed to donors and are better resolved in the measurements performed at 34 GHz (reported in Sec. 5.3.2.6). The red PL becomes weaker when the Mg

concentration is increased (Fig. 3.1). The ODMR signals also decrease, exhibited as a reduction of the signal-to-noise ratio.

5.3.2.5 Near-infrared (NIR) (1.13 - 1.46 eV)

The NIR ODMR spectra for the as-grown samples are shown in Fig. 5.7. The $g_{||} = 2.105$ (i) and $g_{||} = 2.045$ (ii) signals now become PL-enhancing for samples #626 and #625. Additionally there appear two new signals:

(ix) PL-quenching signal with $g_{||} = 1.94 \pm 0.01$ and FWHM = 15-25 mT from sample #626 ($g_{||} = 1.93 \pm 0.01$ and FWHM = 20-25 mT from sample #625). The g-values are similar to those reported from InGaN/GaN LED structures ($g_{||} = 1.926, 1.934, 1.940$) [103] and attributed to shallow donor or conductive electron g-values.

(x) isotropic signal with $g_{||}, g_{\perp} = 2.005$ (FWHM = 16 - 17 mT). It is similar to the MM2 deep defect centre ($g = 2.006$, 18 - 32 mT) detected from the PL <1.9 eV [51].

The NIR PL band is therefore a transition from deep defects (MM2) to Mg acceptors. It competes with shallow donors (or conduction band electrons) involved transitions.

In the NIR region sample #623 with the highest Mg concentration demonstrates no GaN : Mg related ODMR signals. Instead two previously unreported signals from the sapphire substrate are observed:

(xi) isotropic signal with $g_{||}, g_{\perp} = 2.17 \pm 0.005$ (FWHM = 20-23 mT), PL-enhancing.

(xii) isotropic signal with $g_{||}, g_{\perp} = 2.131 \pm 0.003$ (FWHM = 4 mT), PL-quenching.

Neither of the two signals is related to the Cr^{3+} line at 6934 Å since the signal is much stronger from the NIR region than from the red region. Previous study shows that the g-values for the Cr^{3+} line are $g_{||} = (-)2.445 \pm 0.001$ and $|g_{\perp}| < 0.06$ [104].

The signals (xi) and (xii) are also detected from sample #625 and #624. Sample #626 with the lowest Mg-concentration demonstrates strong ODMR signals from the GaN : Mg layer in the NIR region, therefore the signals from the sapphire substrate are negligible. The origins of the signals from sapphire substrate are still unclear.

5.3.2.6 34 GHz

The ODMR results obtained by using the 34 GHz microwave system for sample #626 from the red and the violet regions are shown in Fig. 5.8. With improved spectral resolution, the shallow donor signal (vii) with $g_{||} = 1.952 \pm 0.003$ and FWHM = 8-10 mT is resolved in both regions. From the red region, the deep donor signal (vi) ($g_{||} = 1.967 \pm 0.005$, FWHM = 33 mT) is also resolved. At 34 GHz the linewidth of signal (vi) is ~ 1.5 times larger than it is at 14 GHz. From the violet region, signal (i) also reveals roughly two times larger linewidth at 34 GHz ($g_{||} = 2.087 \pm 0.005$, FWHM = 37 mT). It is well known that a resonance signal broadens proportionally to the increase of microwave frequency, if the following two conditions are met: (i) its width is mainly due to inhomogeneous broadening; (ii) the inhomogeneous broadening arises from variation in g-values, and hence the centres are sensitive to strain. It is therefore suggested that both signal (i) and (vi) are inhomogeneously broadened.

With improved resolution, at 34 GHz two additional PL-quenching signals existing as shoulders of the MM1 signal are resolved. By fitting the violet spectrum with Lorentzian shape lines, their g-values are obtained:

(xiii) $g_{||} = 2.017 \pm 0.005$ (FWHM = 16 mT), similar to the signal assigned to Mg-related deep defect ($g_{||} = 2.02 \pm 0.005, g_{\perp} = 2.00 \pm 0.005$, FWHM = 35

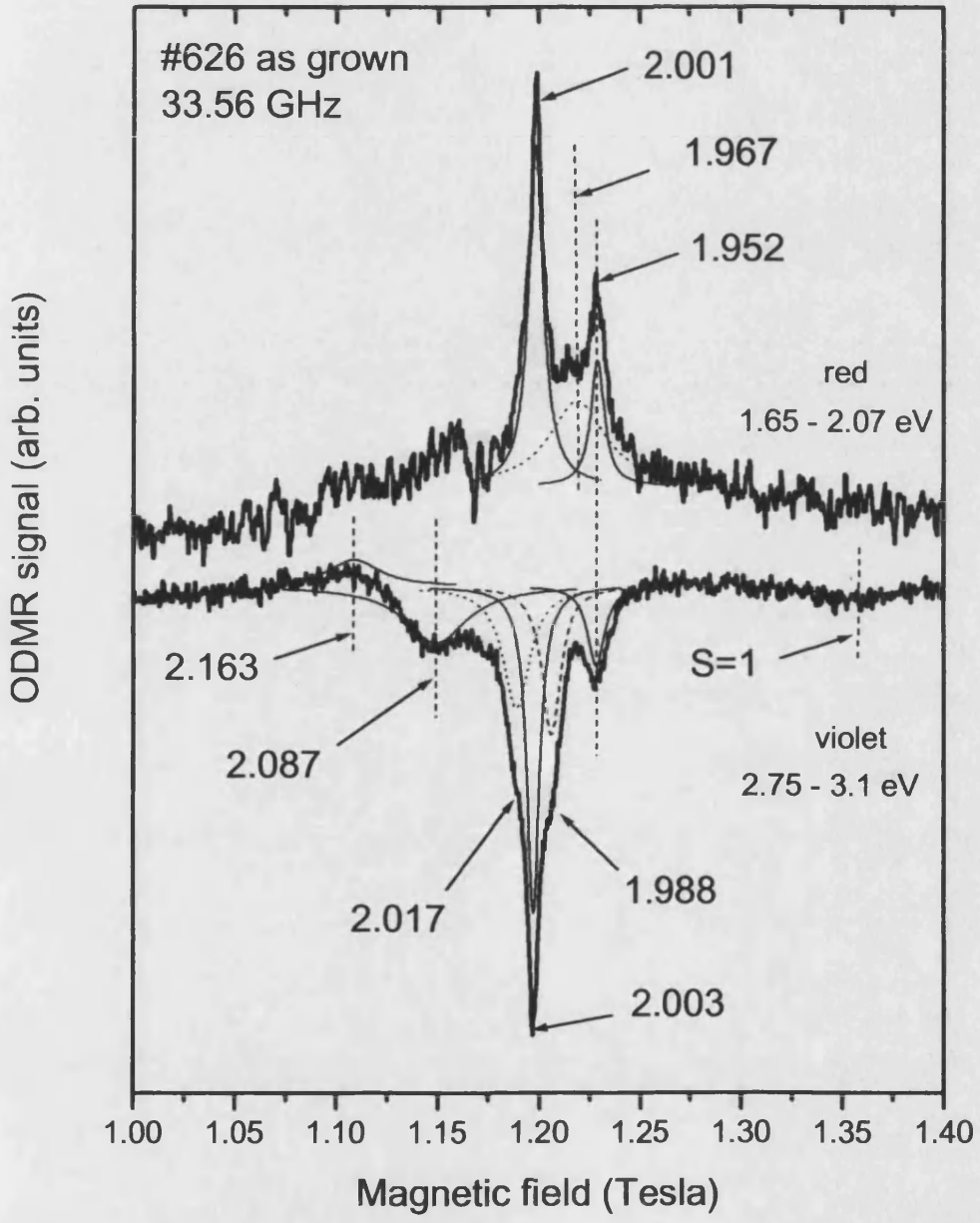

Figure 5.8: ODMR spectra at 33.56 GHz detected on the violet (2.75 - 3.1 eV) and red (1.65 - 2.07 eV) spectral regions for as-grown sample #626, $\mathbf{B}\|c$. The arrows indicate g-values. The spectra were decomposed by Lorentzian shape lines shown as thin and broken lines.

Table 5.1: Summary of the g-values observed in Mg-doped GaN in this work: as-grown samples. The signals indicated by * are observed for the first time in the present work.

Index		Assignment	$g\|\|$	$g_\perp$	FWHM, mT
1	(i)	Mg acceptor	2.107	~ 1.98	12
2	(ii)	Mg-related deep centre	2.045	2.040	14
3	(iii)	Deep acceptor (MM1)	2.003		5
4	(iv)	Deep donor	1.966	1.956	15
5	(v)	Mg acceptor	2.08	~ 2.0	13-18
6	(vi)	Deep donor	1.967		21
7	(vii)	Shallow donor	1.956		8-10
8	(viii)*	paired defect	S=1/2 $\otimes$ 1/2		110-140
9	(ix)*	Shallow donor or CB electron,	1.94		15-25
10	(x)	Deep donor (MM2)	2.005		16-17
11	(xi)*	From sapphire	2.17		20-23
12	(xii)*	From sapphire	2.131		4
13	(xiii)	Mg-related deep defect	2.017		16
14	(xiv)	Deep donor	1.988		11

mT) reported in Ref. [105] and a deep defect ($g = 2.016$) for MBE grown undoped GaN [106].

(xiv) $g_{||} = 1.988 \pm 0.005$ (FWHM = 11 mT), similar to the deep donor related signal ($g_{||} = 1.989 \pm 0.001, g_\perp = 1.992 \pm 0.001$, FWHM = 13 mT) from MOCVD grown undoped GaN [91] and a deep donor signal (g=1.985, FWHM = 14 mT) for MBE grown undoped GaN [106].

The ODMR signals observed in this work for the as-grown samples are summarized in Table 5.1.

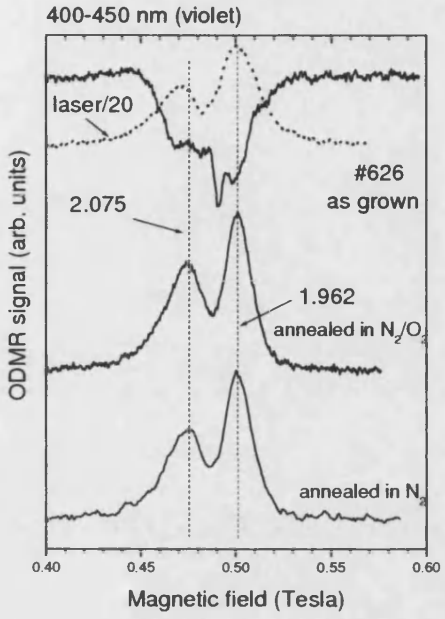

Figure 5.9: ODMR spectra at 13.76 GHz detected on the violet (2.75 - 3.1 eV) region for sample #626 before and after annealing. The arrows indicate g-values with $\mathbf{B}\|c$.

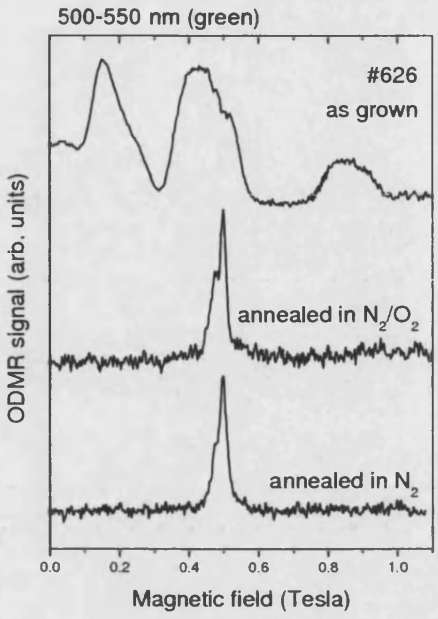

Figure 5.10: ODMR spectra at 13.76 GHz detected on the green (2.25 - 2.48 eV) region for sample #626 before and after annealing.

5.3.3 Concentration and wavelength dependence: annealed samples

After annealing the samples at 850°C in nitrogen atmosphere with (a) and without (b) 0.5% of oxygen, dramatically different ODMR spectra were obtained compared with those of the as-grown samples. Most of the PL-quenching ODMR signals from the violet and blue regions disappear. The broad signals in the green region also vanish. The ODMR spectra become much simpler. For spectra detected from the violet and green windows as examples (Fig. 5.9 and 5.10, respectively; spectra of the as-grown sample are also included for comparison), only two PL-enhancing signals (v) and (vi) are resolved, which are attributed to deep donor and Mg-related acceptor, respectively. After annealing the intensity of the Mg acceptor signal is relatively stronger than that from the as-grown samples, which gives a further evidence of its assignment. No difference has been found between samples annealed in the two conditions.

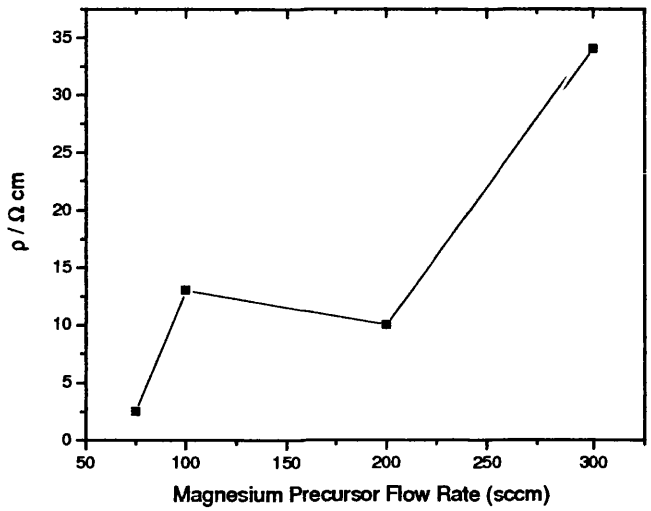

Figure 5.11: The change of resistivity with Mg concentration for samples annealed in nitrogen atmosphere with 0.5% of oxygen. The solid line is used to guide the eye.

5.3.3.1 Concentration dependence

All the annealed samples with different Mg concentrations demonstrate similar ODMR spectra, with small but systematic changes in donor and acceptor g-values with increasing Mg concentration:

Violet:

(v*) $g_{||}$ = 2.075 for the lowest concentration sample (#626a) to 2.084 for the highest concentration sample (#623a) (FWHM = 20 - 26 mT)

(vi*) $g_{||}, g_{\perp} = 1.962 \pm 0.005$ (FWHM = 15 - 20 mT)

Blue:

(v**) $g_{||}$ = 2.066 to 2.072 (FWHM = 17 - 22 mT)

(vi*) $g_{||}, g_{\perp} = 1.962 \pm 0.005$ (FWHM = 15 - 20 mT)

Green:

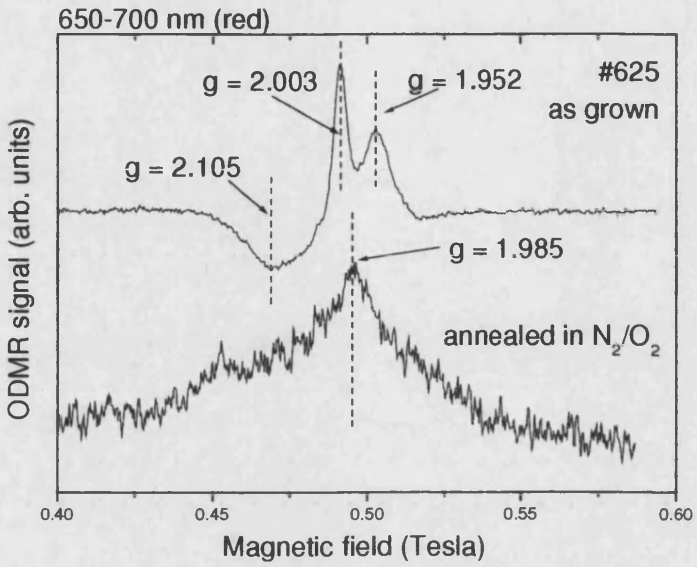

Figure 5.12: ODMR spectra at 13.76 GHz detected on the red (1.77 - 1.91 eV) region for sample #625 before and after annealing. The arrows indicate g-values with $\mathbf{B}\|c$.

(xv) $g_{\|} = 2.045$ to 2.066 (FWHM = 18 - 25 mT)

(xvi) $g_{\|} = 1.965$ to 1.968 (FWHM = 16 - 23 mT)

The g-value increases systematically when the Mg concentration is increased, suggesting that the acceptor level becomes shallower with increasing concentration. Unlike for the as-grown samples, after annealing the linewidth of the acceptor signal (v*) is larger than that of the donor signal (vi*). The intensity ratio of the donor and acceptor signals I_D/I_A increases with increasing Mg concentration (from the values of 0.9 and 1.8 for sample #626a in the violet and the blue regions, respectively, up to 2.0 and 3.5 for sample #623a), probably because the self-compensation process prevails over the acceptor forming process with increasing Mg-doping level. This suggestion is supported by the room temperature Hall-effect measurements, which show that the annealed samples are all of p-type conductivity and the resistivity rises as the Mg concentration is increased (Fig. 5.11). The self-compensation donor therefore exists before and after thermal annealing.

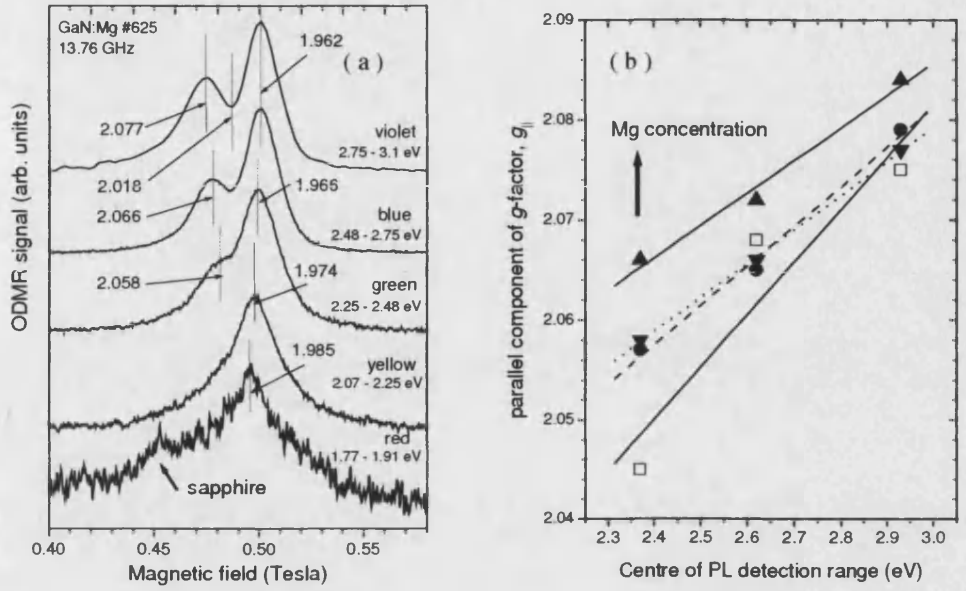

Figure 5.13: (a) ODMR spectra of sample #625a for a series of PL energy ranges. The g-value of the peaks are indicated by the arrows. (b) Trends in the acceptor $g_{||}$ factors (as determined by ODMR) with the PL detection energy range. Data was obtained in three ranges for #626a (□), #625a(●), #624a(▼), #623a(▲) and the lines show linear fits to each set of three points.

Red and NIR:

The ODMR signals from the red region become very weak after annealing (Fig. 5.12), in accordance with the suppression of the red PL upon annealing (Chapter 3). Only a deep donor signal is detected from sample #625a:

(xvii) $g_{||} = 1.985$ (FWHM = 28 mT)

The signals from the Mg-doped layer in the NIR region are fully suppressed after annealing and hence not shown.

Table 5.2: Summary of the g-values observed in Mg-doped GaN in this work: annealed samples

Index		Assignment	$g\|\|$	$g_\perp$	FWHM, mT	Detection window
1	(v*)	Mg acceptor	2.075 to 2.084	~ 2.0	20-26	violet
2	(v**)	Mg acceptor	2.066 to 2.072		17-22	blue
3	(xv)	Mg acceptor	2.045 to 2.066		18-25	green
4	(vi*)	Deep donor	1.962		15-20	violet, blue
5	(xvi)	Deep donor	1.965 to 1.968		16-23	green
6	(xvii)	Deep donor	1.985		28	red

5.3.3.2 Wavelength dependence

ODMR spectra for an annealed sample of intermediate concentration (#625a) detected from different spectral windows are shown in Fig. 5.13a. A shift of $g_{||}$ with PL energy is observed; in particular, the Mg-related acceptor signal moves steadily to higher fields with increasing monitoring wavelength and becomes relatively weaker. In the red and the NIR regions the acceptor signal becomes unresolvable. This trend (which has also been noted previously [74]) is summarized in Fig. 5.13b for this sample and the three others (#626a, #624a, #623a) studied: $g_{||}$ is plotted versus the center energy of the detection window. On the left hand side of this figure, the data points going upwards with increasing Mg concentration. For three of the samples(#625a, #624a, #623a) the rate of change of $g_{||}$ with PL energy is roughly the same ($dg_{||}/dU =\sim 0.040$ eV^{-1}) and for the lowest-doped sample (#626a), it is slightly larger. At the same time the donor-related signal shifts in the opposite direction. In Ref. [85] a model accounting for the variations in g-values observed for Mg-related acceptors in GaN has been proposed by our group and discussed extensively.

The ODMR signals observed in this work from the annealed samples are summarized in Table 5.2.

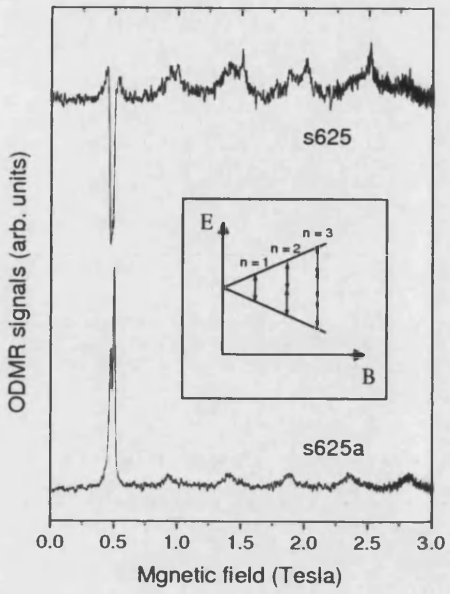

Figure 5.14: Typical ODMR spectra showing multiquantum transitions at 13.76 GHz detected on the violet (2.75 - 3.1 eV) region for sample #625 before and after annealing. The inset shows an energy level diagram illustrating multiquantum transitions.

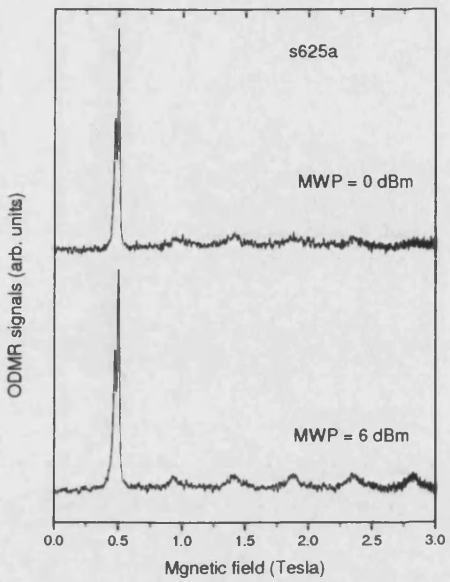

Figure 5.15: Multiquantum ODMR spectra detected under different microwave powers increased by a factor of 4 for sample #625 after annealing.

5.3.4 Multiquantum ODMR signals

Additional ODMR signals from both the as-grown and the annealed samples are observed in the fields which are 2, 3 and so on times as high as the normal transitions from the violet region at high microwave power. Such signals are ascribed to magnetic transitions with the absorption of multiple (n) microwave quanta ($n > 1$) [107]. Typical spectra for an as-grown sample (#625) and an annealed sample (#625a) are shown in Fig. 5.14, with simplified energy level diagram illustrating multiquantum transitions. It is shown that although from I_X the ODMR signals around 0.5 T are of opposite signs for the as-grown and the annealed samples, the multiple quanta-related signals are all PL-enhancing. For the $n > 1$ transitions, before annealing the intensity of the donor signals is bigger than that of the acceptor signals, while after annealing the acceptor signals dominate the spectra. This observation further supports the model of the effect

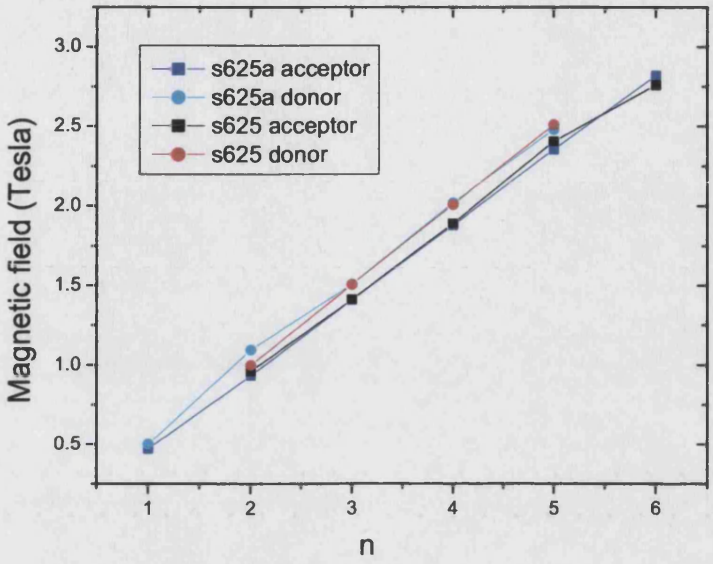

Figure 5.16: The peak positions of the n$\geqslant$1 multiquantum ODMR signals as a function of n for sample #625 before and after annealing. Error bars lie within the size of the points

of annealing on the Mg acceptor activation (Sec. 5.3.3). The magnetic fields of the transitions can be obtained by fitting the spectra with Lorentzian shape lines. Fig. 5.16 shows the peak positions as a function of n. Note that a linear fit to the data does not necessarily pass through zero, due to the interaction of the centres with each other. For both the as-grown and the annealed samples, the transition fields of the donor and the acceptor increase linearly with n, indicating that all the signals can be fitted by the spin of 1/2. The gradients of the donors and the acceptors, which are determined by the g-values of the centres, show no obvious change before and after annealing, indicating that the same pair of donor and acceptor are involved. Fig. 5.15 demonstrates the spectra of the annealed sample (#625a) under different microwave powers, which increase by a factor of 4 from the upper trace to the lower trace. Under high microwave power only the high order transitions (n $\geqslant$ 3) shows an obvious increase in amplitude, implying that the low order transitions are probably saturated. The observation of MQR makes it possible to improve the resolution of the ODMR lines with different g-values.

5.4 Discussion

5.4.1 Origins of the 3.15 eV and 2.8 eV bands

For the as-grown samples, I_Y gives the same pair of signals, with $g_{||}, g_{\perp} = 1.967 \pm 0.005$ for the deep donor and $g_{||} = 2.08 \pm 0.01$ for the Mg acceptor, from both the violet and the blue regions for samples of all Mg concentration. Increasing Mg concentration leads to an increased contribution of this deep donor-to-Mg acceptor transition (Fig. 5.2, 5.5), probably because the concentration of the Mg-related acceptor and/or the self-compensating donor is increased. The pair of signals are therefore most probably associated with the 2.8 eV band. As discussed in Chapter 3, the deep donor is assigned to $V_N - Mg_{Ga}$, which is a deep compensating defect in Mg doped GaN and is also involved in the red PL band. Our violet detection window is 2.75 - 3.1 eV that can include both the tail of the 3.15 eV and the 2.8 eV transitions. However, there are no 3.15 eV PL band related signals detected from the violet window. One possible reason is that the recombination lifetime of this band is not sufficiently long for magnetic dipole spin transitions to take place. A time-resolved PL study at 10 K gave recombination lifetimes of 0.6-5 ns for the 3.15 eV luminescence [108] and $\sim$ 700 ns for the 2.8 eV luminescence [71]. Generally, the lifetime should be longer than 1μs for the necessary sensitivity in ODMR to be achieved. Although the defect centers directly involved in the recombination process are not detectable, in the high excitation power regime it is possible to detect competing centres if the lifetimes of the competing recombination processes are long enough.

Very similar deep donor and Mg acceptor ODMR signals are observed for the annealed samples from the violet and blue windows, indicating that the self-compensating deep donor ($V_N - Mg_{Ga}$) exists before and after annealing. Therefore, in this study we conclude that the $V_N - Mg_{Ga}$ complexes do not contribute to the activation of p-type conductivity in the annealing. It is widely accepted that hydrogen is unintentionally incorporated during MOVPE of Mg-doped GaN, passivating the Mg acceptors and causing the as-grown material to be highly resistive [109]; the MgH complex is a neutral defect. Theoretical calculations using density-functional theory suggests that the dominant configuration consists of

H at an antibonding site of a N neighbor of the substitutional Mg, with the Mg-N and N-H bonds nearly aligned and the N-H bond oriented at an angle of $\sim$ 109° with the c axis [110]. A high-temperature vacuum-ambient and N_2-ambient annealing is sufficient to remove H and activate the p-type doping. The high resistivity can be restored by re-hydrogenation after NH_3 -ambient annealing [109].

The change of energy of the dominant PL band from 3.15 eV down to 2.8 eV with increasing Mg concentration is widely reported. Both bands show donor-acceptor pair (DAP) like behaviour in this study when the excitation energy is changed. In the literature two DAP models have been suggested. In the model proposed by Glazer et al [67], it is the same DAP that is involved in both bands. The donor and the Mg acceptor are both shallow, and the energy shift is due to the present of large potential fluctuations [67]. In the other model, the 2.8 eV PL band in heavily Mg-doped GaN is related with the formation of deep donors and the 3.15 eV band is associated with shallow donors [49, 70, 111, 112]. From the discussion above, our observation supports the second model, since although no signal directly related to the 3.15 eV band was observed, at least two donor signals (i.e., (vi) and (vii)) are detected from each of the as-grown sample and they can be responsible for the blue and violet bands respectively. The shift of emission from violet to blue can be explained by increase of probability of the deep donor-Mg acceptor recombination with Mg doping. As discussed in Chapter 3, the assignment of the shallow donor to a $V_N - H$ complex is favoured in our case. The defect centre dissociates after annealing, with H diffusing either to the surface or to the extended defects. The $V_N - Mg_{Ga}$ centres can also be formed during annealing as the remaining V_N diffuses towards activated Mg_{Ga}.

5.4.2 Origins of the deep centres MM1 and MM2

The ODMR spectra from the NIR region suggest that the MM2 deep centre and the Mg acceptor are involved in the NIR recombination process. The transfer of carriers from the MM1 center to the MM2 center is also possible [51]. The MM2 center behaves like a donor in this study. Taking into account the Mg acceptor level depth about 150-350 meV above the valence band, it can be concluded that

the energy level of the MM2 center is in the midgap region at about 1.7 - 1.9 eV below the conduction band. For the sample with the highest Mg concentration (#623) no ODMR signal from the GaN : Mg layer is detected in the NIR region, probably because the MM2 center is destroyed by Mg-doping. Annealing also destroys the MM2 centre, leading to the disappearance of NIR ODMR signals. The destroying of the MM2 centre with Mg-doping and annealing is very similar to that of the MM1 centre, which is discussed in Chapter 3. The concentration of the MM1 centre (V_{Ga} or related complexes) decreases with Mg-doping and the centre is eliminated after annealing due to the movement of the Fermi level with Mg acceptor activation. Therefore the decrease of defect concentration with Fermi level may explain our experimental observation that the annealing process has a similar effect to the increasing Mg concentration. In Ref. [109], Nakamura *et al* observed a broad deep level emission (DL emission) at around 750 nm from as-grown high-resistivity GaN : Mg samples as well as LEEBI-treated films with further H-passivation of acceptors (by either NH_3-ambient thermal annealing or microwave plasma treatment). It is suggested that the DL emissions are caused by Mg-H complexes related levels. Our experimental observation does not support the assignment of MM2 centre to a neutral Mg-H complex, since the complex should not be eliminated with increasing Mg concentration. Furthermore, the complex is not a paramagnetic centre and hence, in normal situations, it should not be detectable in ODMR measurements. More experiments are needed to decide the chemical origin of the MM2 centre.

5.4.3 Nature of the Mg acceptor states

The closeness of the g-value of the Mg acceptor to 2.00 implies that the hole wave-function is well-localized. A hole may be based on nitrogen $2p$ functions assuming that a Mg^{2+} ion substitutes at a Ga^{3+} site. A rather general Hamiltonian for the hole state is as follows. It contains, respectively, the Zeeman splittings due to the spin and orbital angular momenta (operators **s** and **l**), the axial wurtzite (C_{3v}) crystal field with parameter Δ_{cfz}, a possible symmetry-lowering crystal field term (Δ_{cfx}) and the spin-orbit interaction (λ, where $\lambda < 0$ for holes); μ_B is the Bohr

magneton, $g_l = 1.00$ and $g_s = 2.00$:

$$H_{total} = g_s\mu_B \mathbf{B}.\mathbf{s} + g_l\mu_B \mathbf{B}.\mathbf{l} + \Delta_{cfz}[l_z^2 - l(l+1)/3] + \Delta_{cfx}[l_x^2 - l(l+1)/3] + \lambda \mathbf{l}.\mathbf{s}. \quad (5.1)$$

This Hamiltonian results in a ground state that is a spin doublet, for which the Zeeman splitting can be characterized by g-factors $g_{\|}$ and $g_{\perp}$ whose values depend critically on the details of the model. To be in agreement with the experimental g-values, we suggest that the hole is probably localized on one of the nitrogen atoms in the non-c-axis bond direction relative to Mg and with a lower symmetry, giving $\Delta_{cfx} \neq 0$. In the calculation, we take $|\Delta_{cfz}| >> |\Delta_{cfx}| >> |\lambda|$, which causes g_x and g_y to be approximately equal (and hence identifiable with the experimentally observed $g_{\perp}$). In the limit where perturbation theory can be applied, the following expressions are obtained: $g_x = 2.00$, $g_y = 2.00 - 2\lambda/(|\Delta_{cfz}| + |\Delta_{cfx}|) \approx 2.00$ and $g_z = 2.00 - 2\lambda/|\Delta_{cfx}|$. It is clear that the value of g_z is highly sensitive to the size of the non-axial crystal field Δ_{cfx} (due to nearby defects or to strain). As the acceptor is increasingly perturbed, the acceptor level moves further into the gap as the energy splitting $|\Delta_{cfx}|$ increases. It shows that the different acceptor states are formed by simple substitution of a Mg ion at a Ga site, rather than by the creation of a more complicated defect. Whether the acceptor is shallow or deep is found to be dependent on the strength of the low symmetry perturbation in its vicinity. Thus, different strains, induced for example, by different growth conditions or doping levels, lead to different g-values and to different acceptor depths, the latter giving the possible misleading impression that there are a large number of acceptors of different origins. The need for the low symmetry fields to be small if the acceptor states are to be shallow emphasizes the need for high quality material if effective p-type doping is to be achieved. For a thorough discussion of the nature of the Mg acceptor states in GaN, please refer to Ref. [85].

5.5 Conclusions

ODMR experiments have been carried out on a series of Mg doped GaN layers grown by MOVPE, with particular emphasis on the changes produced by increasing Mg concentration and annealing the layers in nitrogen atmosphere with and without a small fraction (0.5%) of oxygen in it. Both increasing Mg concentration and annealing lead to similar transformations of the shape of the low-temperature and room-temperature PL spectra, making the 2.8 eV (2.9 eV at room-temperature) PL band dominate. Low concentration as-grown specimens show complicated ODMR spectra, with signals due to Mg-related acceptors and to a range of deep and shallow donors. Both positive (luminescence enhancing) and negative (luminescence quenching) ODMR signals are observed. The signs and magnitudes of the signals are of strong functions of the Mg doping level.

Following annealing, in the violet and blue regions the ODMR spectra become much simpler, being dominated by signals due to the Mg-related acceptors and to the compensating $V_N - Mg_{Ga}$ deep donors; the broad spectra observed in the green region and the signals from the red-infrared region are reduced or disappear. Our study shows that the $V_N - Mg_{Ga}$ deep donor, contributing only to electrical compensation of Mg, is not involved in the *p*-type conductivity activation process in the annealing. On the other hand, the Mg-H complexes, which are produced by hydrogen passivation and causes the high resistivity of as-grown samples ([109]), were not detected in the ODMR experiments, probably because these centres are not paramagnetic and/or are not involved in the PL processes. The elimination of deep centres (e.g. MM1 and MM2) with Mg doping and annealing is probably due to the decrease of their concentration associated with the movement of the Fermi level. The nature of the Mg acceptor states in annealed GaN is also discussed and a model is proposed, which identifies the importance of the symmetry-lowering crystal field to the *g*-values and depth of the Mg acceptors.

Chapter 6

Recombination processes and spin dynamics in Mg doped GaN probed by ODMR waveform studies

6.1 Introduction

In the previous chapter schematic recombination models have been suggested for Mg doped GaN samples. In the lightly doped case the model is rather complicated, with some defect levels involved in more than one recombination channel. This conclusion was drawn from the ODMR results. Generally speaking, a positive (PL-enhancing) signal indicates the defect centers are directly involved in the recombination process being monitored; while a negative (PL-quenching) signal suggests the centers are involved in the recombination process which competes with the PL transitions being monitored. For a given sample monitored at different wavelengths, some defect centers give either an enhancing signal or a quenching one, indicating the role of those centers in the recombination process has changed. In this chapter a simple rate-equation model [113] is adopted to describe the MM2 deep defect to Mg acceptor (infrared) and competing $V_N - Mg_{Ga}$

deep donor to Mg acceptor (blue) recombination. We show that the model can successfully explain the experimental observation that the donor resonance can be observed both as an enhancing resonance of the blue PL and as a quenching resonance of the infrared PL. The model is also capable of describing the waveforms of the change of the blue and infrared PL as a function of time. A very similar rate equation model can be directly applied for the red emission and competing blue emission (i.e., two acceptors competing for recombination with the same donors). A simple two-level rate equation model is also discussed and the simulation results are compared with those obtained by use of the first model. The simulations further clarify the spin dynamics and characteristics of the magnetic sites.

6.2 Experimental details

The MOVPE grown GaN : Mg sample with the lowest Mg concentration (#626) was investigated in this study. The details of the sample and the ODMR experimental set-up can be found in earlier chapters. To obtain the waveform, the photomultiplier output was monitored directly by use of an integrating oscilloscope.

6.3 Experimental results and discussions

6.3.1 Infrared emission and competing blue emission

The energy-level diagram illustrating the blue and infrared recombination processes is presented in Fig. 6.1. ODMR spectra and waveforms obtained by monitoring the two PL bands are shown in Fig. 6.2(a) and (b). Two resonance signals are resolved in the blue region. The g-values are $g_{||} = 2.08 \pm 0.01$ for the Mg acceptors and $g_{||} = 1.967 \pm 0.005$ for the $V_N - Mg_{Ga}$ complexes. The waveform obtained under the donor resonance condition shows a strong spike

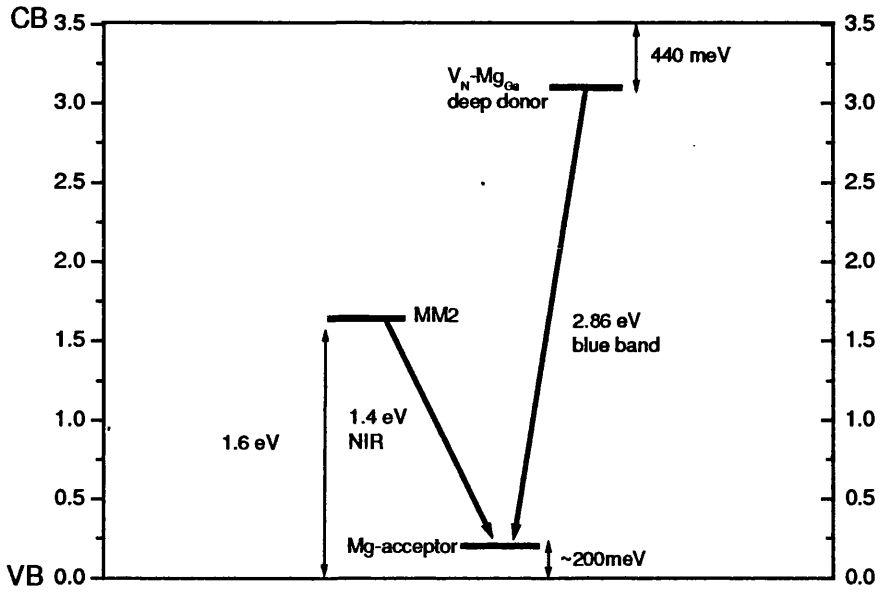

Figure 6.1: Schematic diagram for the recombination processes giving rise to the blue and NIR bands of GaN.

at the rising edge of the microwave power, which decays quickly to an approximate quasi-equilibrium situation in the presence of the microwave excitation (Fig. 6.2(a)). There is a negative spike at the falling edge of the microwave pulse, which recovers gradually to zero intensity. In the infrared spectral region two enhancing and one quenching signals were detected. The enhancing signals reveal the donor (MM2 deep defects, $g_{||}, g_{\perp} = 2.005$) acceptor (Mg acceptor, $g_{||} = 2.08 \pm 0.01$) pair which gives the infrared emission. The quenching character of the shallow donor signal of the highest field indicates it competes with the MM2 center for the recombination with the Mg acceptor-bound holes. The waveform obtained under the strong MM2 resonance condition is different from the one from the blue region: As in the blue region, the response shows a sharp spike when the microwaves are turned on followed by a change to a new steady-state level in the presence of the microwave. However, when the microwave power is switched off the PL intensity return to zero without the negative spike.

The rate equations used in a previous study of antisite-to-acceptor and related

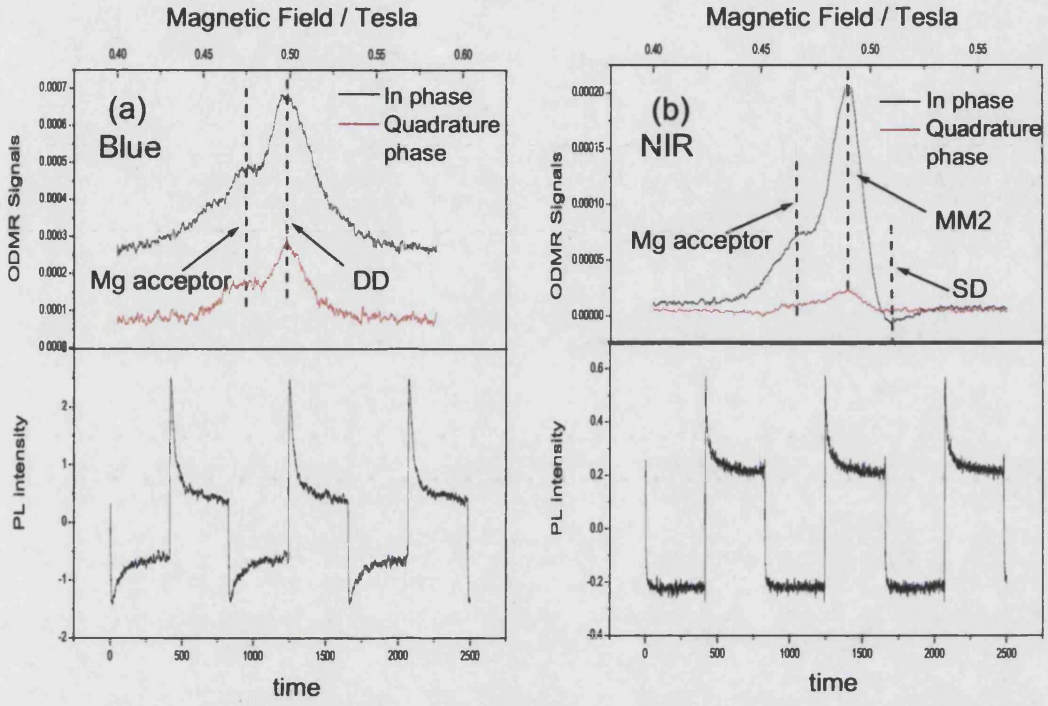

Figure 6.2: (a) ODMR signals obtained via detection of the 2.48 - 2.75 eV PL and the experimental waveform of the deep donor signal. (b) ODMR signals obtained via detection of the 1.13 - 1.46 eV PL and the experimental waveform of the MM2 signal.

recombination processes in as-grown InP:Zn [113] are capable of describing the opposite changes of intensity on the two bands when the antisite resonance occurs, while to explain the shape of the waveforms presented in Fig. 6.2, a spin-lattice relaxation effect has to be included. The pair model for donor-acceptor recombination should be valid as long as the average donor-acceptor separation is much larger than the Bohr radius of the more extended wave function [46]. If both donor and acceptor concentration are of 10^{20} cm^{-3}, the average donor-acceptor separation is estimated to be ~ 17Å, which is comparable to their Bohr radii ($\sim$ 23Å and $\sim$ 5Å for shallow donors and shallow Mg acceptors, respectively). For the lowest concentration sample #626, the donor and acceptor concentration should both be well below 10^{20} cm^{-3}. Therefore the pair model is probably valid in the present work. The donor may be occupied by a spin-up ($\uparrow$) or spin-down ($\downarrow$) electron or may be unoccupied (0). The acceptor may be occupied by a hole

(h) or unoccupied (0). Different hole spin states are not distinguished. The difference in recombination rates for spin-up and spin-down electrons caused by the population imbalance among the various hole spin states are expressed as (1 - α)v_R for the ($\uparrow h$) state and as (1 + α)v_R for the ($\downarrow h$) state. Therefore the pair may exist in six different spin and charge states: ($\uparrow h$), ($\downarrow h$), ($\uparrow 0$), ($\downarrow 0$), ($0h$) and (00). The rate equations revised from those in Ref. [113] can be written as

$$\begin{aligned}
dn_{\uparrow h}/dt &= K_{\uparrow} n_{0h} + K_h n_{\uparrow 0} - [(1-\alpha)v_R + v_{NR} + v_e + v_h] n_{\uparrow h} \\
&\quad - M(n_{\uparrow h} - n_{\downarrow h}) - S n_{\uparrow h} + S' n_{\downarrow h} \\
dn_{\downarrow h}/dt &= K_{\downarrow} n_{0h} + K_h n_{\downarrow 0} - [(1+\alpha)v_R + v_{NR} + v_e + v_h] n_{\downarrow h} \\
&\quad + M(n_{\uparrow h} - n_{\downarrow h}) + S n_{\uparrow h} - S' n_{\downarrow h} \\
dn_{\uparrow 0}/dt &= K_{\uparrow} n_{00} + v_h n_{\uparrow h} - [K_h + v_e] n_{\uparrow 0} - M(n_{\uparrow 0} - n_{\downarrow 0}) \\
&\quad - S n_{\uparrow 0} + S' n_{\downarrow 0} \\
dn_{\downarrow 0}/dt &= K_{\downarrow} n_{00} + v_h n_{\downarrow h} - [K_h + v_e] n_{\downarrow 0} + M(n_{\uparrow 0} - n_{\downarrow 0}) \\
&\quad + S n_{\uparrow 0} - S' n_{\downarrow 0}
\end{aligned} \tag{6.1}$$

where n is the population of the state. K corresponds to the rate of the electrons (or holes) being captured by donors (or acceptors), which is probably spin-dependent. v_R and v_{NR} correspond to the rates for radiative and nonradiative recombination of the electrons and holes, and v_e and the v_h are the rates for the competing recombination of the electrons and the holes, respectively. Microwaves promote carriers from one spin levels to the other with the rate M when the spin resonance condition is met. S and S' are the rates of spin-lattice relaxation induced transitions between the two spin levels, with $S = S'\exp(g\beta_e B/kT)$. In the current study, $g \approx 2$, $B \approx 0.5$ T and $T \approx 1.8$ K, which gives $S = 1.45S'$. To simplify the calculation we assume $S \approx S'$.

To determine the details of the transient behaviour, the four kinetic equations are solved numerically and the populations of the four pair states (($\uparrow h$), ($\downarrow h$),

($\uparrow 0$), ($\downarrow 0$)) are then obtained directly. The time-dependent PL intensity of the donor-acceptor pair recombination directly being monitored can be determined from the equation (for detailed analysis, see Ref. [113])

$$I_{PL}(t) = (1-\alpha)\frac{K_h + v_e}{K_h + v_e + v_h} n_{\uparrow h}(t) + (1+\alpha)\frac{K_h + v_e}{K_h + v_e + v_h} n_{\downarrow h}(t) \qquad (6.2)$$

and the PL intensity of the competing recombination process is

$$I_c(t) = v_c[n_{\uparrow h}(t) + n_{\downarrow h}(t) + n_{0h} + n_h^*] \qquad (6.3)$$

where v_c is the radiative rate of the competing process and n_h^* is the density of acceptors not paired with any of the deep donors that are involved in the recombination process directly being monitored.

Fig. 6.3 (a) to (e) shows the simulation results of the waveforms as a function of time, together with the time dependence of microwave power shown in Fig. 6.3 (f). Curve a corresponds to a condition that both radiative and nonradiative processes are involved, while the radiative emission is dominant ($v_R > v_{NR}$) and the process is thermalized ($S > v_R$). Curve b and c correspond to the PL intensity changes on the monitored band and the competing band under the same condition. It includes similar radiative and nonradiative decay times to those in curve a; however, $S < v_R$ (unthermalized). Curve d involves competing radiative and nonradiative process ($v_R \sim v_{NR}$); the increase of the contribution from the nonradiative process can be observed as a decrease of the transit part of the waveform. Curve e corresponds to the competing band under the same condition as curve d. The experimental waveforms, shown in Fig. 6.2 (a) and (b), resemble the responses shown in curves a and b in Fig. 6.3 respectively, and are displayed together with the simulated results in Fig. 6.3. The simulation results thus indicate that both the blue band and the infrared band correspond to the situation that radiative emission is dominant ($v_R > v_{NR}$), while the infrared band involves a much longer spin-lattice relaxation time than the blue band. Furthermore, curve b and c show opposite changes in intensity on the monitored

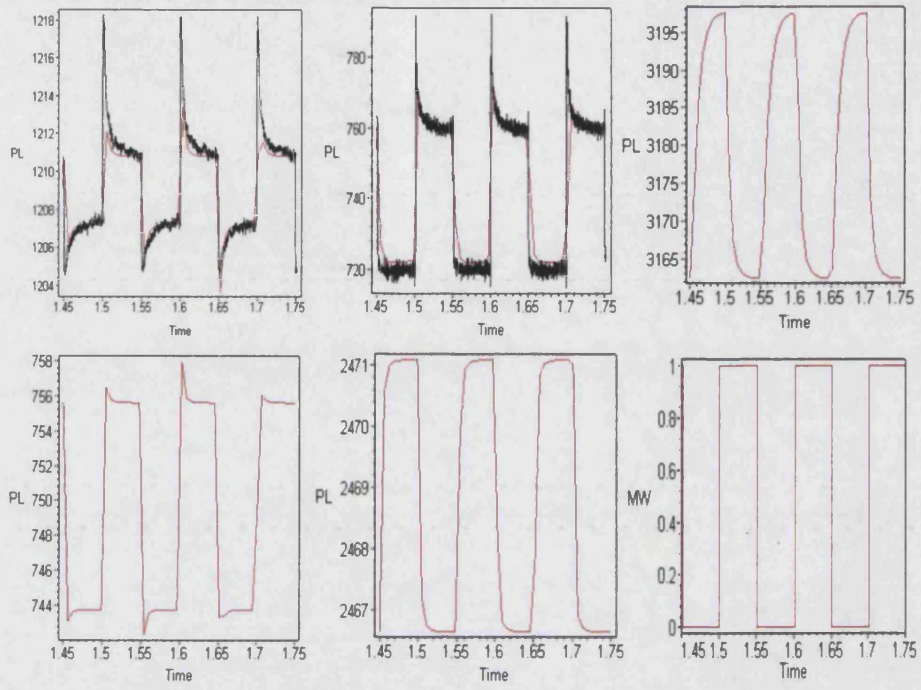

Figure 6.3: (a) - (e) Calculated waveforms on the basis of the rate equation model presented in the text with the following parameters kept constant: $\alpha = 0.5$, $K_{\uparrow} = K_{\downarrow} = 100$, $n_{0h} = 10$, $n_{00} = 10$, $K_h = 100$, $v_h = 100$, $v_e = 100$, $M = 500$. (a) $v_R = 250$, $v_{NR} = 10$, $S = 1000$; (b) and (c) $v_R = 100$, $v_{NR} = 10$, $S = 1$; (d) and (e) $v_R = 250$, $v_{NR} = 250$, $S = 250$; (a) and (b) are displayed together with the experimental waveforms shown in Figure 6.2(a) and (b), respectively. (f)Time dependence of microwave power used in the calculation.

and the competing bands, which agrees with the experimental observations that both enhancing and quenching signals are detected from the infrared band.

While the shapes of the experimental waveforms can be reproduced, there are discrepancies in amplitudes. In the present study, the modulation in the blue and the infrared bands are 0.17% and 0.3%, respectively. The simulation results under the conditions stated above yield the values of 0.4% and 6% correspondingly. On the other hand, a previous study ([46]) shows that when recombination occurs predominantly between nearest donor-acceptor pairs, at X-band at 2K maximum intensity changes of 2% are predicted at resonance when the system is thermalised. In contrast, when the recombination occurs before thermalisation is achieved, much larger changes can be observed. Our experimental and simulation results do not contradict the conclusion that under unthermalised conditions (the

NIR band) the modulation of PL is much bigger than under thermalised conditions (the blue band). It is also indicated from Eq. 6.3 that the intensity of the quenching signal is proportional to v_c, which increases with laser excitation power. This trend with laser power is also observed (reported in Chapter 3).

6.3.2 Red emission and competing blue emission

Although the rate equation model described above is designed for the case that two different donors compete for recombination with certain acceptors, it can be also applied directly to the opposite case, i.e., two different acceptors competing for recombination with certain donors. The six spin and charge states (($\uparrow h$), ($\downarrow h$), ($\uparrow 0$), ($\downarrow 0$), ($0h$) and (00)) are then revised to six new states: ($e\uparrow$), ($e\downarrow$), ($0\uparrow$), ($0\downarrow$), ($e0$) and (00) and the rate equations can be written

$$\begin{aligned}
dn_{e\uparrow}/dt &= K_{\uparrow}n_{e0} + K_e n_{0\uparrow} - [(1-\alpha)v_R + v_{NR} + v_e + v_h]n_{e\uparrow} \\
&\quad -M(n_{e\uparrow} - n_{e\downarrow}) - Sn_{e\uparrow} + S'n_{e\downarrow} \\
dn_{e\downarrow}/dt &= K_{\downarrow}n_{e0} + K_e n_{0\downarrow} - [(1+\alpha)v_R + v_{NR} + v_e + v_h]n_{e\downarrow} \\
&\quad +M(n_{e\uparrow} - n_{e\downarrow}) + Sn_{e\uparrow} - S'n_{e\downarrow} \\
dn_{0\uparrow}/dt &= K_{\uparrow}n_{00} + v_e n_{e\uparrow} - [K_e + v_h]n_{0\uparrow} - M(n_{0\uparrow} - n_{0\downarrow}) \\
&\quad -Sn_{0\uparrow} + S'n_{0\downarrow} \\
dn_{0\downarrow}/dt &= K_{\downarrow}n_{00} + v_e n_{e\downarrow} - [K_e + v_h]n_{0\downarrow} + M(n_{0\uparrow} - n_{0\downarrow}) \\
&\quad +Sn_{0\uparrow} - S'n_{0\downarrow}
\end{aligned} \tag{6.4}$$

Very similar to the previous case, the time-dependent PL intensity of the directly monitored and competing donor-acceptor pair recombination are

$$I_{PL}(t) = (1-\alpha)\frac{K_e + v_h}{K_e + v_e + v_h}n_{e\uparrow}(t) + (1+\alpha)\frac{K_e + v_h}{K_e + v_e + v_h}n_{e\downarrow}(t) \tag{6.5}$$

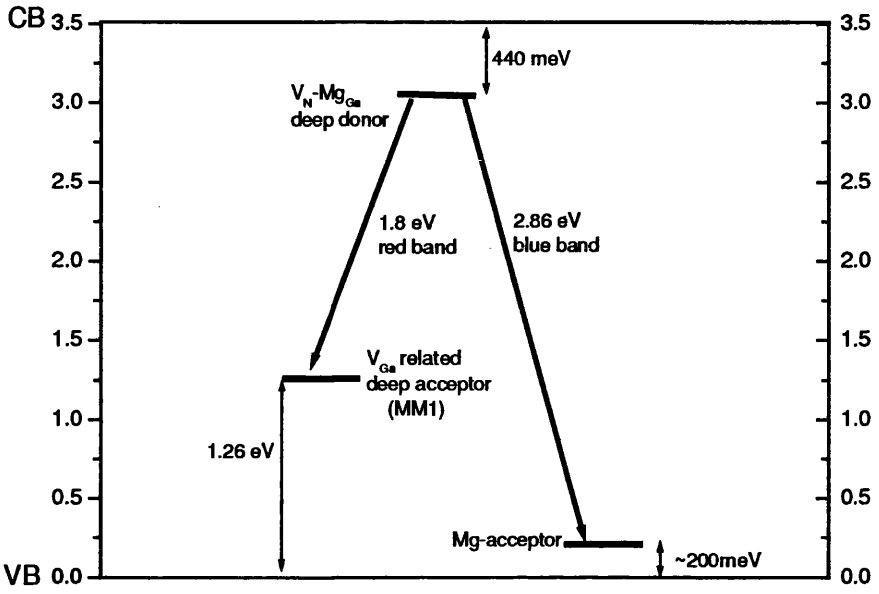

Figure 6.4: Schematic diagram for the recombination processes giving rise to the blue and red bands of GaN.

and

$$I_c(t) = v_c[n_{e\uparrow}(t) + n_{e\downarrow}(t) + n_{e0} + n_e^*] \tag{6.6}$$

where v_c is the radiative rate of the competing process and n_e^* is the density of donors not paired with any of the deep acceptors that are involved in the recombination process directly being monitored.

In the sample with the lowest Mg concentration (#626) the red emission and competing blue emission fall into this case (Fig. 6.4). Fig. 6.5 shows the ODMR signals detected on the red PL band of the sample, together with the waveforms obtained under the resonance conditions. Both PL-enhancing (V_{Ga} or related complexes, $g_{||}, g_{\perp} = 2.003 \pm 0.003$ and $V_N - Mg_{Ga}$, $g_{||} = 1.967 \pm 0.005$) and PL-quenching (shallow Mg acceptors, $g_{||} = 2.105$) ODMR signals were detected. The PL-enhancing waveform is similar to neither the one from the blue band nor the one from the infrared band. It is closer to a square wave. At the rising edge of the

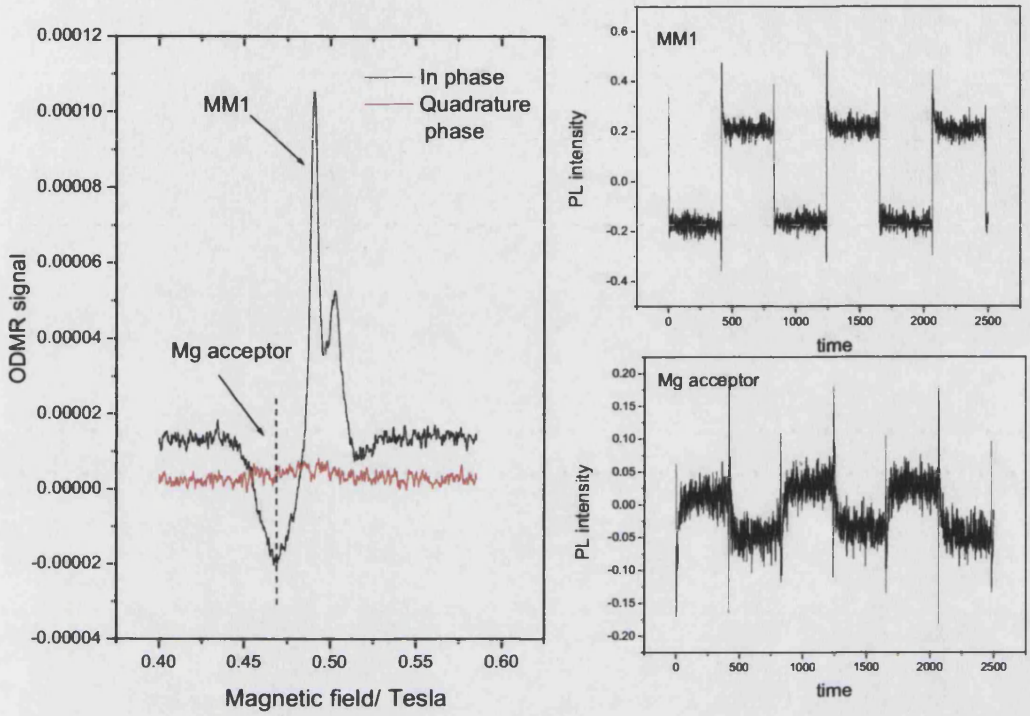

Figure 6.5: ODMR signals obtained via detection of the 1.77 - 1.91 eV PL and the experimental waveforms of the MM1 and the Mg acceptor signal.

microwave power there is a weak spike which decays very fast to the equilibrium plateau; at the falling edge of the microwave power the PL intensity return to zero without the negative spike. It is suggested from the simulation results of the previous section that the lack of a strong transient part of the waveform indicates that competing radiative and nonradiative recombination is involved in the recombination process ($v_R \sim v_{NR}$). The red luminescence is thus different from the blue and the infrared luminescence in the way that the contribution of the nonradiative process is increased. Although very weak, the waveform of the PL-quenching signal is also detected, which clearly shows the negative-going PL intensity change when microwave power is on.

6.4 Two-level rate equation model

In addition to the model discussed above, there are other rate equation models which are capable of describing the dynamics of the ODMR process [43, 46, 114]. Previous attempts to explain the shape of the waveforms of both the ODMR signals and the non-resonant background signal based on a two-level rate equation model have been successful [43]. The two-level model is essentially a simplification of the four-level model discussed in Ref. [46], in which four excited spin levels $|++\rangle$, $|+-\rangle$, $|-+\rangle$ and $|--\rangle$ are formed by combining the two spin states of the acceptor with the two spin states of the donor. When the spin state populations are determined predominantly by the optical selection rules, it is sufficient to represent the problem by two excited levels, assuming from one level (n_1) radiative recombination can take place rapidly and from the other (n_2) it is negligibly weak. Carriers are pumped into the two levels with rates g_1 and g_2, respectively. Non-radiative recombination is assumed to take place from both levels (rates v_{NR1}, v_{NR2} respectively) and radiative recombination only from level 1 (rate v_R). Spin-lattice relaxation induces transitions between the two levels with rates t_1 and t_2, respectively. Microwaves promote carriers from the non-radiative level to the radiative one with a rate M when the spin resonance condition is met. The occupations of the two levels as a function of time can then be written as

$$\begin{aligned} dn_1(t)/dt &= g_1 - [t_1 + v_{NR1} + v_R]n_1(t) + [t_2 + M(t)]n_2(t) \\ dn_2(t)/dt &= g_2 + t_1 n_1(t) - [v_{NR2} + t_2 + M(t)]n_2(t) \end{aligned} \tag{6.7}$$

The disadvantage of the two-level model is that it makes a complete analysis of the directly monitored recombination process together with the competing recombination process intractable. However, the waveforms obtained by solving Equation 6.7 numerically can still reproduce all the main features of the experimental data. The general change of the shapes of the waveforms with some of the rate parameters is still observed as discussed in the previous sections. The calculated waveforms, together with the time dependence of the microwave power, are

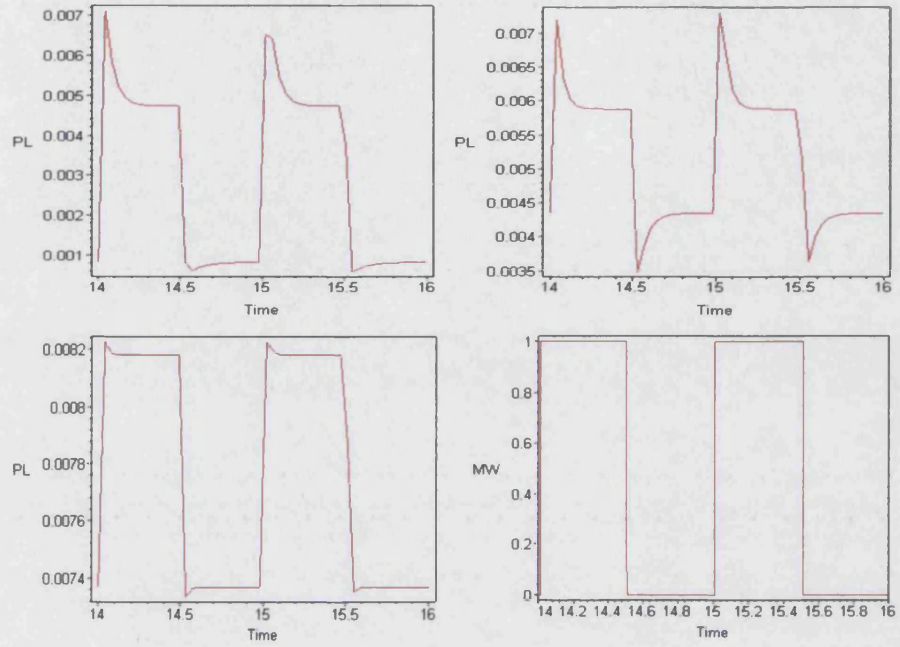

Figure 6.6: (a) - (c) Calculated waveforms on the basis of the rate equation model and parameters presented in the text; (d)Time dependence of microwave power used in the calculation.

presented in Fig. 6.6. In all the calculations the following parameters are kept constant: $g_1 = 0$, $g_2 = 1$, $v_R = 100$, $M = 10$. Fig. 6.6 (a) corresponds to a rather long spin-lattice relaxation time ($t_1 = t_2 = 1$) and $v_{NR1} = v_{NR2} = 10$; Fig. 6.6 (b) is under the same conditions as (a) except that the spin-lattice relaxation time is ten times shorter ($t_1 = t_2 = 10$); Fig. 6.6 (c) involves a nonradiative recombination rate five times of those employed in (a) and (b) ($v_{NR1} = v_{NR2} = 50$) and $t_1 = t_2 = 10$. The emission intensity is given by $I_E = \alpha v_R n_1$ and has the same time dependence as n_1.

6.5 Conclusions

Two simple rate equation models have been employed to study the recombination processes and spin dynamics in Mg doped GaN. The first model has been adopted to describe the competing recombination processes in the sample with the lowest Mg concentration. The model is capable of describing the opposite changes of

intensity on the two competing bands when the resonance occurs. Both models are able to represent the experimental waveforms of the change of PL intensity with the microwave power switched on and off. It is suggested that both the blue and the infrared bands correspond to the situation that radiative emission is dominant ($v_R > v_{NR}$), while the infrared band involves a much longer spin-lattice relaxation time than the blue band. Unlike the blue and the infrared bands, the red band corresponds to a much increased contribution of the nonradiative recombination processes.

Chapter 7

ODMR studies of MBE grown Mg doped GaN

7.1 Introduction

Although the majority of the commercialized III-nitride based optoelectronic devices are fabricated by metalorganic vapor phase epitaxy (MOVPE), the interest in developing high quality materials and devices using molecular-beam epitaxy (MBE) is still of both academic and commercial interest. MBE has several advantages over MOVPE, e.g., the ability to produce materials with more flexible growth parameters and high interfacial growth control [95]. MBE-grown LEDs usually have output power well below 0.1 mW (see, e.g., Refs. [115], [116]), while recently packaged devices with output powers up to 0.87 mW at 20 mA forward current have been reported [117]. In January 2004 the first MBE-grown InGaN LD was achieved by Sharp Laboratories of Europe Ltd. The device operates at room temperature but only under low duty cycle (0.01%) pulsed current injection [118]. Further improvements in device characteristics have also been reported by using free-standing GaN substrates and a pulsed current duty cycle of 10% has been achieved [119]. These results demonstrate the potential of MBE as a suitable growth technique for high quality InGaN-based optoelectronic devices. It is therefore of interest to investigate the defects involved in the recombination

Table 7.1: Carrier concentration and mobility of sample #736 to #739.

	Carrier concentration (cm^{-3})	Mobility ($cm^2/V.s$)
#736	6e16	14.6
#737	1.5e17	9
#738	-1.3e17	53
#739	-1.8e17	35

processes in MBE grown Mg doped GaN epilayers and compare the results to those for example grown by MOVPE.

7.2 Experimental Details

In this study 14 GHz ODMR and room temperature PL experiments were performed on five MBE grown epitaxial layers from Sharp Laboratories of Europe Ltd. (#736, #737, #738, #739) and from Bremen University (#0855). The experimental set-up and conditions are as described in previous chapters. The samples from Sharp are of a series of Mg concentrations, which was achieved by increasing the Cp_2Mg flux used as Mg source. For all the samples, the MBE layers are $\sim$ 2 μm thick and grown on MOVPE-GaN templates (3μm thick). Room temperature Hall measurement was performed at the Sharp Laboratories and carrier concentration and mobility of the samples are presented in Table 7.1. The data shows that with increasing Mg flux, the samples change abruptly from n-type to p-type and the mobility increases by about a factor of 5. The sample # 0855 is grown on an undoped MOVPE buffer ($\sim$ 1 μm). The thickness of the Mg doped layer is $\sim$ 0.5 μm. The Mg concentration in the sample is around $5 \times 10^{19} cm^{-3}$.

7.3 Experimental results and discussions

The room temperature PL spectra are dominated by the near band-gap recombination (Fig. 7.1 (a) and (b)). The 3.27 eV shallow donor to shallow acceptor

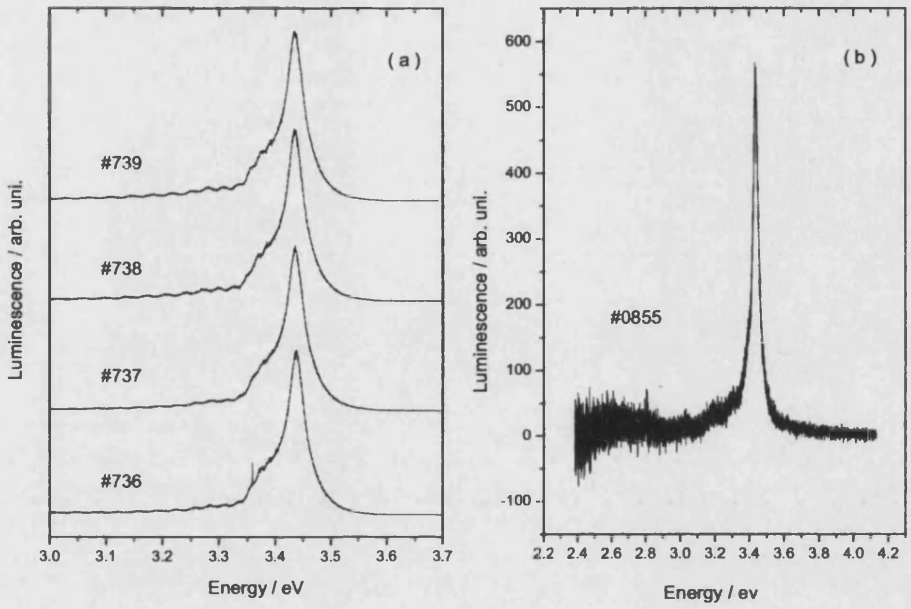

Figure 7.1: Room temperature PL spectra of the MBE grown samples (a) #736 to #739 with different Cp_2Mg flux rates increased from #736 to #739 (b) #0855.

(SD-SA) recombination is weak in the samples and is present as a tail of the near band-gap emission. The 2.8 eV blue band was not detected. A broad green band was observed in the Bremen sample whose origin is not clear yet (Fig. 7.1 (b)).

In ODMR measurements no signal was detected in the violet and blue spectra regions. Possible explanations are as follows: firstly, the disappearance of the 2.8 eV "blue" PL band indicates that no $V_N - Mg_{Ga}$ deep donor exists in the MBE samples. Secondly, the shallow donor and shallow acceptor involved in the 3.27 eV PL band are normally not directly detectable in our ODMR system, probably due to the short lifetime of this recombination process. The lack of $V_N - Mg_{Ga}$ centers may explain the observation of a continuous increase of the free hole concentration as the Mg dopants are increased in MBE grown samples, compared with the saturation character of MOVPE grown samples [120]. For all the MBE grown samples, broad, isotropic signals were detected in the green spectral region, which have been discussed in Chapter 4.6 and compared with

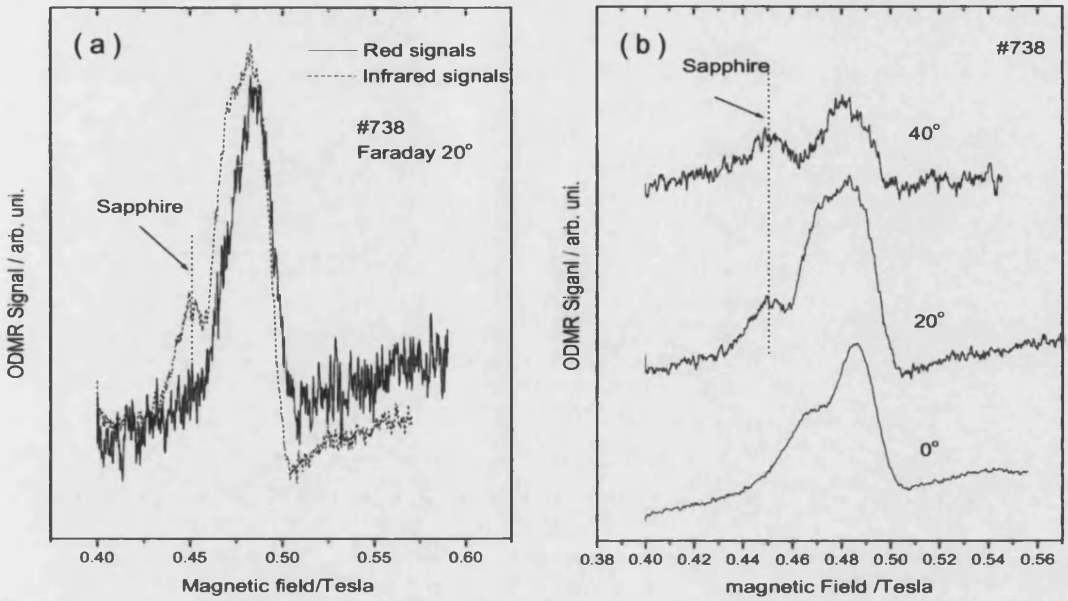

Figure 7.2: (a) ODMR spectra obtained from the red (solid line) and NIR (dotted line) spectral regions for sample #738 in Faraday 20°. (b) ODMR of the sample #738 from the violet spectral region as a function of the angle between the c-axis and the magnetic field.

green signals from MOVPE grown samples. Therefore in this chapter we concentrate on signals from the red/NIR region. In the red and infrared spectral regions similar overlapping signals were detected, with the red signals narrower than the infrared ones (Fig. 7.2(a)). The low magnetic field peak appearing in the infrared region comes from the sapphire substrate (Fig. 7.2(b)). The signals can be decomposed into two Gaussian peaks. As an example, sample n738 gives deep donor and deep acceptor signals with c-axis g-values of 2.07 (FWHM $\sim$ 27.56 mT) and 1.998 (FWHM $\sim$ 13.27 mT) respectively. When the angle between the the magnetic field and the sample c-axis is increased, the acceptor signal moves towards the high magnetic field direction (Fig. 7.2(b)). The signal is very similar to the $g_{||} = 2.07$, $g_{\perp} = 2.03$ (FWHM $\sim$ 45 mT) PL-EPR signal assigned to deep Mg-related complex and observed for both as-grown and annealed MOVPE grown samples [105]. The complex is not responsible for the p-type conductivity [105]. Although the g-value of the deep donor is close to that of both the MM1 (V_{Ga} related) and MM2 signals in the MOVPE grown samples (reported in Chapter 3 and 5), they are not from the same origin. MM1 is an acceptor signal and the formation energy of the acceptor-like defect rises as the Fermi level moving

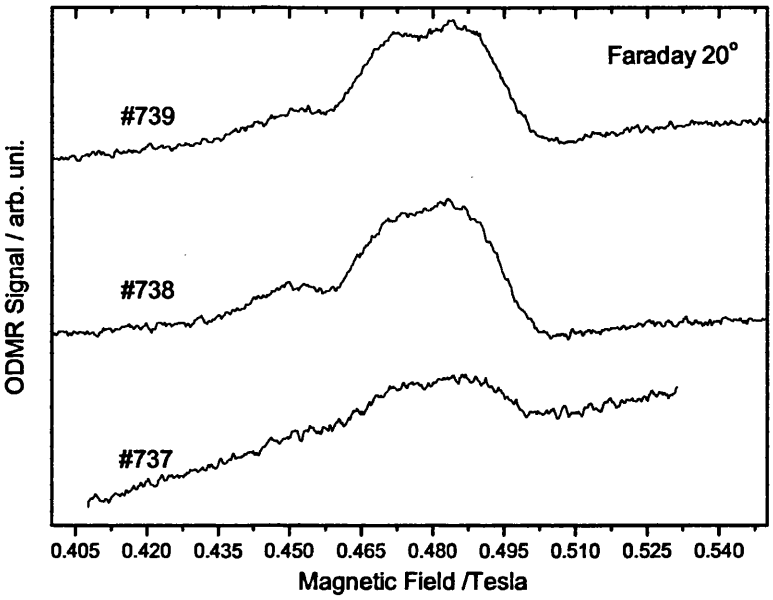

Figure 7.3: ODMR spectra obtained from the NIR spectral regions for samples #737, #738 and #739 with different Mg concentrations increased from #737 to #739.

towards the valence band. MM2 is also removed with Mg doping. In this study with increasing Mg flux (#736 to #739) as the samples change from n-type to p-type, the ODMR signals get stronger rather than being eliminated (see Fig. 7.3 as an example). The increase of the signal intensity with Mg doping, on the other hand, suggests that the donor signal is probably related to compensating deep donors in the samples.

In MOVPE grown samples there are two mechanisms related to the problem of p-type conductivity. One is the passivation of Mg acceptors by forming Mg-H complexes; the other is the formation of compensation centres as Mg concentration is increased. MBE is a hydrogen-free growth process so that Mg-H complexes probably do not exist in the current samples. But compensating centers (mainly deep donors) may still be induced. Theoretical calculations predicted that nitrogen vacancies are the dominant compensating defects in p-type GaN [17]. The isolated nitrogen-vacancy is a deep donor with energy level sitting around ~ 0.4 eV below the conduction band [121]. They are likely to form complexes with acceptors. Substitutional carbon atoms form shallow acceptors in GaN when they are substitutional on the N site and shallow donors when on the Ga site [122].

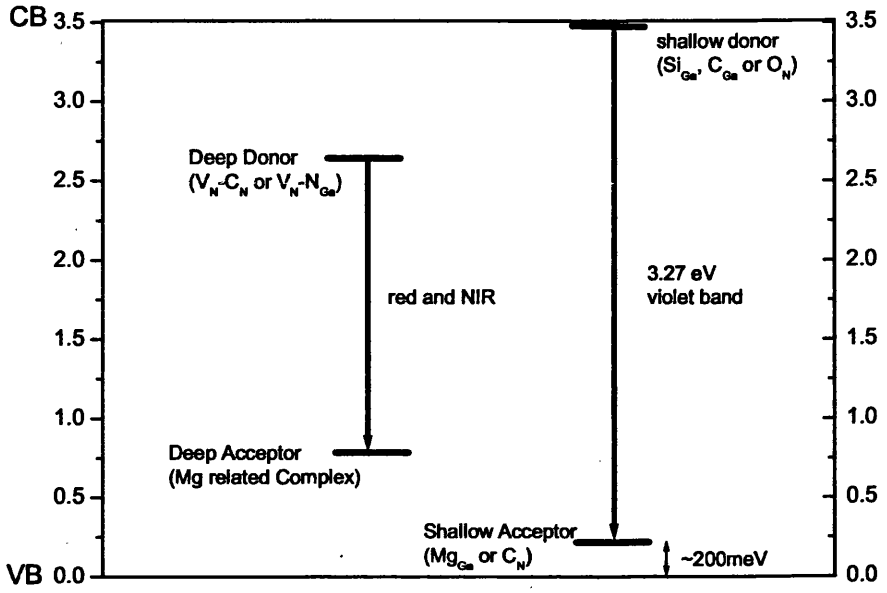

Figure 7.4: Schematic diagram for the recombination process in MBE grown GaN.

It is possible that nitrogen vacancy-C pair defects ($V_N - C_N$) are formed as deep compensation donors. Such a model has been suggested for the origin of the L_1 center reported earlier for electron-irradiated GaN [50]. The g-value of the L_1 center ($g_{||} = 2.008$, $g_{\perp} = 2.004$) is very close to that of the deep donors observed in this work. However, other V_N related compensation defects such as $V_N - N_{Ga}$ are also possible. The $V_N - N_{Ga}$ defect center can be formed through the structural modification $V_{Ga} \longrightarrow N_{anti}+V_N$ and its energy level is at approximately 2 eV above the valence band [123]. Based on the above discussions the following recombination model is suggested for the MBE samples (Fig. 7.4). The weak 3.27 eV band is due to recombination from shallow donors to shallow acceptors, while deep centres are involved in the red-NIR band. Possible models for the defect centres are also shown in the diagram.

7.4 Conclusions

PL and ODMR experiments have been performed on a group of MBE grown GaN samples doped with Mg. Our results suggest that different compensation mechanisms exist in MOVPE and MBE grown samples. Common acceptor passivation and compensation centres in MOVPE grown samples such as Mg-H and $V_N - Mg_{Ga}$ complexes do not appear to exist in MBE grown ones; instead, a new centre is formed. The chemical origin of the centre is tentatively suggested but further theoretical and experimental verification is needed.

References

[1] S. Nakamura, Optical Properties of GaN and Related Materials, Gordon & Breach, Amsterdam, 1998.

[2] J. A. Majewski, M. Städele, P. Vogel, MRS Internet Journal of Nitride Semiconductor Research 1 (1996) Article No. 1.

[3] D. K. Gaskill, C. D. Brandt, R. J. Nemanich (Eds.), III-Nitride, SiC, and Diamond Materials for Electronic Devices, Material Research Society Symposium Proceedings, 1996.

[4] M. Suzuki, T. Uenoyama, Group III Nitride Semiconductor Compounds, Oxford, Clarendon, 1998.

[5] G. D. Chen, M. Smith, J. Y. Lin, H. X. Jiang, S.-H. Wei, M. A. Khan, C. J. Sun, Appl. Phys. Lett. 68 (1996) 2784.

[6] H. M. Ng, Appl. Phys. Lett. 80 (2002) 4369.

[7] M. D. Craven, S. H. Lim, F. Wu, J. S. Speck, S. P. DenBaars, Appl. Phys. Lett. 81 (2002) 469.

[8] G. Popovici, H. Morkoç, S. N. Mohammad, Group III Nitride Semiconductor Compounds, Oxford, Clarendon, 1998.

[9] C. R. Abernathy, GaN and Related Materials, Gordon and Breach, New York, 1997.

[10] S. Nakamura, Y. Harada, M. Senoh, Appl. Phys. Lett. 58 (1991) 2021.

[11] S. T. Strite, H. Morkoç, J. Vacuum Science and Technology B10 (1992) 1237.

[12] H. M. Ng, D. Doppalapudi, T. D. Moustakas, N. G. Weimann, L. F. Eastman, ibid 73 (1998) 821.

[13] S. Nakamura, T. Mukai, M. Senoh, J. Appl. Phys. 71 (1992) 5543.

[14] B. Heying, I. Smorchkova, C. Poblenz, C. Elsass, P. Fini, S. Denbaars, U. Mishra, J. S. Speck, Appl. Phys. Lett. 77 (2000) 2885.

[15] M. J. Manfra, L. N. Pfeiffer, K. W. West, H. L. Stormer, K. w. Baldwin, J. W. P. Hsu, D. V. Lang, R. J. Molnar, ibid 77 (2000) 2888.

[16] S. Limpijumnong, C. G. V. de Walle, Phys. Rev. B 69 (2004) 035207.

[17] J. Neugebauer, C. G. V. de Walle, Phys. Rev. B 50 (1994) 8067.

[18] T. Mattila, R. Nieminen, Phys. Rev. B 55 (1997) 9571.

[19] P. Boguslawski, E. L. Briggs, J. Bernholc, Phys. Rev. B. 51 (1995) 17255.

[20] H. P. Maruska, J. J. Tietjen, Appl. Phys. Lett. 15 (1969) 327.

[21] M. Ilegems, H. C. Montgomery, J. Phys. Chem. Solids 34 (1973) 885.

[22] S. Nakamura, G. Fasol, The blue laser Diode, Springer, Berlin, 1998.

[23] W. J. Moore, J. A. F. Jr., S. K. Lee, S. S. Park, J. Y. Han, Phys. Rev. B 65 (2002) 081201.

[24] J. Neugebauer, C. G. V. de Walle, Festkorperprobleme/Advances in Solid State Physics, Vieweg, Braunschweig/Wiesbaden, 1996.

[25] M. A. Reshchikov, H. Morkoç, J. Appl. Phys. 97 (2005) 061301.

[26] H. Harima, T. Inoue, S. Nakashima, M. Ishida, M. Taneya, Appl. Phys. Lett. 75 (1999) 1383.

[27] S. M. Myers, A. F. Wright, G. A. Peterson, W. R. Wampler, C. H. Seager, M. H. Crawford, J. Han, J. Appl. Phys. 89 (2001) 3195.

[28] S. Yoshida, S. Misawa, S. Gonda, Appl. Phys. Lett. 42 (1983) 427.

[29] S. Yoshida, S. Misawa, S. Gonda, J. Vac. Sci. & Techol. B 1 (1983) 250.

[30] H. Amano, M. Kito, K. Hiramatru, I. Akasaki, Inst. Phys. Conf. Ser. 106 (1989) 725.

[31] H. Amano, M. Kito, K. Hiramatru, I. Akasaki, Jpn. J. Appl. Phys. 28 (1989) L2112.

[32] S. Nakamura, Jpn. J. Appl. Phys. 30 (1991) L1705.

[33] S. Nakamura, M. Senoh, T. Mukai, Jpn. J. Appl. Phys. 30 (1991) L1708.

[34] S. Nakamura, T. Mukai, M. Senoh, N. Iwasa, Jpn. J. Appl. Phys. 31 (1992) L139.

[35] B. Goldenberg, J. D. Zook, R. J. Ulmer, Appl. Phys. Lett. 62 (1993) 381.

[36] M. A. Khan, J. N. Kuznia, D. T. Olson, M. Blasingame, A. R. Bhattarai, Appl. Phys. Lett. 63 (1993) 2455.

[37] H. Obloh, K. H. Bachem, U. Kaufmann, M. Kunzer, M. Maier, A. Ramakrishnan, P. Schlottor, J. Cryst. Growth. 195 (1998) 270.

[38] R. T. Cox, Rev. Physique Appl. 15 (1980) 653.

[39] B. C. Cavenett, Advan. Phys. 30 (1981) 475.

[40] J. J. Davies, J. Crystal Growth 72 (1985) 317.

[41] B. K. Meyer, Semicond. Semimetals 57 (1999) 371.

[42] T. A. Kennedy, E. R. Glaser, Identification of Defects in Semiconductors, Academic, San Diego, 1998.

[43] D. Wolverson, G. N. Aliev, S. J. Bingham, J. J. Daavies, S. Stepanov, B. Yavich, W. N. Wang, not published .

[44] L. M. Roth, B. Lax, S. Zwerdling, Phys. Rev. 114 (1959) 90.

[45] E. R. Weber, H. Ennen, U. Kaufmann, J. Windscheif, J. Schneider, T. Wosinski, J. Appl. Phys. 53 (1982) 6140.

[46] D. J. Dunstan, J. J. Davies, J. Phys. C: Solid State Phys. 12 (1979) 2927.

[47] H. Weman, M. Godlewski, B. Monemar, Phys. Rev. B. 38 (1988) 12525.

[48] F. P. Wang, B. Monemar, M. Ahlstrm, Phys. Rev. B. 39 (1989) 11195.

[49] U. Kaufmann, M. Kunzer, H. Obloh, M. Maier, C. Manz, A. Ramakrishnan, B. Santic, Phys. Rev. B 59 (1999) 5561.

[50] D. M. Hofmann, B. K. Meyer, H. Alves, F. Leiter, W. Burkhard, N. Romanov, Y. Kim, J. Kruger, E. R. Weber, Phys. Stat. Sol. (b) 180 (2000) 261.

[51] M. W. Bayerl, M. S. Brandt, O. Ambacher, M. Stutzmann, E. R. Glaser, R. L. Henry, A. E. Wickenden, D. D. Koleske, T. Suski, I. Grzegory, S. Porowski, Phys. Rev. B 63 (2001) 125203.

[52] M. Bayerl, M. Brandt, E. Glaser, A. Wickenden, D. Koleske, R. Henry, M. Stutzmann, Phys. Stat. Sol. (b) 216 (1999) 547.

[53] O. Gelhausen, M. R. Phillips, E. M. Goldys, T. Paskova, B. Monemar, M. Strassburg, A. Hoffmann, Phys. Rev. B 69 (2004) 125210.

[54] U. Kaufmann, M. Kunzer, M. Maier, H. Obloh, A. Ramakrishnan, B. Santic, P. Schlotter, Appl. Phys. Lett. 72 (1998) 1326.

[55] S. Hautakangas, J. Oila, M. Alatalo, K. Saarinen, L. Liszkay, D. Seghier, H. P. Gislason, Phys. Rev. Lett. 90 (2003) 137402.

[56] C. D. Latham, R. Jones, S. Oberg, R. M. Nieminen, P. R. Briddon, Phys. Rev. B 68 (2003) 205209.

[57] R. Krause-Rehberg, H. S. Leipner, Positron Annihilation in Semiconductors: Defect Studies, Springer, Berlin, 1999.

[58] N. B. Chilton, P. G. Coleman, Meas. Sci. Technol. 6 (1995) 53.

[59] U. Kaufmann, M. Kunzer, C. Merz, I. Akasaki, H. Amano, Mat. Res. Soc. Proc. 395 (1996) 633.

[60] S. J. Xu, G. Li, S. J. Chua, X. C. Wang, W. Wang, Appl. Phys. Lett. 72 (1998) 2451.

[61] M. Toth, K. Fleischer, M. R. Phillips, Phys. Rev. B 59 (1999) 1575.

[62] H. C. Yang, T. Y. Lin, Y. F. Chen, Phys. Rev. B 62 (2000) 12593.

[63] K. Saarinen, T. Laine, S. Kuisma, J. Nissila, P. Hautojarvi, L. Dobrzynski, J. M. Baranowski, K. Pakula, R. Stepniewski, M. Wojdak, A. Wysmolek, T. Suski, M. Leszcznski, I. G.rzegory, S. Porowski, Phys. Rev. B 79 (1997) 3030.

[64] H. W. Choi, S. J. Chua, Phys. Stat. Sol. (a) 188 (2001) 393.

[65] F. Varsanyi, D. Wood, A. Schawlow, Phys. Rev. Lett. 3 (1959) 544.

[66] A. Viswanath, E. Shin, J. Lee, S. Yu, D. Kim, B. Kim, Y. Choi, , C.-H. Hong, J. Appl. Phys. 83 (1998) 2272.

[67] E. Glaser, W. Carlos, G. Braga, J. F. Jr., W. Moore, B. Shanabrook, R. Henry, A. Wickenden, D. Koleske, H. Obloh, P. Kozodoy, S. DenBaars, U. Mishra, Phys. Rev. B 65 (2002) 085312.

[68] W. Götz, N. M. Johnson, C. Chen, H. Liu, C. Kuo, W. Imler, Appl. Phys. Lett. 68 (1996) 3144.

[69] C. Wetzel, T. Suski, J. W. A. III, E. R. Weber, E. E. Haller, S. Fischer, B. K. Meyer, R. J. Molnar, P. Perlin, Phys. Rev. Lett. 78 (1997) 3923.

[70] M. A. Reshchikov, G.-C. Yi, B. W. Wessels, MRS Internet J. Nitride Semicond. Res. 4S1 (1999) G11.8.

[71] Y. H. Kwon, S. K. Shee, G. H. Gainer, G. H. Park, S. J. Hwang, J. J. Song, Appl. Phys. Lett. 76 (2000) 840.

[72] M. A. Reshchikov, H. Morkoç, S. S. Park, K. Y. Lee, Appl. Phys. Lett. 81 (2002) 4970.

[73] W. Carlos, J. Freitas, M. A. Khan, D. Olson, J. Kuznia, Phys. Rev. B 48 (1993) 17878.

[74] E. R. Glaser, T. A. Kennedy, J. A. F. Jr., B. Shanabrook, A. E. Wickenden, D. Koleskea, R. Henry, H. Obloh, Physica B 273 (1999) 58.

[75] J. Neugebauer, C. G. V. de Walle, Appl. Phys. Lett. 68 (1996) 1829.

[76] E. Calleja, F. J. Sánchez, D. Basak, M. A. Sánchez-Garsía, E. M. noz, I. Izpura, F. Calle, J. M. G.Tijero, J. L. Sánchez-Rojas, B. Beaumont, P. Lorenzini, P. Gibart, Phys. Rev. B 55 (1997) 4689.

[77] X. D. Pi, P. G. Coleman, C. L. Tseng, C. P. Burrows, B. Yavich, W. N. Wang, J. Phys.: Condens. Matter 14 (2002) 243.

[78] J. Moxom, J. Xu, R. Suzuki, T. Ohdaira, G. Brandes, J. S. Flynn, J. Appl. Phys. 92 (2002) 1898.

[79] J. Oila, V. Ranki, J. Kivioja, K. Saarinen, P. Hautojärvi, J. Likonen, J. M. Baranowski, K. Pakula, T. Suski, M. Leszczynski, I. Grzegory, Phys. Rev. B 63 (2001) 04205.

[80] U. Kaufmann, P. Schlotter, H. Obloh, K. Köler, M. Maier, Phys. Rev. B 62 (2000) 10867.

[81] K. Saarinen, J. Nissila, P. Hautojärvi, J. Likonen, T. Suski, I. Grzegory, B. Lucznik, S. Porowski, Appl. Phys. Lett. 75 (1999) 2441.

[82] J. Neugebauer, C. G. V. de Walle, Phys. Rev. Lett. 75 (1995) 4452.

[83] W. Götz, N. M. Johnson, D. P. Bour, M. D. McCluskey, E. E. Haller, Appl. Phys. Lett. 69 (1996) 3725.

[84] E. Sonder, W. A. Sibley, Point Defects in Solids, Plenum, New York London, 1972.

[85] G. N. Aliev, S. Zeng, J. J. Davies, D. Wolverson, S. J. Bingham, P. J. Parbrook, T. Wang, Phys. Rev. B 71 (2005) 195204.

[86] G. H. Park, D. J. Chadi, Phys. Rev. B 55 (1997) 12995.

[87] A. Abragam, B. Bleaney, Electron Paramagnetic Resonance of Transition-Metal Ions, Oxford University Press, Oxford, 1970.

[88] J. J. Davies, G. N. Aliev, S. J. Bingham, D. Wolverson, S. Stepanov, B. Yavich, W. Wang, Phys. Rev. B 67 (2003) 035203.

[89] M. W. Bayerl, M. S. Brandt, T. Suski, I. Grzegory, S. Porowski, , M. Stutzmann, Physica B 273-274 (1999) 120.

[90] M. Godlewski, T. Suski, I. Grzegory, s. Porowski, J. P. Bergman, W. M. Chen, B. Monemar, Physica B 273-274 (1999) 39.

[91] E. R. Glaser, T. A. Kennedy, K. Doverspike, I. B. Rowland, D. Gaskill, J. A. F. Jr., M. A. Khan, D. Olson, J. N. Kuznia, A. E. Wickenden, Phys. Rev. B 51 (1995) 13326.

[92] D. M. Hofmann, W. Burkhardt, F. Leiter, W. von Forster, H. Alves, A. Hofstaetter, B. K. Meyer, N. Romanov, H. Amano, , I. Akasaki, Physica B 43 (1999) 273.

[93] G. P. Yablonskii, A. L. Gurskii, E. V. Lutsenko, I. P. Marko, B. Schineller, A. Guttzeit, O. Schoen, M. Heuken, K. Heime, R. Beccard, D. Schmitz, H. Juergensen, J. Electr. Materials 27 (1997) 222.

[94] W. Shan, B. D. Little, A. J. Fisher, J. J. Song, B. Goldenberg, W. G. Perry, M. D. Bremser, R. F. Davis, Phys. Rev. B 54 (1996) 16369.

[95] H. Morkoç, Nitride Semiconductors and Devices, Springer, Berlin, 1999.

[96] J. K. Sheu, Y. K. Su, G. C. Chi, B. J. Pong, C. Y. Chen, C. N. Huang, W. C. Chen, J. Appl. Phys. 84 (1998) 4590.

[97] Y. Li, Y. Lu, H. Shen, M. Wraback, C. Y. Hwang, M. Shurman, W. Mayo, T. Salagaj, R. A. Stall, Mater. Res. Soc. Symp. Proc. 395 (1996) 369.

[98] M. Lachab, D. H. Youn, R. S. Q. Fareed, T. Wang, S. Sakai, Sol. St. Electronics 44 (2000) 1669.

[99] L. S. Vlasenko, C. Bozdog, G. D. Watkins, F. Shahedipour, B. W. Wessels, Phys. Rev. B 65 (2002) 205202.

[100] M. Palczewska, B. Suchanek, R. Dwilinski, K. Pakula, A. Wagner, M. Kaminska, MRS Internet J. Nitride Semicond. Res. 3 (1998) 45.

[101] M. Kunzer, U. Kaufmann, K. Maier, J. Schneider, N. Herres, I. Akasaki, H. Amano, Mater. Sci. Forum 87 (1994) 143.

[102] M. Kunzer, J. Baur, U. Kaufmann, J. Schneider, H. Amano, I. Akasaki, Solid-State Electron. 41 (1997) 189.

[103] E. R. Glaser, W. E. Carlos, G. C. B. Braga, J. A. F. Jr., W. J. Moore, B. Shanabrook, A. E. Wickenden, D. D. Koleske, R. L. Henry, M. W. Bayerl, M. S. Brandt, H. Obloh, P. Kozodoy, S. P. DenBaars, U. K. Mishra, S. Nakamura, E. Haus, J. S. Speck, J. E. V. Nostrand, M. A. Sanchez, E. Calleja, A. J. Ptak, T. H. Myers, R. J. Molnar, Mater. Sci. and Eng. B93 (2002) 39.

[104] S. Geschwind, R. J. Collins, A. L. Schawlow, Phys. Rev. Lett. 3 (1959) 545.

[105] F. K. Koschnick, K. Michael, J. M. Spaeth, B. Beamont, P. Gibart, J. Off, A. Sohmer, F. Scholz, J. Cryst. Growth. 76 (1998) 561.

[106] M. W. Bayerl, M. S. Brandt, O. Ambacher, M. Stutzmann, E. R. Glaser, R. L. Henry, A. E. Wickenden, D. D. Koleske, T. Suski, I. Grzegory, S. Porowski, Phys. Rev. B 63 (2000) 125203.

[107] N. G. Romanov, P. G. Baranov, Semicond. Sci. Technol. 9 (1994) 1080.

[108] M. Smith, G. D. Chen, J. Y. Lin, H. X. Jiang, A. Salvador, B. N. Sverdlov, A. Botchkarev, H. Morkoç, B. Goldenberg, Appl. Phys. Letts. 68 (1996) 1883.

[109] S. Nakamura, N. Iwasa, M. Senoh, T. Mukai, Jpn. J. Appl. Phys. 31 (1992) 1258.

[110] A. F. Wright, S. M. Myers, J. Appl. Phys. 94 (2003) 4918.

[111] F. Shahedipour, B. W. Wessels, Appl. Phys. Letts. 76 (2000) 3011.

[112] F. Shahedipour, B. W. Wessels, MRS Internet J. Nitride Semicond. Res. 6 (2001) 12.

[113] L. H. Robins, P. C. Taylor, T. A. Kennedy, Phys. Rev. B 38 (1988) 13227.

[114] D. Verity, J. J. Davies, J. E. Nicholls, J. Phys. C: Solid State Phys. 14 (1980) 485.

[115] N. Grandjean, J. Massies, S. Dalmasso, P. Vennéguès, L. Siozade, L. Hirsch, Appl. Phys. Lett. 74 (1999) 3616.

[116] F. B. Naranjo, S. Fernàndes, M. A. Sànches-Garciá, F. Calle, E. Calleja, Appl. Phys. Lett. 80 (2002) 2198.

[117] P. Waltereit, H. Sato, C. Poblenz, D. S. Green, J. S. Brown, M. McLaurin, T. Katona, S. P. DenBaars, J. S. Speck, Appl. Phys. Lett. 84 (2004) 2748.

[118] S. Hooper, M. Kauer, V. Bousquet, K. Johnson, J. Barnes, J. Heffernan, Electron. Lett. 40 (2004) 33.

[119] S. Hooper, M. Kauer, V. Bousquet, K. Johnson, C. Zellweger, J. Heffernan, J. Cryst. Growth. 278 (2005) 361.

[120] H. Alves, M. Böhm, A. Hofstaetter, H. Amano, S. Einfeldt, D. Hommel, D. M. Hofmann, B. K. Meyer, Physica B 308-310 (2001) 38.

[121] T. L. Tansley, R. J. Egan, Phys. Rev. B 45 (1992) 10942.

[122] P. Boguslawski, E. L. Briggs, J. Bernholc, Appl. Phys. Lett. 69 (1996) 1996.

[123] D. J. Chadi, Appl. Phys. Lett. 71 (1997) 2970.